



TECHNISCHE  
UNIVERSITÄT  
WIEN  
Vienna | Austria



## DIPLOMARBEIT

---

# EFFICIENCY MEASUREMENT OF THE AEGIS FACT DETECTOR AND DEVELOPMENT OF ANALYSIS TOOLS

---

zur Erlangung des akademischen Grades

**Diplom-Ingenieur**

im Rahmen des Studiums

**Technische Physik**

eingereicht von

**Philip Hackstock**

Matrikelnummer 01253210

Ausgeführt am:

Stefan Meyer Institut und  
Technische Universität Wien

Betreuung:

Dipl.-Ing. Dr. Chloé Malbrunot (CERN)  
Hon.-Prof. Dipl.-Phys. Dr. Eberhard Widmann  
(Stefan Meyer Institut)

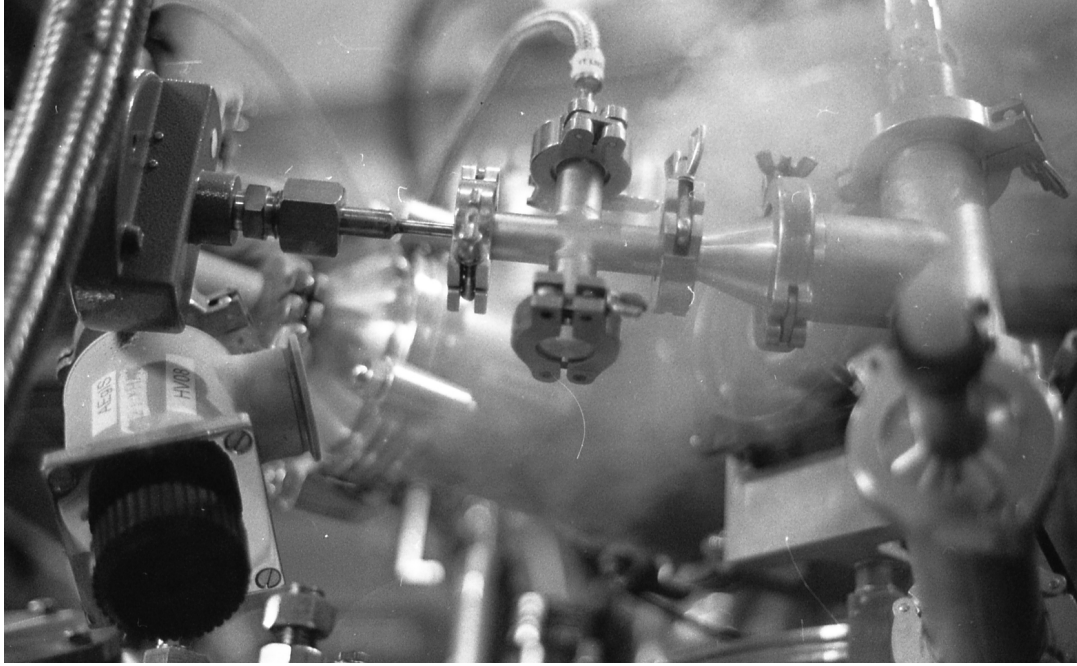
Wien, 04.03.2020:

\_\_\_\_\_  
(Verfasser)

\_\_\_\_\_  
(Betreuer)



Die approbierte gedruckte Originalversion dieser Diplomarbeit ist an der TU Wien Bibliothek verfügbar.  
The approved original version of this thesis is available in print at TU Wien Bibliothek.



---

Picture of the AEGIS apparatus with liquid Helium vapor after filling the superconducting magnets of the experiment. Keeping the magnets cool at all times is a collaborative effort shared among the members of the AEGIS collaboration. In that sense the picture may be seen to symbolically represent the team effort I was fortunate enough to contribute to.

The picture was taken with an analog camera and developed in the darkroom of the CERN photoclub under the guidance of my friend Athena.

---



Die approbierte gedruckte Originalversion dieser Diplomarbeit ist an der TU Wien Bibliothek verfügbar.  
The approved original version of this thesis is available in print at TU Wien Bibliothek.

# Abstract

This thesis presents the results of a year's work on the FACT (**F**ast **A**nnihilation **C**ryogenic **T**racker) detector of the AEGIS experiment at CERN. FACT is a tracking detector that uses scintillating fibers to track charged pions from antiproton annihilations. As the AEGIS experiment's primary antihydrogen detector, FACT plays a critical role in achieving the collaboration's goal of performing a gravity measurement on antihydrogen.

The first part of this thesis covers the basics of the detector including mechanical design, hardware, measurement capabilities and the developed analysis software.

In the second part a method for determining the efficiency of the individual channels of FACT is derived. As the approach does not require an external reference detector, it is dubbed the "MEM" (**M**ünchenhausen **e**fficiency **m**ethod). More generally speaking, the MEM presents a way to measure the efficiencies of the smallest detection units of any pixel or pixel-like tracking detector.

In the third chapter, the MEM is applied to antiproton annihilation data to extract the average fiber efficiency of FACT which is found to be  $\sim 46\%$ . This translates to an average charged pion tracking efficiency of  $\sim 50\%$ . For this efficiency 0.75 tracks can be expected to be reconstructed per antihydrogen annihilation.

Additionally, a total of 30 dead channels are identified which can be repaired for a boost in detection efficiency. Through time-resolved comparison with another detector system in the AEGIS experiment a saturation effect of FACT as a result of a too high antiproton annihilation rate was identified.

Using the MEM with cosmic radiation for a measurement of the FACT efficiency and calibration of the detector had to remain uncharted territory due to algorithmic limitations which are discussed as well. Details on the locations of the current bottlenecks are provided so that this thesis may serve as a basis for future work and contribute to the success of the AEGIS collaboration.



Die approbierte gedruckte Originalversion dieser Diplomarbeit ist an der TU Wien Bibliothek verfügbar.  
The approved original version of this thesis is available in print at TU Wien Bibliothek.

# Kurzfassung

Die vorliegende Arbeit behandelt die Ergebnisse von einem Jahr Arbeit am FACT Detektor (**F**ast **A**nnihilation **C**ryogenic **T**racker) des AEGIS Experiments am CERN. FACT ist ein Teilchenspurdetektor, der mittels szintillierender Kunststofffasern Spuren von geladenen Pionen aus Antiprotonannihilationen misst. Als Haupt-Antiwaterstoffdetektor des AEGIS Experiments, spielt er eine tragende Rolle auf dem Weg zur Messung der Gravitationskonstante von Antiwaterstoff.

Das erste Kapitel behandelt Grundlagen des Detektors in den Aspekten mechanisches Design, Hardware, Spurrekonstruktionsstrategie und die für Datenanalyse entwickelte Software.

Im zweiten Kapitel wird eine Methode zur Messung der Effizienz der einzelnen Kanäle von FACT entwickelt. Nachdem sie ohne äußeren Referenzdetektor auskommt, wird die Methode "MEM" (**M**ünchhausen **E**ffizienz **M**ethode) genannt. Der Einsatz der MEM ist allerdings nicht auf FACT beschränkt, sondern kann allgemein zur Messung der Effizienz der kleinsten Detektionselemente eines beliebigen Spurrekonstruktionsdetektors verwendet werden.

Im dritten Kapitel wird mit Hilfe der MEM unter Verwendung von Messdaten von Antiprotonannihilationen eine durchschnittliche Kanaleffizienz von  $\sim 46\%$  bestimmt. Umgerechnet entspricht dieser Wert entspricht einer Spurrekonstruktionseffizienz für geladene Pionen von  $\sim 50\%$ . Pro Antiwaterstoffannihilation können damit in etwa 0.75 Teilchenspuren rekonstruiert werden.

Außerdem werden insgesamt 30 defekte Kanäle identifiziert, welche repariert werden können um eine unmittelbare Effizienzsteigerung des Detektors zu erzielen.

Mittels zeitaufgelöster Vergleichsmessung mit einem zweiten Detektorsystem des AEGIS Experiments wurde ein Sättigungseffekt bei FACT entdeckt. Dieser tritt als Folge einer zu hohen Antiprotonannihilationsrate auf und äußert sich in stark reduzierter Detektionseffizienz.

Die Verwendung von kosmischer Strahlung zur Effizienzbestimmung und Kalibrierung von FACT blieb leider unerforschtes Terrain. Der Grund dafür sind algorithmische Limitationen, die ebenfalls im dritten Kapitel im Detail diskutiert werden. Damit soll diese Arbeit als Grundlage für zukünftige Entwicklungen dienen und zum Erfolg des AEGIS Experiments beitragen.



Die approbierte gedruckte Originalversion dieser Diplomarbeit ist an der TU Wien Bibliothek verfügbar.  
The approved original version of this thesis is available in print at TU Wien Bibliothek.



# Acknowledgements

As is custom when writing a thesis, I would like to take a moment to express gratitude for the people who helped me along the way. As experimental physics is becoming an ever more complex endeavour, there is simply no way around collaboration in order to achieve a research goal. However, calling the work with my colleagues in the AEGIS experiment just a collaboration, would hardly do the year I was fortunate enough to spend at CERN justice. Many close friendships formed that last to this day.

First and foremost I'd like to thank my supervisor **Chloé Malbrunot** for providing me with guidance for my work. No matter the time of day or day in the week she was always available for immediate feedback and input. She encouraged me to push forward with my analyses to get the best possible results.

I would like to thank **Michael Doser** and the entire **AEGIS** collaboration for allowing me to contribute to their efforts and providing financial support for my time at CERN.

My stay at CERN would also not have been possible either without financial support from **Eberhard Widmann** and the **Stefan Meyer Institute**.

Additionally, I would like to thank **CERN** for creating a wonderful place for pushing the boundaries of human knowledge and enabling intercultural exchange. Thank you for letting me contribute to this great goal.

**Stefan Haider** contributed to this work not only by providing free coffee every day but free chocolate as well. All jokes aside (free coffee should never be taken as a joke anyway), the countless conversations including but not limited to topics such as why one should generally avoid blowing hot Helium into a cryogenic vessel cooling a superconducting magnet provided a lot of useful insight.

Distilling the impact **Francesco Guatieri** had on my work into two or three sentences is a feat far beyond my capabilities as a writer. Therefore I'll keep it simple by saying that I'm thankful for all the fun hours we've spent dissecting code and chasing various ghosts up and down the system.

As a part of the core FACT team **Germano Bonomi** was a massive help throughout the course of this thesis. I don't know a lot of people who would answer to Monte Carlo simulation requests during intercontinental travel.

**Nicola Zurlo** has always had an open ear for detector physics related questions and more than once his answer was "Ah you see, I have already solved your problem. Here's the solution for you to use."

On a rather technical note, almost all illustrations and plots in this thesis were produced using the open source Python plotting library Matplotlib [1]. Matplotlib is the brainchild of the late John D. Hunter and I am deeply indebted to him and the current developer base for providing an excellent, open source data potting and vizualization tool.

**Ruggero Caravita** became a good friend through the many conversations in the control room and the post-work beers at ÔBrasseur. Remotely chasing and killing an haywire daemon from his laptop after a long day of off-piste skiing in the Swiss alps is a thrill that I would've never known without him.

Thank you **Seba Mariazzi** for showing me Trento and that having oven-fresh Italian pizza in the sun as a daily lunch is an essential ingredient for good research. I have to thank **Milena Vujanovic** for reminding me time and time again that mental health is every bit as important for a researcher's success as knowledge of facts and formulae.

Not a single work day during my year at CERN has gone by without having a laugh with the AEGIS control room crew including but not limited to **Lillian Smestad**, **Olga Khalidova**, **Antoine Camper** and **Benji Rienacker**. Thank you guys for keeping the mood light even in stressful times.

On a more personal side of things I want to thank the two best roommates **Katt Andryskova** and **Tobi Kulenkampff**. I'll keep the fondest of memories of our countless coffees, mountain adventures and Rick and Morty nights.

As the community of people at CERN is an integral part of what makes it a unique and fantastic place I would like to thank all the great friends I've made during my time there. Thank you **Stani**, **Doug**, **Francesca**, **Will**, **Athena**, **Jaakko**, **Giovanni** and everyone else who came by even for just a quick coffee or a beer.

The amount of gratitude my wonderful girlfriend **Jennie Atwell** deserves for her support cannot be compressed into a few sentences. I'll leave it at a simple thank you for having a seemingly endless amount of patience and understanding.

Last but by no means least I want to thank my parents **Christa** and **Rainer Hackstock** and my little brother **Felix**. I simply could not have done any of this without your endless support. Thank you for always putting up with me even in my most "mentally somewhere else" state.

# Dear Reader

Before this thesis really starts I would like to take a minute and break the fourth wall for a just a second.

Dear future FACT person,

(Chances are if you're reading this thesis, that's you)

(If you're just here out of curiosity, please feel welcome too)

Perhaps this is your first introduction to the detector, or maybe you are a veteran already and merely wanted to look up some details. Either way, please know that this thesis is written for you to be used as a tool and a reference guide.

As such, it makes heavy use of hyperlinks pointing to different parts within the document and to the TWiki of the AEGIS collaboration. On the TWiki you can find additional information such as raw data and full results of analyses for further studies, python scripts used for calculations or C++ code focused technical caveats.

Additionally, appendix A provides an introduction on how to start analyzing FACT data. It features a documentation of the of the analysis code and a tutorial analysis with some practice tasks to get started.

This package of information was created to give you an easy start to the analysis of FACT data and enable a seamless continuation of the work presented in this thesis.

I hope that I've succeeded in providing you a solid base to build your work on in the same way as I've built this thesis on the work of my wonderful colleagues.

All that's left for me to do is wish you all the best for your work and start with the thesis.



Die approbierte gedruckte Originalversion dieser Diplomarbeit ist an der TU Wien Bibliothek verfügbar.  
The approved original version of this thesis is available in print at TU Wien Bibliothek.

# Contents

<b>Introduction</b>	<b>1</b>
The AEGIS Experiment . . . . .	3
Content of this Thesis . . . . .	7
<b>1 Introduction to FACT</b>	<b>9</b>
1.1 Geometry and Hardware . . . . .	10
1.1.1 Mechanical Design . . . . .	10
1.1.2 Nature of the signals in FACT . . . . .	13
1.1.3 Readout Electronics . . . . .	13
1.2 Control Software . . . . .	16
1.3 Data Analysis . . . . .	18
1.3.1 Track Reconstruction . . . . .	18
1.3.2 Vertex Reconstruction . . . . .	25
1.3.3 Cosmic Ray Tracking . . . . .	29
1.3.4 Analysis Software . . . . .	30
<b>2 Efficiency Measurement Method</b>	<b>35</b>
2.1 Derivation of the Method . . . . .	36
2.1.1 Required Amount of Particles . . . . .	44
2.2 Antiproton Monte Carlo . . . . .	50
2.3 Cosmic Radiation Monte Carlo . . . . .	55
2.4 Cosmic Daemon . . . . .	60
<b>3 Efficiency Measurement Results</b>	<b>63</b>
3.1 Antiproton Annihilations . . . . .	63
3.1.1 Comparison with the Outer Scintillators . . . . .	70
3.2 Cosmic Muons . . . . .	77
3.3 Discussion and Outlook . . . . .	80
<b>Conclusion</b>	<b>83</b>
<b>Appendices</b>	<b>85</b>
<b>A AEgFACT Analysis Index</b>	<b>87</b>
<b>B FACT Mapping</b>	<b>95</b>
<b>C Dead Channels</b>	<b>101</b>



Die approbierte gedruckte Originalversion dieser Diplomarbeit ist an der TU Wien Bibliothek verfügbar.  
The approved original version of this thesis is available in print at TU Wien Bibliothek.

# Introduction

$$\left( \beta mc^2 + c \left( \sum_{n=1}^3 \alpha_n \beta_n \right) \right) \psi(x, t) = i\hbar \frac{\partial \psi(x, t)}{\partial t}$$

When British physicist Paul Dirac derived his now famous Dirac equation in 1928, a breakthrough in theoretical physics had been made. The equation managed to combine quantum mechanics and special relativity and successfully described the behaviour of electrons at relativistic energies. It did, however, yield a peculiar property. The solutions to the equation could have both positive and negative energies. Dirac interpreted the vacuum as an infinite sea where all negative energy eigenstates are occupied. In the event that a negative energy state was not occupied this hole would interact with an electromagnetic field in the same way as an electron carrying opposite charge.

In 1932 Carl Anderson found the experimental proof that those negative energy eigenstates were not holes but in fact actual particles. Using a cloud chamber to investigate cosmic radiation, he discovered a particle that exhibited the same properties as an electron but curved the opposite way in a magnetic field. This marked the discovery of the positron, for which he was awarded the Nobel prize in 1936.

When Dirac received the Nobel prize in 1933, it was predicted that every particle has a corresponding antiparticle, and thus the hunt for more antiparticles begun. In the following years, the study of cosmic radiation proved to be fruitful grounds for further discoveries. In 1936 the muon and in 1947 the pion and the kaon, with their respective antiparticles were found. However, the antiparticle of the most prevalent baryonic matter state, the antiproton ( $\bar{p}$ ), remained elusive until 1955. At that time particle accelerator technology had advanced enough for the Bevatron in Berkeley, California to be constructed. This accelerator could produce proton beams of up to 6 GeV. Together with their team Emilio Segrè and Owen Chamberlain managed to create and detect antiprotons by firing a proton beam at a copper target [2]. Only a year later, again at the Bevatron, the antineutron was discovered by the research group of Bruce Cork and his team [3].

After the discovery of the three antiparticles of electron, proton and neutron, the next step was producing nuclei and subsequently atoms made up entirely of antimatter.

The first goal was achieved in 1965 by two different teams at the same time. Antonino Zichichi led the team at CERN, Geneva [4] while Leon Lederman with his group operated at Brookhaven, New York [5]. Both teams successfully produced anti-deuteron nuclei, comprised of an antiproton and an antineutron. Creating an antimatter atom, however, proved to be a difficult task.

Firstly, a mechanism for storing and cooling antiprotons had to be developed. This device came in 1978 in form of the ICE (Initial Cooling Experiment) at CERN, which managed to store antiprotons for about 85 h. Using its successor, the LEAR (Low Energy Antiproton Ring), Walter Oelert and his team in 1996 produced nine antihydrogen ( $\bar{H}$ ) atoms [6], consisting of a positron orbiting an antiproton. Later that year a team at Fermilab managed to create even more antihydrogen, counting a total of 66 atoms [7].

The antihydrogen formation process used by both Oelert and his team as well as the Fermilab group yielded  $\bar{H}$  at relativistic energies, not suited for measurements of its properties. In order to perform precision measurements, new techniques for storing and cooling antiprotons were needed. Precision studies of antihydrogen are of particular interest because its matter counterpart, hydrogen, is the most simple stable atom and one of the best studied and characterized systems in physics. Comparisons between the properties of hydrogen and antihydrogen are a valuable test for CPT symmetry (Charge conjugation Parity transformation Time reversal). CPT symmetry predicts that all physical processes must occur in the same way if simultaneously all involved particles are replaced by their antiparticles, all their positions are reflected by an arbitrary plane and time is reversed. This implies that matter and antimatter have the same properties and so far there is no sign of any processes which suggest otherwise. According to the CPT theorem, CPT symmetry is expected to hold for any quantum field theory under mild assumptions. Experimental evidence of CPT-symmetry breaking could provide hints towards the currently unsolved problem of the imbalance of matter over antimatter in the observable universe.

In order to provide the needed low-energy antiprotons for precision experiments, the Antiproton Decelerator (AD) commenced operations at CERN in 1999. Currently, six different experiments are exploring the physics of antimatter by manipulating the  $\bar{p}$  provided by the AD. As of today, all measurements confirm the theoretically predicted symmetry between matter and antimatter.

While antimatter has been observed interacting with the electromagnetic as well as the strong and the weak force, no experiment has yet precisely probed its gravitational interaction. Such a measurement would be a test of the weak equivalence principle (WEP) for antimatter. The weak equivalence principle states the universality of free fall or, in other words, gravitational and inertial mass are to be equal for all bodies. It has been tested and confirmed experimentally with matter for centuries. The best measurement to date has a relative accuracy of  $2 \times 10^{-17}$  by Reasenberget al. [8]. In contrast, the only antimatter WEP measurement to date by the ALPHA collaboration [9] set bounds for the ratio of gravitational ( $m_g$ ) to inertial mass ( $m_i$ ) of  $-65 < m_g/m_i < 110$ . This means that to this day negative gravitational attraction for antimatter is not directly excluded.

With the goal of a measurement of antimatter's gravity constant with a 1% precision, an experiment at the antiproton decelerator called AEGIS (Antimatter Experiment: Gravity, Interferometry, Spectroscopy) [10] was proposed in 2007. It got approved in 2008, the year that marked the 80<sup>th</sup> anniversary of Paul Dirac's eponymous equation, which laid the foundation for the entire field of antimatter research.



## The AEGIS Experiment

The AEGIS experiment started in 2008 as a European collaboration consisting of 18 different institutes from 9 different countries. The experiment's goal is to probe the weak equivalence principle for antimatter by measuring its gravitational constant to an uncertainty of 1%.

The experimental concept of AEGIS involves sending a beam of antihydrogen through a classical Moiré deflectometer. The setup developed for AEGIS consists of two gratings and a position sensitive detector placed in succession (as seen in figure 1). The two gratings and the detector are placed with equal spacing between each other. After the atoms traverse both gratings, a regular pattern in the number of atoms along the vertical direction emerges which is recorded by the detector. If the deflectometer is installed parallel to the ground, gravity will act on the atoms during their flight and the pattern measured by the detector will shift. Given an atom's time of flight  $\tau$  between the two gratings and the shift  $\Delta y$ , the gravitational acceleration  $a$  is given by  $a = \frac{\Delta y}{\tau^2}$  [11].

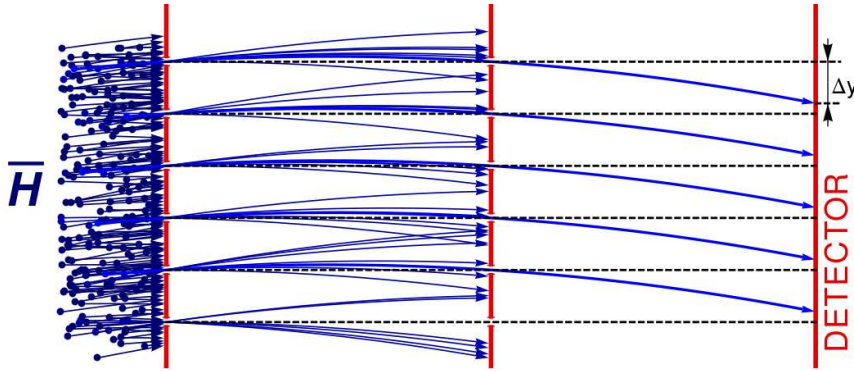


Figure 1: The non-monochromatic antihydrogen beam shown in blue is selected for initial position at the first grating and for initial velocity at the second. The beam's flight path is parallel to the ground so that gravity acts in the perpendicular direction. Given the time of flight (TOF)  $\tau$  between the two gratings and the vertical displacement  $\Delta y$ , the acceleration  $a$  can be calculated.

Reprinted from [12, p.11], by Guatieri Francesco, 2018, Trento. Reprinted with permission from the author.

In order to reach the goal of performing a gravity measurement for antimatter, three steps are envisioned:

- Produce a large quantity of cold antihydrogen using charge exchange between Rydberg excited positronium (atoms consisting of an electron and a positron, abbreviated with Ps) and trapped cold antiprotons.
- Use an electric field gradient to Stark accelerate the antihydrogen right after formation to form a pulsed beam with axial velocities of a few hundred meters per second.
- Send the beam towards a Moiré type deflectometer mounted downstream of the antihydrogen production region. Measure time and position of the antihydrogen atoms after they traversed the deflectometer with a detector to calculate the acceleration  $a$ .

Currently, the AEGIS collaboration is focusing its efforts on the first step which is covered in the following. Details about the second and the third step can be found in the proposal for the experiment [10].

The first step, namely the production of large quantities of cold antihydrogen, is based upon a charge exchange reaction that can be written as follows:



Rydberg excited positronium ( $Ps^*$ ) and an antiproton ( $\bar{p}$ ) combine to form an antihydrogen atom ( $\bar{H}$ ) and an electron ( $e^-$ ). Figure 2 shows the process of charge exchange as done in AEGIS.

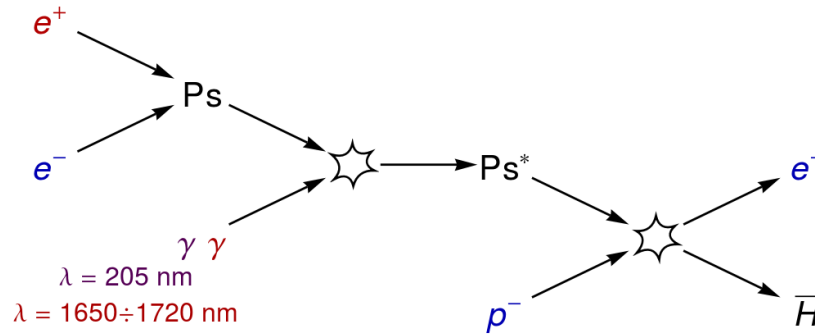


Figure 2: Schematic of the antihydrogen production process.

Positronium is generated by firing positrons onto a silicon converter target. After formation it is first excited to  $n = 3$  and then to Rydberg levels using two lasers. The Rydberg positronium is then combined with the trapped antiprotons to form antihydrogen.

Reprinted from [12, p.12], by Guatieri Francesco, 2018, Trento. Reprinted with permission.

The charge exchange reaction is a different approach than the direct mixing of antiprotons and positrons pioneered by the ATHENA collaboration to produce the first cold antihydrogen atoms in 2002 [13]. The main advantage of using charge exchange is that the temperature of the antihydrogen is given by the temperature of the antiproton. Using laser cooled negative ions to sympathetically cool antiprotons, temperatures in the mK range are deemed possible [14]. In comparison, during the direct mixing process of antiprotons and positrons, the antihydrogen heats up to temperatures about 20 times higher than the antiprotons from which they are formed [15].

The reason for using Rydberg excited over ground state positronium, which would be easier to produce, is that the production cross section for antihydrogen scales with the fourth power of the principal quantum number of the positronium [10, p.30].

The steps along the AEGIS apparatus that positrons and antiprotons go through before being combined to form antihydrogen will be explained in the following. All parts mentioned can be found in the overview of the AEGIS apparatus in figure 3.

The positrons needed for positronium are produced by a radioactive source of  $\beta^+$ -decaying  $^{22}\text{Na}$ . After emission, the positrons are trapped by a Surko-type trap which is unloaded every 152 ms into the following accumulator trap. For the 2018 antihydrogen production attempts, typically 420 pulses from the Surko trap are accumulated, making for an accumulation time of about 70 s. After that, the positrons are transferred towards the Off-Axis trap (as seen in figure 3) and onto a nanochannelled silica positronium converter. This positronium converter is located about 1.7 cm above the center of the antihydrogen production trap where the antiproton plasma is kept. In short, the Ps converter in the AEGIS experiment has a conversion efficiency of 35 %, meaning that 65 % of the incident positrons annihilate upon arrival. An electron-positron annihilation yields two 511 keV gamma-rays. The freshly produced positronium is then excited using two different lasers to first reach the  $n = 3$  level and then a Rydberg level (around  $n = 16$ ).

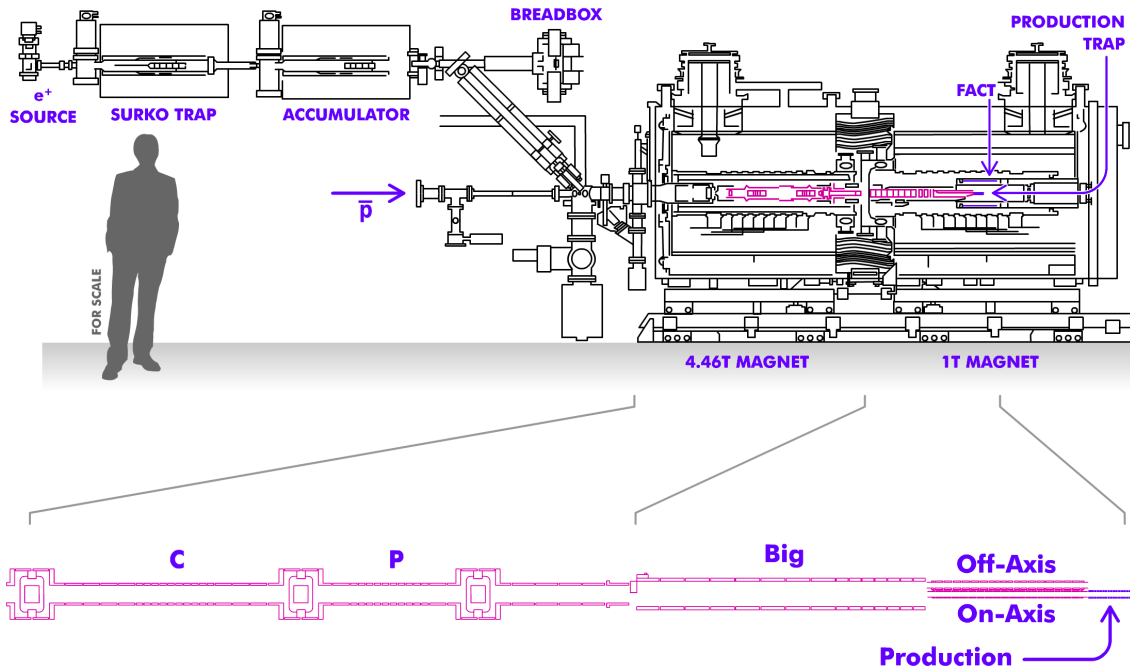
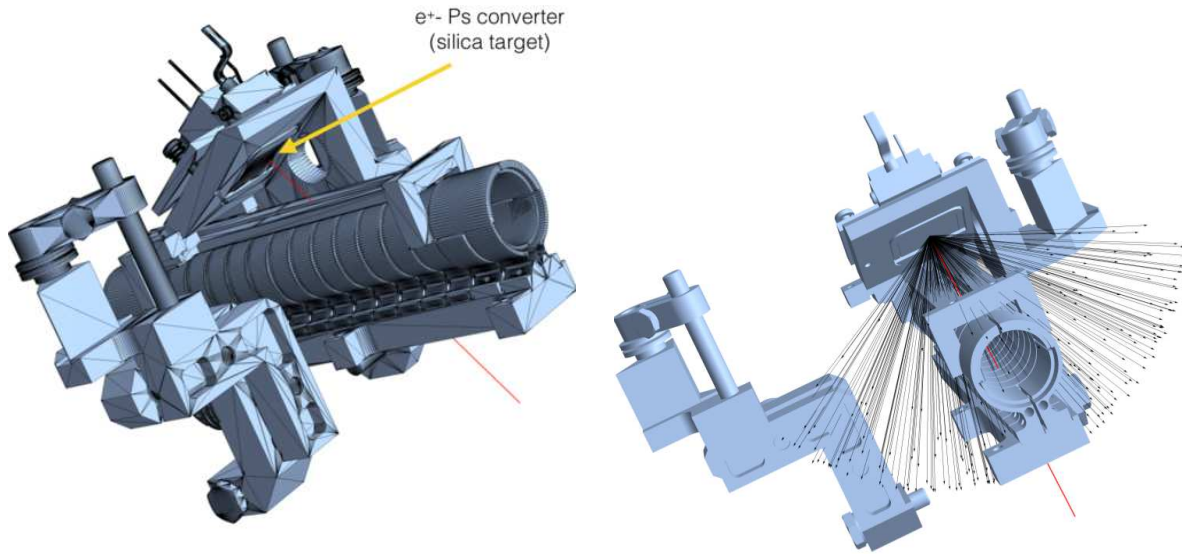


Figure 3: Schematic of the AEGIS experimental apparatus.

Reprinted from [12, p.13], by Guatieri Francesco, 2018, Trento. Reprinted with permission.

In parallel, the AEGIS apparatus is supplied with bunches of about  $3 \times 10^7$  antiprotons at kinetic energies of around 5.3 MeV from the AD every 100 s. This energy is too high for capture and therefore the antiprotons are moderated by being shot through a silicon-aluminum degrading foil. The coldest fraction below 9 keV is then captured by the first in a series of Penning-Malmberg traps in the 4.46 T region of the experiment. After compression and cooling with electrons, the coldest fraction is transferred to the production trap in the 1 T region. Recently new procedures have been developed to enable stacking multiple  $\bar{p}$  bunches from the AD to make for a denser plasma. The antiprotons are kept in the production trap to be combined with the Rydberg positronium generated at the target located just above the production trap. Details of the production trap and the positronium converter target are shown in figure 4.

The production trap which is the final trap of the apparatus is comprised of several cylindrical electrodes, as seen in figure 4a, with a radius of 5 mm. It features a segmented electrode for rotating wall compression of the  $\bar{p}$ -plasma. Using a multiple-step rotating wall compression process, the  $\bar{p}$ -plasma was compressed to sub-millimeter radial half-width-half-maximum (HWHM) values [17]. The trap features a grating directly underneath the positronium converter target so that the positronium enter the trap for the  $\bar{H}$ -production. Downstream of the production trap, where the proposed gravity module will be installed, a microchannel plate (MCP) detector is currently located. Due to its original purpose of detecting hydrogen, this detector is referred to as the hydrogen detector micro-channel plate (HDMCP). The  $\bar{p}$ -plasma can be shot from the production trap at this detector to gain insights into the plasma's properties such as radial density distribution and temperature.



(a) Detailed view of the production trap and the positron target.

The antiprotons are held in the segmented cylindrical trap while the electrons are shot on the nanoporous silica target marked by the yellow arrow.

Reprinted from [16, p.26], by Zurlo Nicola, 2018, Brescia. Reprinted with permission.

(b) Front view of the cone of positronium marked as the black lines which is produced by the target after being implanted with positrons.

Reprinted from [16, p.28], by Zurlo Nicola, 2018, Brescia. Reprinted with permission.

Figure 4

In summary, the complete  $\bar{\text{H}}$ -production scheme is comprised of the following steps:

- Antiprotons supplied from the AD are captured, cooled, compressed and stored in the production trap.
- Positrons from a  $\beta^+$   $^{22}\text{Na}$  source are trapped and accumulated.
- Once antiprotons are in the final trap, cooled sufficiently and enough positrons have been accumulated, the positrons are transferred and shot onto the converter target.
- Immediately after formation, two lasers are fired to excite the positronium to Rydberg levels.
- A fraction of the Rydberg positronium makes it into the trap and together with the antiprotons forms antihydrogen.

The newly formed antihydrogen is a neutral atom and therefore not confined by the electromagnetic fields of the production trap. Due to this lack of confinement the  $\bar{\text{H}}$  is expected to dissipate isotropically until eventually hitting an electrode of the final production trap (in principle the antihydrogen could also annihilate on a rest gas atom but given the vacuum of around  $1 \times 10^{-13}$  mbar to  $1 \times 10^{-15}$  mbar, this is very unlikely). On contact with the trap walls, the antihydrogen annihilates. With the purpose of measuring the charged particles produced in the  $\bar{\text{H}}$  annihilation, a cylindrical detector was built around the whole production region including the target. This detector is called FACT (**F**ast **A**nnihilation **C**ryogenic **T**racker) and its purpose is establishing antihydrogen production in the AEGIS experiment. The inner workings and analyses which can be done with this detector are the subject of this thesis.

## Content of this Thesis

The first chapter of this thesis covers the basics of the detector. This includes its purpose and mechanical design as well as the hardware and the control software used for operation. Next, the detector's reconstruction capabilities are assessed and a strategy for reconstructing tracks and vertices is derived. The last part of the first chapter provides an overview of the FACT part of the analysis software which was developed for data analysis in the AEGIS experiment. Appendix A then goes into the details of all relevant C++ classes and analyses created for this thesis. It is highly recommended for anyone looking to start analyzing FACT data to read those two sections.

Chapter two covers the derivation of an efficiency measurement method for FACT without the need of an external reference detector. By making use of the detector's tracking capabilities, the efficiency values of individual FACT channels can be measured. As a particle source charged pions from antiproton annihilations as well as cosmic muons can be used. After its derivation, the method's performance is tested using Monte Carlo simulated antiproton annihilations and cosmic muons. The strengths and current limitations of the method are explored and starting points for improvements are identified.

In the third and final chapter the results of applying the previously developed measurement method to antiproton annihilations and cosmic radiation are presented. Additionally, the possibility of cross-checking the measured efficiency values by time-resolved comparison between the FACT and another detector system in the AEGIS experiment is discussed. Finally, the results from chapter 3 are evaluated and suggestions for the next steps in the work with FACT are provided.

Additionally, this thesis features three appendices.

- Appendix A contains the previously mentioned description of the C++ analysis code.
- Appendix B covers the discovery and fixing of an error in the mapping between the numbers of individual FACT channels and their positions inside the detector.
- Appendix C features a list of all dead fibers which were identified during the efficiency studies.



Die approbierte gedruckte Originalversion dieser Diplomarbeit ist an der TU Wien Bibliothek verfügbar.  
The approved original version of this thesis is available in print at TU Wien Bibliothek.

# Chapter 1

## Introduction to FACT

Rise and shine, Mr. Freeman.  
Rise and shine.

— THE G-MAN  
*Half-Life 2*

The aim of the AEGIS collaboration is to perform a gravity measurement of antihydrogen. The first step in achieving this goal is demonstrating the production of antihydrogen. The antihydrogen will be synthesized by combining antiprotons from the AD and laser excited positronium produced through implantation of positrons into a nanoporous silica target. For demonstrating the production of antihydrogen, a detector called FACT (**F**ast **A**nnihilation **C**ryogenic **T**racker) was built around the  $\bar{H}$ -production region. FACT is a cylindrical tracking detector for charged particles that uses scintillating fibers as a detection medium.

The strategy for detecting and establishing the formation of antihydrogen in the AEGIS experiment works as follows:

The antihydrogen is formed through charge exchange between Rydberg positronium and antiprotons inside the production trap. The neutral antihydrogen will drift freely inside the ion trap, until eventually annihilating on the trap walls at a radial distance of 5 mm from the center of the trap. The two constituents of antihydrogen, the antiproton and the positron annihilate in two separate reactions. The electron-positron annihilation produces, most of the time, two 511 keV  $\gamma$ -particles while an antiproton annihilating on a matter nucleus results in, on average, 2.9 charged pions. An artistic interpretation of the annihilation process is shown in figure 1.1.

With plastic scintillating fibers<sup>1</sup> as a detection medium, FACT is built to reconstruct the charged pion tracks and find their common point of origin, the annihilation vertex. Due to the nature of the scintillating fibers, the detection efficiency for a  $\gamma$ -particle is in the order of  $1 \times 10^{-3}$ [18], meaning only an intense source of  $\gamma$ -radiation will cause the fibers to produce scintillation light. The approach to detect antihydrogen with the FACT detector is therefore to reconstruct the tracks and vertices of the charged pions from antiproton annihilations that occur as part of antihydrogen annihilations. By counting the amount of tracks and vertices and comparing this signal to the measured background, the formation of antihydrogen can be established. The precise assessment of the rates of the various sources of background is still ongoing and not part of this thesis.

---

<sup>1</sup>model SCSF-78M from Kuraray <http://kuraraypsf.jp/psf/sf.html>

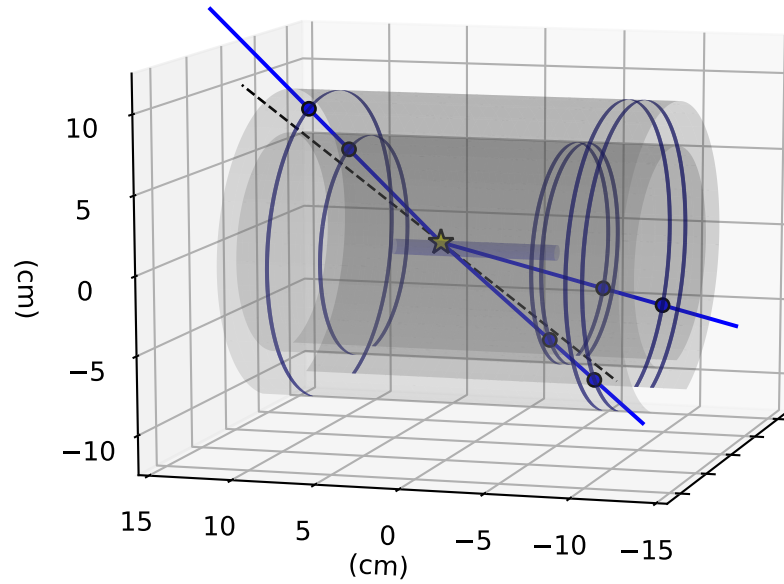


Figure 1.1: Artistic render of an  $\bar{H}$ -annihilation.

The charged pions are denoted as the blue solid lines and the gamma particles as the dashed black lines. The point of annihilation, the vertex, is marked as the yellow star. The innermost cylinder is the production trap. The outer two cylinders represent the FACT detector with the intersections of the pion tracks denoted as the blue dots while the rings represent the FACT fibers which register the hits. The dimensions of all three cylinders are to scale.

This first chapter focuses on how the signal is acquired. The detector is described in detail concerning its geometry as well as the electronic hardware and software. After that, the reconstruction strategies for tracks and vertices are discussed. Both the track and the vertex reconstruction are deduced in a mathematical way without detailing its software implementation. This will be covered in the very final part of this chapter together with the development of analysis tools.

## 1.1 Geometry and Hardware

### 1.1.1 Mechanical Design

The detector consists of 794 plastic scintillating fibers wrapped around two hollow cylinders. The cylinders are made from 7075 aluminum [19, p.3] and stacked inside each other, centered around the production trap. They are 240 mm long and feature inner radii of 68 and 96 mm respectively. In order to accommodate a connector that connects the scintillating fibers to clear fibers that transmit the scintillation photons to the sensors, both cylinders feature an opening. For the smaller cylinder this opening is  $22^\circ$  and for the bigger it is  $40^\circ$  as is shown in figures 1.2a and 1.2b. Since the scintillating fibers do not bridge the gap this limits the solid angle coverage of the detector. The apparatus is installed with the opening angle facing downwards.



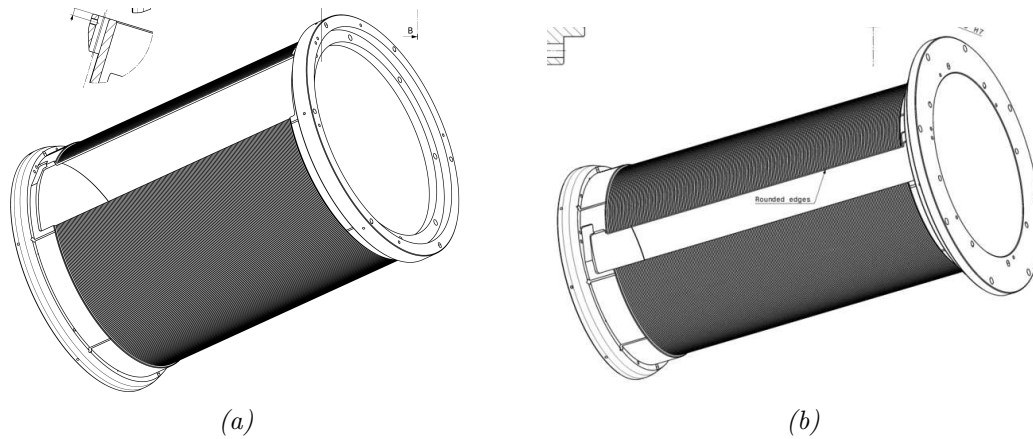


Figure 1.2: 3D views of the two FACT cylinders. In (a) the outer cylinder is shown, in (b) the inner.

Due to the detector's cylindrical symmetry, a cylindrical coordinate system is used, defined in figure 1.3: The axis that both the production trap and FACT are centered around is used as the  $z$ -coordinate. The center of FACT is used as the origin of this coordinate system and the positive direction is defined pointing downstream towards the proposed gravity module. The radius  $r$  is defined in the usual way for cylindrical coordinates and the angle  $\varphi$  is counted from the top so the geometry with respect to the opening of both FACT cylinders is symmetric.

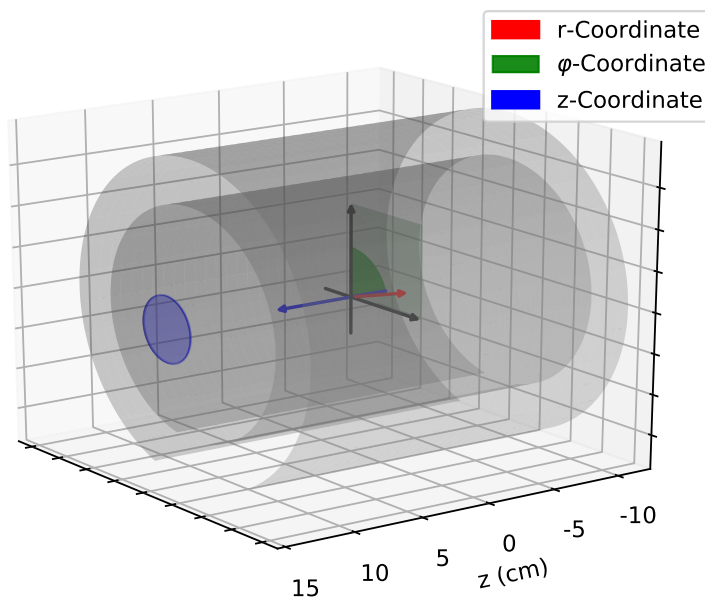


Figure 1.3: FACT coordinate system, with the axial coordinate  $z$  in blue, the radial distance  $r$  in red and the azimuth angle  $\varphi$  in green. The  $r$ - $\varphi$  plane, perpendicular to  $z$ , is denoted in light green. The blue circle represents the HDMCP located in the downstream direction of FACT.

The fibers of each of the two cylinders form the two super-layers of FACT. Each super-layer consists of two sub-layers arranged in a “circular-honeycomb” pattern, shown in figure 1.4. The lower sub-layer of each two super-layers rests in U-shaped grooves cut into the aluminum cylinders while the upper sub-layer rests in the gaps between the lower sub-layer’s fibers. In total, the fibers cover a length of 23.78 cm in  $z$ . The numbering convention for the fibers and the four sub-layers is also shown in figure 1.4.

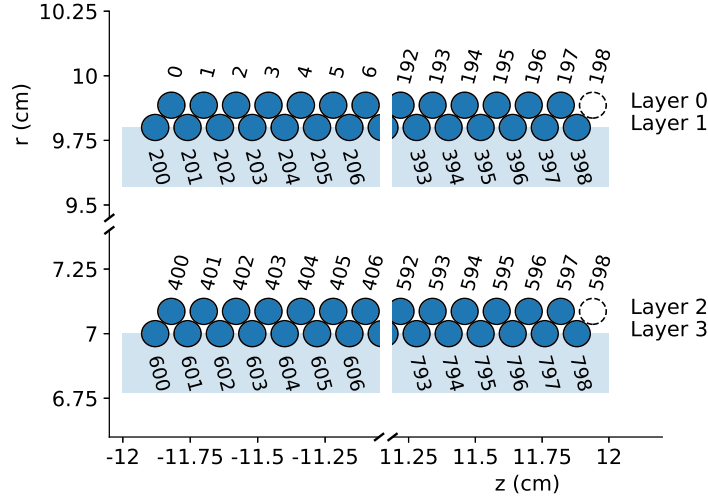


Figure 1.4: Illustration of the “circular-honeycomb” pattern of the layers. The slanted numbers indicate the fiber/channel numbers. Each layer starts with an integer multiple of 200. Due to the nature of the honeycomb layout, layers 0 and 2 feature one less fiber than layers 1 and 3, indicated by the dashed outlines at 11.88 mm in  $z$ .

The hollow aluminum cylinders are represented by the light blue area although the thickness is not to scale.

Layers 0 and 2 feature 198 fibers while layers 1 and three 3 consist of 199 making for a total of 794 fibers. The center positions of the layers are at 98.86, 98.0, 70.86 and 70.0 mm radially. Each fiber has a diameter of 1 mm, of which 94% are active scintillation area and the remaining 6% is cladding [20].

The scintillating fibers have one end connected to a clear fiber for readout while the other end is mirror coated to maximize the collection of scintillation photons. The mirrored end does not only maximize the photon yield but could also in principle enable the possibility to determine where along the fiber (i.e. in  $\varphi$ ) the charged particle crossed and generated the scintillation photons. Depending on the initial direction of the photons’ trajectories, towards the readout or towards the mirror, the sensors would register two temporally separated groups of photons. The expected time difference  $\Delta t$  as a function of the azimuthal origin of the photons  $\varphi_o$  (“o” for origin) can be calculated as follows:

After being generated at  $\varphi_o$ , the photons that fly directly towards the sensors need to cover a distance of  $s_1 = r \cdot \varphi_o$  ( $r$  being the radius of the FACT fiber) and the ones that initially fly towards the mirror have to cover  $s_2 = r((\varphi_{mirror} - \varphi_o) + \varphi_{mirror})$  ( $\varphi_{mirror}$  marks the end of the fiber). Using the difference in the paths  $\Delta s = 2r(\varphi_{mirror} - \varphi_o)$  and the speed of light inside the fiber  $c/n$ , the expression for  $\Delta t(\varphi_o)$  can be calculated<sup>2</sup>:

$$\Delta t(\varphi_o) = \frac{\Delta s}{v} = 2r(\varphi_{mirror} - \varphi_o) \frac{n}{c} \quad (1.1)$$

<sup>2</sup>The value  $\Delta t$  only serves as a lower bound estimation of actual time delay because the photons do not travel straight in the fiber but are reflected many times, making the effective path much longer.

The expression in equation 1.1 describes a linear relation between the angular origin point of the photons and the time delay that has its minimum at  $\Delta t(\varphi_o = \varphi_{mirror}) = 0$  s. In order to calculate the maximum delay, we're using the values for the outer FACT layer ( $r = 9.8$  cm and  $\varphi_{mirror} = \frac{16}{9}\pi$ ) as well as the fibers' refractive index  $n = 1.59$  [20]. This yields  $\Delta t(0) = 5.8$  ns. In order to reconstruct information in the  $\varphi$ -domain, a detector with a time resolution considerably smaller (depending on the desired accuracy) than 5.8 ns is needed. With the FACT FPGAs operating at a time resolution of 5 ns, this  $\varphi$  information is not obtainable. As a side note, even if the FPGAs operated at a higher frequency, the real bottleneck is the time it takes for a single photodiode to re-fire after the first wave of photons. As will be discussed in subsection 1.1.3, this recovery time is around 100 ns to 200 ns.

FACT can therefore be seen as a 2D detector measuring in  $r$  and  $z$  while integrating along the available  $\varphi$ -domain (i.e.  $2\pi$  minus the respective opening angles of the two hollow cylinders). This means that while in reality the intersection of a track and a fiber is a point, it is seen as the entire fiber by the detector (shown as the points and rings in figure 1.1). The implications of this limitation are addressed in subsection 1.3.2.

### 1.1.2 Nature of the signals in FACT

As mentioned in subsection 1.1 the detection principle used in FACT is the collection of scintillation light. As charged particles traverse polystyrene scintillators such as the FACT fibers they can excite electrons from the  $\pi$ -orbitals of the material's benzene rings. The photons emitted during the relaxation of the electrons can be detected as a measure of the energy deposited by the charged particle. In order to minimize losses due to scattering and re-absorption, the photons have to be shifted in wavelength. This is achieved by adding doping agents to the pure polystyrene.

For any scintillation detector it is essential to get an estimate of the amount of scintillation photons that are expected to be generated by the studied particles. The starting point for this approximation is the average travel distance of the particles through the detection medium. In our case we are looking at charged pions with energies in the minimum-ionizing region passing through fibers with a diameter of 1 mm. Using a Monte-Carlo simulation an average travel distance of around 0.72 mm was determined. Depending on the actual path length of the particle through the fiber, energy around  $(199 \pm 139)$  keV is deposited. This results in 1,400 to 2,000 scintillation photons. Around 5.4% or 100 of those scintillation photons are expected to be trapped inside the scintillating fiber and guided through clear fibers towards the photon sensors of FACT (all the numbers are taken from [21]).

### 1.1.3 Readout Electronics

Following the path of the scintillation photons as described in subsection 1.1.2 leads us to the detector's sensors. FACT uses a specific type of silicon photomultiplier (SiPM) called a multiple pixel photon counter (MPPC). An MPPC is made up from an array of individual avalanche photodiodes (10 by 10 individual pixels, with a total active area of 1 cm<sup>2</sup>) operated in Geiger mode. Geiger mode operation means that a single photon is enough to trigger an avalanche in the photodiode. The amount of signal generated hereby is independent of the amount of incident photons, i.e. a single photon produces the same output as one hundred, provided they hit the same pixel at the same time. In order to get information about the light intensity, a number of single photodiodes are combined and their signals superimposed to form an MPPC. This means that an MPPC acts as a discrete counter of the number of pixels which received at least one photon. The difference between number of incoming photons and firing pixels was addressed in [21]. Correcting the 100 incident photons for the around 35% detection efficiency of an MPPC, around

35 photons are expected to be detected. Using formula 24 from [22, p.21] we can take into account pixels which received more than one photon, resulting in the final estimate of around 31 pixels firing. After an avalanche has been triggered, the MPPC needs a certain time to restore 100 % of its gain. For the MPPCs used in FACT this time is in the order of 100 ns to 200 ns [22, p.22].

As with operating any avalanche photodiode, signals are not only generated by photons but also by thermally-generated carriers. Such signals are called dark pulses and cannot be distinguished from “photonic”-signals. At room temperature typical dark count rates are in the order of hundred kilohertz [21]. Since most of these dark counts are just single pixels firing, the largest fraction can be suppressed by setting a threshold on the output signal. In about 10 % of the cases when a pixel fires, secondary photons generated in the avalanche process can be detected by the neighboring pixels. This phenomenon is called optical cross-talk. In absence of an absolute calibration of the sensors the frequency of such high signal dark counts is used to adjust the gain settings to equalize the response of the MPPCs (as covered in section 1.2).

The FACT MPPCs are installed on half-moon shaped printed circuit boards (PCBs) in groups of 48 each, located inside the main apparatus’ vacuum. Mounted on these boards are PT-1000 thermoresistors [p.6][19] that measure the MPPCs temperatures<sup>3</sup>. It is very important to control the sensors’ temperatures because of the temperature dependency of the gain. The manufacturer of the FACT MPPCs Hamamatsu provides two graphs shown in figure 1.5 that are essential in understanding the working range of the sensors.

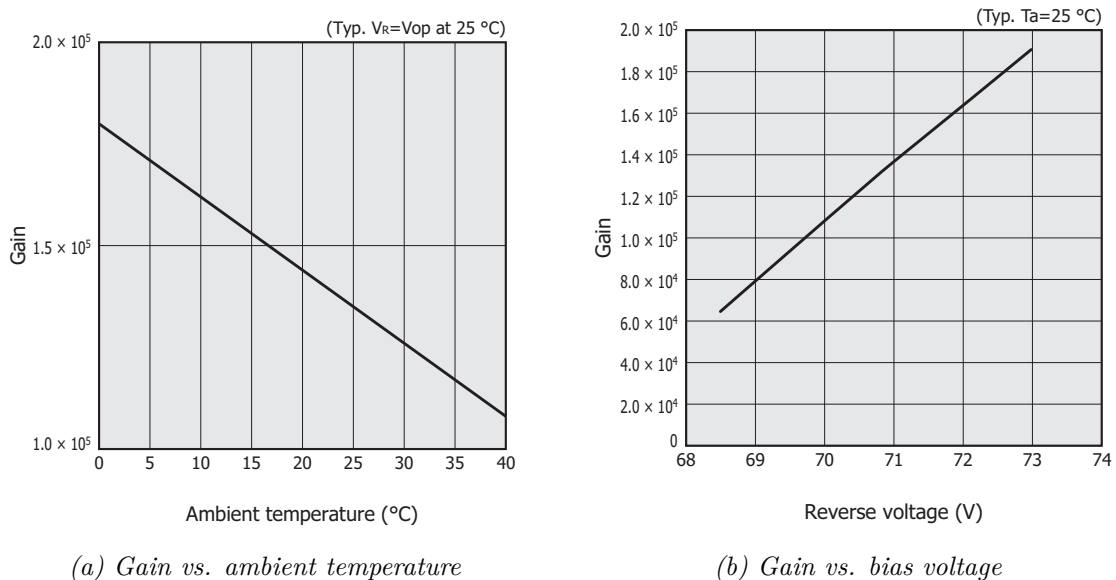


Figure 1.5: Reprinted from [22]. Reprinted with friendly permission of Hamamatsu Photonics.

Figure 1.5a shows the linear relation between the gain factor and the temperature for the MPPCs used in FACT. The change in gain per degree Celsius is about  $-1.8 \times 10^3 \text{ } ^\circ\text{C}^{-1}$ , meaning that the sensor becomes less sensitive, the hotter it gets. To put this in perspective, figure 1.5b displays the linear relation of bias voltage and gain factor. The recommended operating range of bias voltage from 68.5 to 73 V results in gain factors from  $6 \times 10^4$  to  $1.9 \times 10^5$ . However, due to a technical limitation<sup>4</sup> in the digital potentiometers that are used to apply the bias voltage to the MPPCs we are limited to a working range

<sup>3</sup><https://twiki.cern.ch/twiki/bin/view/AEGIS/FACTTemperatureControl>

<sup>4</sup>Details can be found here: <https://twiki.cern.ch/twiki/bin/view/AEGIS/FACTBiasSaturation>

from 69.9 to 71.1 V restricting the gain area to about  $3.5 \times 10^4$ . A change of  $1^\circ\text{C}$  corresponds to about 5% relative to the whole working range.

The temperature control of the MPPCs is only done passively by cooling the boxes that connect to the vacuum feedthroughs of the MPPC boards from the outside using fans. Each box houses 2 FPGAs and 4 analogue boards per FPGA. The fans' speed is adjusted using a PID controller according to the temperature measured on the corresponding MPPC half-moon board. In normal operation with the fans fully functional we observe different temperatures across the MPPC-PCBs as well as peak-to-peak differences in temperature of a few degrees during a 24 h day-night-cycle (as seen in figure 1.6).

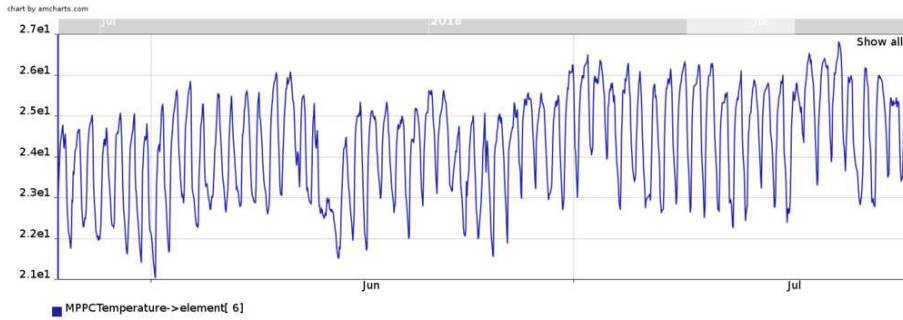


Figure 1.6: Temperature values are displayed in  $^\circ\text{C}$  on the y-axis for an MPPC board during the summer months of 2018. The minima correspond to the nights and the maxima to the days.

(Data taken from the AEGIS-DAQ online data browser)

In order to compensate for these drifts we periodically run an equalization routine that adjusts the gain of each MPPC to achieve a target dark-count rate in the order of 100 Hz. If the chosen gain ends up being in the upper end of the voltage working range, an increase in temperature can lead to problems. Particularly in the summer months it was observed that some boxes were running too hot, and cooling and maximum bias voltage were not enough to correct for the thermally induced loss in gain. Therefore an active temperature control with, for example, Peltier elements is an upgrade to consider.

Moving along the readout chain, the MPPC PCBs use feedthroughs to connect to analogue boards located outside of the apparatus. Each analogue board reads a group of 12 MPPCs. Here each MPPC's analog signal is amplified using a fixed gain linear amplifier. This signal is then discriminated and fed directly into one of 17 FPGAs<sup>5</sup>. The FPGAs are numbered from 0 to 15 plus one additional FPGA 17. FPGAs 0 to 15 are all connected to 48 MPPCs (i.e. 4 analog boards), except for the two border ones that contain one less MPPC as shown by the dashed fibers in figure 1.4. The MPPCs connected to those FPGAs are model S10362-11-100C from Hamamatsu.

FPGA 17 is only connected to 28 MPPCs of the different and newer type (S12571-100C) than the ones reading the rest of the fibers. These 28 channels are not only discriminated but were also digitized to gain a better understanding of the signal shape. The layout pattern of FACT is shown in figure 1.7.

A mapping is used that connects each “FPGA, MPPC” combination to the corresponding fiber number and position in  $z_{fiber}, r_{fiber}$  (as seen in figure 1.4). Details about the mapping can be found in appendix B.

<sup>5</sup>Xilinx Spartan-6 SP601

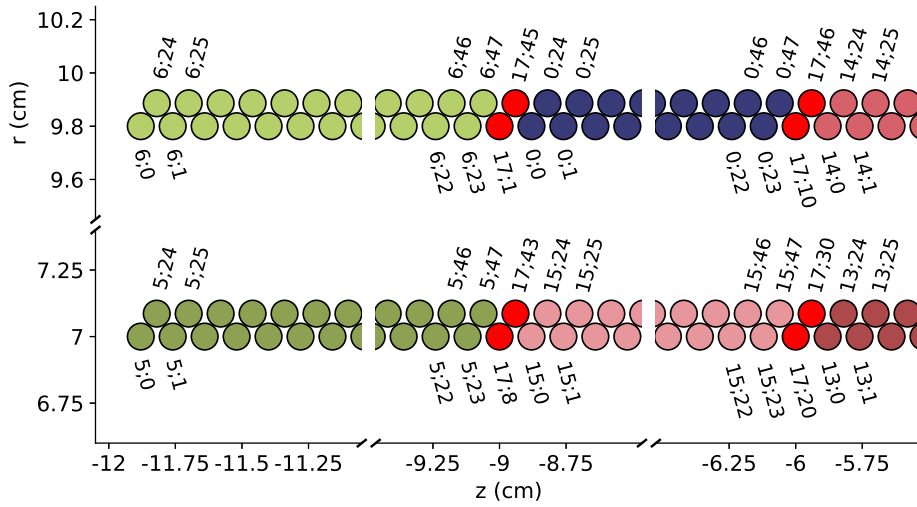


Figure 1.7: Layout of the first quarter of FACT. Fibers are grouped by colors according to their FPGAs. The numbers above and below the fibers represent the “FPGA, MPPC” combination. FPGA 0 to 15 always cover chunks of two times 24 fibers on the same super-layer while the fibers of FPGA 17 are separators between two consecutive FPGAs. The 28 channels of FPGA 17 are not numbered consecutively, and thus have numbers larger than 28.

The FPGAs also control the bias voltage that is applied to each MPPC as well as the discriminator threshold. The bias settings are determined by the aforementioned equalization routine for each MPPC individually and stored in a configuration file. *As an important side note*, in this configuration file the MPPC numbering starts at the number 1 while in the analysis software it starts at 0. This needs to be kept in mind when analysing single channels of FACT with respect to the bias settings.

The output of the discriminator is read by the FPGA at a rate of 200 MHz. This means that the FACT detector can detect the arrival of signals with a 5 ns resolution. For detecting back-to-back pions in the same sensor the limiting factor is the MPPC recovery time of around 100 ns to 200 ns.

Each FPGA groups its data together in Ethernet frames and sends it to main FACT control program called FACTDriver via Ethernet. At the end of each acquisition cycle, FACTDriver sends the data to the main AEGIS DAQ where it gets piped into ROOT files for analysis. Additionally, FACTDriver also saves a local copy of that data so that it can be recovered in the event of DAQ issues.

In order to start and end an acquisition a trigger gate is generated using an arbitrary waveform generator<sup>6</sup>. In our case a rectangular pulse with  $-1.3$  V acting as a gate signal is used.

## 1.2 Control Software

As mentioned in the previous section 1.1.3, the main driver software for the detector is a program called FACTDriver written in C++. Its main task is the communication with the FPGAs for acquiring data, setting the bias on the MPPCs and the threshold on the discriminators as well as handling the interaction with the DAQ system to ensure that the FACT data is saved.

<sup>6</sup>TTi TG5011

During an acquisition, before the FPGAs send their data to FACTDriver it is stored in their internal block random-access memory (BRAM). The format used is called a FACT word. A FACT word is an 88 bit long unit composed of a 32 bit time-stamp (in multiples of 5 ns), 48 bits for the discriminated state of the MPPCs (0 or 1) and 8 bits for 'fake' MPPCs for debugging purposes. A FACT word is written to the BRAM every time at least one fiber changes state (from 0 to 1 or the other way around). FACTDriver combines two words into a hit with the information on the FPGA and MPPC number, the starting time and how long it stayed on (time over threshold).

Depending on how the BRAM is handled during the course of an acquisition, we can distinguish between different FPGA operation modes set by FACTDriver.

The most simple mode is called *single*. In this mode the FPGAs acquire data, store it in their internal BRAM and wait with the sending until the trigger gate stops. The limiting factor is the size of the FPGAs BRAM. At 495.616 kbit or 5,632 FACT words at 88 bit each, it is rather small. In the absence of any signal, only considering the typical amount of 100 Hz of dark counts per fiber, this buffer fills up after around 1 s to 2 s. Due to the low event rate (a few  $\bar{H}$  per trial) and the short acquisition time (given the  $\bar{p}$ -plasma temperature, the  $\bar{H}$  is expected to annihilate within 100  $\mu$ s after production) the buffer size is sufficient for the  $\bar{H}$ -production procedure. For any gate length longer than this time or a high event rate, the FPGAs in *single*-mode are not able to record the full measurement. In order to bypass this limitation, two additional operation modes have been developed as detailed in appendix D of [12, p.218].

The first one is called *multiple*, here FACTDriver asks the FPGAs to send data as quickly as possible while clearing the buffer immediately after.

The second one, which is debugged thoroughly, and used in almost all cases at the current point in time, is called the *stream* mode. This mode uses the FPGAs BRAM as a circular buffer and sends data packets to FACTDriver spontaneously upon reception. Using this mode a maximum instantaneous rate of up to 3,000 Hz per fiber has been tested and confirmed to be working. As far as acquisition time goes the current limitation is the 32 bit time-stamp of the FACT words. The maximum number this 32-bit unsigned integer can represent is about  $4.29 \times 10^9$  and therefore the acquisition time is limited to  $4.29 \times 10^9 \cdot 5 \text{ ns} \approx 21.47 \text{ s}$ . In case this time is exceeded, the time-stamp is expected to wrap around which may cause undefined behavior. Such a limitation is nothing that cannot be solved by appropriate software measures, but it is currently not implemented, and therefore every FACT acquisition is limited to around 21.5 s.

Independent of the chosen operation mode, the FACTDriver work-cycle looks as follows:

1. Launch one thread per FPGA and establish Ethernet connections with the FPGAs.
2. Read bias and threshold values from configuration files and set them.
3. Arm the FPGAs and wait to receive trigger gate.
4. Start acquiring data after reception of trigger gate.
5. Handle the data according to the selected mode (*single*, *multiple* or *stream*).
6. After trigger gate stops, convert the received FACT words into hits with information about fiber number, starting time and time over threshold.
7. Open a connection to the AEGIS-DAQ and send the data. Save a copy of the data locally (to be able to recover data in case of DAQ issues).
8. Shut down.

In order to have FACTDriver running and ready to receive a trigger at any time a daemon called ObsessiveFACT is used. This program checks if there is a current instance of FACTDriver running and if not starts a new one.

For measurements of cosmic radiation where data needs to be acquired for hours another daemon has been developed. This daemon handles the interaction with the DAQ, FACTDriver and the trigger generator to continuously acquire data in 21.5 s chunks (details

on this program are given section 2.4). The daemon can be remote-controlled and vetos ObsessiveFACT in order to avoid collisions between the two programs.

In order to achieve a uniform response from the detector’s sensors in absence of a calibration with a well defined source, an auto-equalization routine based on the FACTDriver architecture is used. This routine sets the bias values for each MPPC according to a given target rate of dark counts. The higher the dark count rate, the higher the efficiency of detecting “real”-signals from scintillation photons. On the other hand the detector’s tracking abilities suffer with an increased “fake”-hit noise level. A compromise between single sensor efficiency and tracking efficiency was found at around 50 Hz to 100 Hz. Another reason to periodically run this equalization procedure is the temperature dependence of the sensors’ gains. As seen in figure 1.6 temperatures can drift during the course of an 8 h shift, where the experiment is supplied with antiprotons from the AD. In order to ensure comparability of the data across the whole shift the equalization routine should be run around once per hour. The details of the rate estimation and bias setting algorithm can be found in Appendix D.4 in [12].

For the control and operation of the detector and all its hardware we use a server called aegisfact1. This server is running FACTDriver, the equalization software, as well as all daemons mentioned above and a web-interface for quick and easy overview and control of the system. Through the web-interface the status of the detector can be checked, all power supplies of FACT components can be controlled and a trigger for the detector can be sent manually. Additionally cosmic ray acquisitions can be launched and controlled from there.

An overview of the FACT detector’s control and data handling system is shown in figure 1.8.

### 1.3 Data Analysis

Equipped with an understanding of the FACT’s hardware and control software we can now discuss the analysis strategy.

In the following two subsections we will derive a strategy to first reconstruct charged pion trajectories and then combine them to find annihilation vertices. As the FACT detector is not only used to track charged pions but also cosmic radiation, which requires a different approach in track reconstruction, this is covered as well.

In the last part of this section, the steps performed by the analysis software in order to get from single hits recorded by the detector’s MPPCs to particle tracks and annihilation vertices will be explained.

#### 1.3.1 Track Reconstruction

Each antiproton annihilation is expected to produce an average of around three charged pions. The aim is to reconstruct the trajectory of each pion and find their common point of origin, the annihilation vertex.

After production, the charged pions fly from the production trap outwards towards the FACT (the pion tracks are represented as blue lines in figure 1.1). Along their trajectory they are affected by the 1 T magnetic field in the axial direction that is used for radial confinement of the antiproton plasma. Since the magnetic component of the Lorentz force has the form of  $\vec{F}_B = q \cdot \vec{v} \times \vec{B}$  the radial velocity component  $v_r$  together with an axial magnetic field  $B_z$  will result in an azimuthal force  $F_\varphi$ . The result of this is a helical trajectory curved in the  $\varphi$ -direction. As discussed in section 1.1  $\varphi$ -information is not obtainable. Therefore, the real curved trajectory cannot be reconstructed and an approximation needs to be used. In the case of FACT the approximation of choice is a



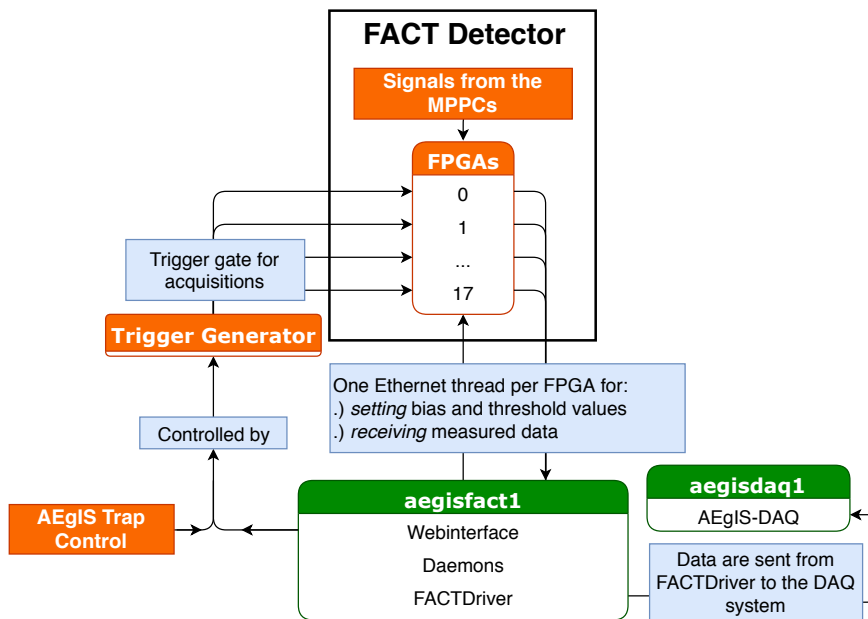


Figure 1.8: Schematic of the FACT detector's control and readout system. Control and measurement hardware is marked in dark yellow, the two servers are green and the blue boxes detail the type of connection between the components.

The primary server *aegisfact1* runs the web-interface, daemons for automated control tasks and *FACTDriver*. *FACTDriver* communicates via Ethernet with each FPGA and initially sets the bias and threshold values. Once the trigger generator, controlled either by the web-interface or the main AEGIS trap control system, sends a trigger gate to the FPGAs, signals from the MPPCs are recorded and sent to *FACTDriver* via Ethernet. After the acquisition is concluded *FACTDriver* sends the data to the AEGIS-DAQ system running on the *aegisdaq1* server.

straight line. The error that this simplification causes can be neglected in first approximation because the measurement of the particle's position happens at radial distances of 7 cm and 9.8 cm while the pions' trajectories are expected to have radii of curvature in the order of meters ( $r_{\text{measurement}} \ll r_{\text{curvature}}$ ).

The straight line needs to be transformed from its original Cartesian into the FACT coordinate system in  $r, z$ . The transformation is carried out as presented in [23].

A straight line in a three dimensional Cartesian coordinate system can be written as follows:

$$\begin{pmatrix} x \\ y \\ z \end{pmatrix} = \begin{pmatrix} x_0 \\ y_0 \\ z_0 \end{pmatrix} + t \cdot \begin{pmatrix} c_x \\ c_y \\ c_z \end{pmatrix} \quad (1.2)$$

where any point  $(x, y, z)$  along the line can be obtained by adding a multiple  $t$  of a direction vector  $(c_x, c_y, c_z)$  from an origin point  $(x_0, y_0, z_0)$ . Using the transformation into cylindrical coordinates the direction vector can be transformed in the following way:

$$\begin{pmatrix} c_x \\ c_y \\ c_z \end{pmatrix} = \begin{pmatrix} r_d \cos \varphi_d \\ r_d \sin \varphi_d \\ z_d \end{pmatrix} \quad (1.3)$$

The subscript “ $d$ ” stands for direction and denotes that  $r_d, \varphi_d$  and  $z_d$  are fixed values pointing in the direction of the line.

Looking at the  $r$ - $z$  plane one obtains:

$$r^2 = x^2 + y^2; t = \frac{z - z_0}{c_z} \quad (1.4)$$

$$r^2(t) = (x_0 + tc_x)^2 + (y_0 + tc_y)^2 = (c_x^2 + c_y^2)t^2 + 2(x_0c_x + y_0c_y)t + r_0^2 \quad (1.5)$$

Since the radial origin point  $r_0$  can be chosen freely along the line it is convenient to define  $r_0$  as the curve's minimum  $r_{\text{min}}$  with the corresponding curve parameter  $t_{\text{min}} = 0$ , resulting in:

$$r^2(t_{\text{min}} = 0) = r_0^2 = r_{\text{min}}^2 \quad (1.6)$$

By forcing  $t_{\text{min}} = 0$  and therefore  $r_{\text{min}} = r_0$ , a constraint can be obtained by looking at the definition of the minimum of the curve defined in formula 1.5,  $\frac{\partial(r^2)}{\partial t}(t_{\text{min}} = 0) = 0$ :

$$\frac{\partial(r^2)}{\partial t} = 2(c_x^2 + c_y^2)t + 2(x_0c_x + y_0c_y) \quad (1.7)$$

$$\frac{\partial(r^2)}{\partial t}(t = 0) = 2(x_0c_x + y_0c_y) = 0 \quad (1.8)$$

This equation can only be satisfied if  $(x_0c_x + y_0c_y) = 0$ . This drastically simplifies equation 1.5:

$$r^2(t) = (c_x^2 + c_y^2)t^2 + r_{\text{min}}^2 \quad (1.9)$$

with  $t = \frac{z - z_0}{c_z}$ :

$$r^2(z) = (c_x^2 + c_y^2)\left(\frac{z - z_0}{c_z}\right)^2 + r_{\text{min}}^2 = \frac{r_d^2(\sin^2 \varphi_d + \cos^2 \varphi_d)}{z_d^2}(z - z_0)^2 + r_{\text{min}}^2 \quad (1.10)$$

Arranging this into a more common form one obtains the equation for a hyperbola with its respective asymptotes:

$$\frac{r^2}{r_{min}^2} - \frac{r_d^2}{z_d^2 r_{min}^2} (z - z_0)^2 = 1 \quad (1.11)$$

$$r(z) = \pm \frac{r_d}{z_d} (z - z_0) = \pm \frac{1}{\tan \theta_d} (z - z_0) \quad (1.12)$$

This completes the transformation of the particle's trajectory from a straight line in a Cartesian coordinate system into a hyperbola in cylindrical  $r, z$  space. The hyperbola has three free parameters:  $r_{min}$  and  $z_0$  are the coordinates of the minimum point of the hyperbola known as the vertex (not to be confused with an annihilation vertex) and the term  $\frac{r_d}{z_d}$ . This term corresponds to the slope of the hyperbola's asymptote and can be interpreted as  $1/\tan \theta_d = \frac{r_d}{z_d}$  with  $\theta_d$  being the inclination angle. This angle is defined from  $-\pi/2$  to  $\pi/2$ , whereas a  $z_d > 0$  corresponds to  $\theta > 0$ .

In principle the hyperbola as given in formula 1.11 has two branches, one with  $r > 0$  and the other one with  $r < 0$ . Due to the definition of our coordinate space as cylindrical with  $r \geq 0$  we ignore the branch with negative  $r$  values. By arranging formula 1.11 for the positive branch of the hyperbola and using  $\tan \theta_d = \frac{z_d}{r_d}$  we get:

$$r = r_{min} \sqrt{1 + \frac{(z - z_0)^2}{r_{min}^2 \tan^2 \theta_d}} \quad (1.13)$$

A graphical interpretation of an example hyperbola<sup>7</sup> is shown in figure 1.9.

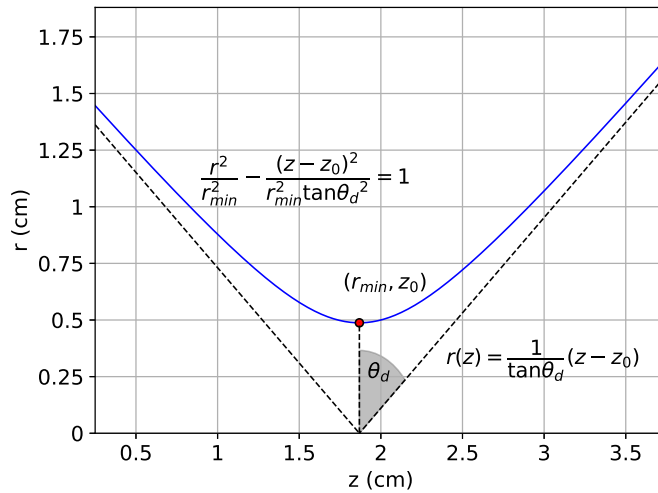


Figure 1.9: Illustration of an example hyperbola in blue with all three parameters  $r_{min}$ ,  $z_0$  and  $\theta_d$ . The hyperbola's vertex is marked in red and the two asymptotes are drawn as black dashed lines. The equation for the hyperbola as well as the right asymptote are displayed as well (for the left asymptote the sign of the  $\tan \theta_d$  expression is reversed).

In order to perform a reconstruction of the hyperbola, i.e. determine its three parameters, the track has to be measured at three different points in space.

<sup>7</sup>The exact hyperbola in figure 1.9, as well as the underlying 3D-track, are also used in figures 1.11, 1.12, 1.13 and 1.14 and consistently color-coded in blue.

In principle FACT features a total of four layers so we should get four different points. However, the layers are not evenly spaced but arranged as two super-layers comprised of two sub-layers each (as seen in figure 1.4). Inside each super-layer, the sub-layers have radial distances of 0.82 mm. This means that despite having four layers, the detector acts as two layer device with improved spatial resolution as well as higher detection efficiency compared to just two single layers.

For the reconstruction process we group neighboring fibers that fire at the same time into clusters (illustrated in figure 1.10). The position of the cluster is calculated as the average position of its constituent fibers.



Figure 1.10: Clustering process for six individual fibers firing (marked in red). The raw fibers are shown on the left and the clusters, marked by the hatching, on the right. The leftmost cluster has the typical shape one would expect. The middle “single-fiber” cluster can occur as a result of inefficiencies in the lower layer or a dark count causing in a single fiber to fire. The rightmost cluster can be the result of a particle track crossing the fibers at a shallow angle.

For each particle crossing the detector we get one cluster for every super-layer, rendering full reconstruction of the hyperbola impossible. The closest geometric object that contains two of the hyperbola’s parameters, namely  $z_0$  and  $\tan \theta_d$ , and therefore in principle can be reconstructed is its asymptote<sup>8</sup>. The problem with this is that FACT, as any other tracking detector, measures points along a particle’s trajectory, and not its asymptote. What is obtained by fitting a line through the two intersection points ( $(z_1, r_1 = 7.041 \text{ cm})$  and  $(z_2, r_2 = 9.841 \text{ cm})$ )<sup>9</sup> with the detector is in fact a secant to the hyperbola as shown in formula 1.14:

$$r(z) = \pm \frac{1}{\tan \theta_s} (z - z_s) \tag{1.14}$$

with  $\tan \theta_s$  corresponding to  $\tan \theta_d$  and  $z_s$  to  $z_0$ , as the real asymptote’s parameters (the subscript “s” stands for secant). In analogy to the hyperbola’s two asymptotes the  $\pm$  represents the reflection of the secant across a vertical line at  $z_s$ . During an actual detection process, only one of the two secants is measured, however, the mirroring is needed for vertex reconstruction as detailed in the following subsection. The two measurement points available for determining  $\tan \theta_s$  and  $z_s$  are sampled from the real hyperbola:

$$z(r) = z_0 \pm r_{min} \tan \theta_d \sqrt{\frac{r^2}{r_{min}^2} - 1} \tag{1.15}$$

The first parameter  $\theta_s$  is determined as the following expression:

<sup>8</sup>This approach for the reconstruction of tracks and subsequently vertices is outlined in [24].

<sup>9</sup>Here the mean radial positions of the two super-layers are used. Depending on the cluster layout the radial position can vary between the upper and lower sub-layer. The mean radial position is used throughout the tracking and vertexing algorithm including all corresponding illustrations (sections 1.3.1 and 1.3.2).

$$\tan \theta_s = \frac{\Delta z}{\Delta r} = \tan \theta_d \frac{r_{min} \left( \sqrt{\frac{r_2^2}{r_{min}^2} - 1} - \sqrt{\frac{r_1^2}{r_{min}^2} - 1} \right)}{\Delta r} = \tan \theta_d \cdot \alpha(r_{min}) \quad (1.16)$$

with  $\Delta r = 2.8 \text{ cm}$  being the fixed radial distance between the two sampling points and  $\alpha(r_{min}) > 1$  the factor that carries the  $r_{min}$  dependency and relates the two tangent expressions.

The error in the estimation of  $\tan \theta_d$  is comprised of the  $\alpha(r_{min})$  term as well as the  $\tan \theta_s$  term:

$$\Delta \tan \theta(\tan \theta_s, r_{min}) = (\tan \theta_s - \tan \theta_d) = \tan \theta_s \left( 1 - \frac{1}{\alpha(r_{min})} \right) = \tan \theta_s \cdot \alpha'(r_{min}) \quad (1.17)$$

with the parameter  $\alpha'(r_{min}) > 0$  for easier notation. An interesting point to note here is that the error on the  $\tan \theta_s$  estimation is proportional to the value of  $\tan \theta_s$  itself.

The second parameter  $z_s$  is obtained by rearranging equation 1.14:

$$\begin{aligned} z_s &= z_1 - \tan \theta_s r_1 = z_0 + r_{min} \tan \theta_d \sqrt{\frac{r_1^2}{r_{min}^2} - 1} - r_1 \tan \theta_s = \\ &= z_0 + r_{min} \frac{\tan \theta_s}{\alpha(r_{min})} \sqrt{\frac{r_1^2}{r_{min}^2} - 1} - \tan \theta_s r_1 = z_0 + \tan \theta_s \left( \frac{r_{min}}{\alpha(r_{min})} \sqrt{\frac{r_1^2}{r_{min}^2} - 1} - r_1 \right) = \\ &= z_0 + \tan \theta_s \cdot \beta(r_{min}) \end{aligned} \quad (1.18)$$

with the term  $\beta(r_{min})$  being strictly smaller than 0 the error in  $z$  looks as follows:

$$\Delta z(\tan \theta_s, r_{min}) = z_s - z_0 = \tan \theta_s \cdot \beta(r_{min}) = -\tan \theta_s |\beta(r_{min})| \quad (1.19)$$

Looking at equations 1.17 and 1.19 it becomes apparent that the two expressions carry opposite signs. For  $\tan \theta_s > 0$  (i.e. the “right” asymptote as seen in figure 1.9) the angle will be overestimated, while  $z_0$  will be underestimated. For  $\tan \theta_s < 0$  the opposite happens.

With these expressions now derived we can assess the errors quantitatively. As deduced before, the reconstruction strategy does not yield a value for  $r_{min}$ , therefore both error expressions cannot be used directly. What can be done, however, is assess the worst-case scenario. Both error terms increase as their variables,  $\tan \theta_s$  and  $r_{min}$  increase. In order to get an idea of the worst-case, the maximum for both has to be found.

For  $r_{min}$  the maximum is obtained easily since the trajectory of the antihydrogen is limited by the trap electrodes at  $r = 0.5 \text{ cm}$ .

The antiproton plasma used to form the antihydrogen is held in the section of the production trap around the center of FACT, i.e.  $z = 0$ . Therefore the tangent of the maximum angle that FACT is expected to record is around  $\pm \frac{12}{10} = \pm 1.2 = \tan \theta_s$  with a corresponding angle  $\theta_s = \pm 50.2^\circ$ .

With this we can get worst-case values for  $\alpha'$  and  $\beta$  as well as the errors. Table 1.1 provides an overview of all worst-case values.

As is shown in table 1.1 the errors presented in the last two columns are rather small. In the case of  $\Delta z$ , around  $\pm 0.4 \text{ mm}$  are expected. This is smaller than the diameter of the scintillating fibers and does not dramatically impact the detector’s tracking capabilities. The reason for the error being so small lies in the square root terms from equation 1.16 that are approximated when using the secant as the asymptote:

Table 1.1: Overview of the worst-case values for an antihydrogen annihilation tracking scenario. The  $\mp$  in the last column denotes that the sign of the error  $\Delta z$  is always opposite of  $\Delta \tan \theta$ , which inherits its sign from the  $\tan \theta_s$  value.

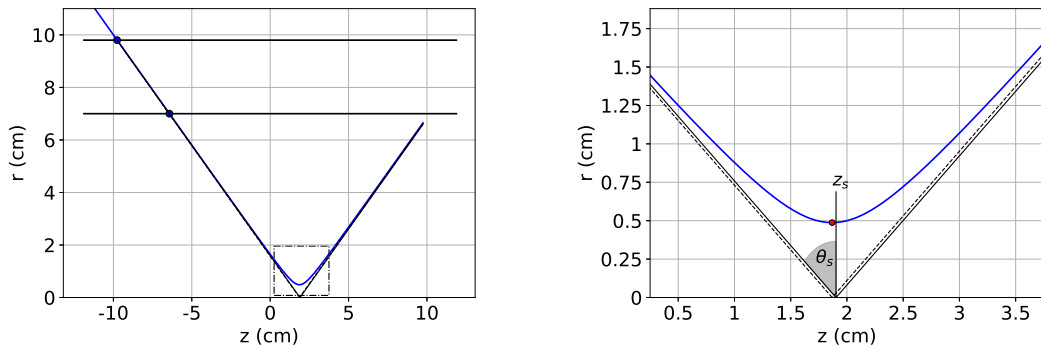
$\tan(\pm 50.2^\circ)$	$\alpha'(0.5 \text{ cm})$	$\beta(0.5 \text{ cm})$	$\Delta \tan \theta$	$\Delta z$
$\pm 1.2$	$1.81 \times 10^{-3}$	$-3.0 \times 10^{-2} \text{ cm}$	$\pm 2.2 \times 10^{-3}$	$\mp 3.65 \times 10^{-2} \text{ cm}$

$$\sqrt{\frac{r_{1;2}^2}{r_{min}^2} - 1}; \sqrt{\frac{7.041^2}{0.5^2} - 1} \approx \sqrt{196 - 1} \approx \sqrt{196} \quad (1.20)$$

with  $r_{1;2}$  as a shorthand for  $r_1$  and  $r_2$ . Since the  $r_{1;2}^2/r_{min}^2$ -term is more than two orders of magnitude bigger than 1, the error becomes small. In other words, the FACT detector gains accuracy by being further away from the annihilation vertex.

The most important column in table 1.1 is the last one, the error in  $z$ . This is because  $z_0$  is an approximation for the  $z$ -coordinate of the particle's origin point, the annihilation vertex. Now, it has to be stated that the annihilation vertex and the track's minimum don't necessarily coincide. In principle the particle can originate at any point along the hyperbola from figure 1.11a with  $r < 7 \text{ cm}$ . However, since the trap electrodes confine the area of origin to  $r \leq 5 \text{ mm}$ , the worst-case difference between  $z_0$  and the particle's annihilation vertex  $\pm 6 \text{ mm}$ .

Additionally, it is notable that both error terms are functions of  $r_{min}$  and  $\tan \theta_s$  while being independent of  $z$ . An intuitive explanation for this is that  $z_0$  is the only one of the three hyperbola parameters that preserves cylindrical symmetry. The approximation of the asymptote with the secant is illustrated in figure 1.11:



(a) The two horizontal lines at 7.041 cm and 9.841 cm represent the FACT detector and the two blue dots the intersection of the track with the detector, i.e. the fibers that produce scintillation light. The size of the dots is exaggerated with respect to the real fiber size. The dash-dotted frame shows the area that is zoomed in at figure 1.11b

(b) Detailed view of the hyperbola-vertex region. The red marker represents the hyperbola's real vertex. The reconstructed angle  $\theta_s$  is shown in grey and the approximation  $z_s$  for the  $z$ -coordinate of hyperbola vertex is denoted by a vertical line.

Figure 1.11: Illustration of a reconstruction situation with an example track in blue. The asymptotes are represented as dashed lines and the reconstructed secants as solid lines.

In conclusion we have now developed an understanding of the properties of the particle tracks, namely  $z_s$  and  $\tan\theta_s$ , we can reconstruct. Utilizing a reconstructed secant as an approximation for the hyperbola's asymptote which in turn is used as a proxy for the actual hyperbola, we are able to produce estimates for two out of the three parameters. Additionally, we have found expressions for the expected errors. Since both terms contain  $r_{min}$  which cannot be reconstructed, they cannot be used to correct the estimates directly. They could, however, be used when comparing reconstructed secants to each other.

The main shortcoming of the single track reconstruction process is that it doesn't yield a value for  $r_{min}$  and that the track's minimum ( $z_0, r_{min}$ ) does not necessarily coincide with the particle's origin point. However, as stated before, the difference between the particle's vertex and  $z_0$  is at most  $\pm 6$  mm. The main appeal of using the  $z_s$  distribution of single tracks is that it only requires very little information. Out of the on average 3 charged pions per antiproton annihilation, FACT only needs to record a single pion with one hit in each super layer, making this method robust against detector inefficiencies. Due to the combination of inefficiency robustness and sufficient accuracy, the distribution of the  $z_s$  values has proved itself a valuable tool and is used on a frequent basis in the AEGIS experiment. It is employed not only for antihydrogen production analysis but also to get insights into antiproton plasma dynamics for the development and debugging of new trapping schemes.

As far as the  $\tan\theta_s$  value goes the usability is limited. Since an angular isotropic emission spectrum is expected there is not too much that can be deduced from a  $\tan\theta_s$ -distribution.

In order to get an estimate of the actual annihilation vertex, at least two tracks need to be used. The strategy for this is presented in subsection 1.3.2.

### 1.3.2 Vertex Reconstruction

More meaningful analysis results for antiproton annihilations can be obtained by combining two or more tracks, to find their common point of origin, the annihilation vertex. The coordinates of the real annihilation vertex are called  $(z_v, r_v)$  in the following.

In principle an antiproton annihilation can produce more than two charged pions, nonetheless, the reconstruction algorithm will be deduced on the basis of a two pion/track annihilation. The reason for this is that the two track case is the most simple and at the same time most likely scenario to be detected by FACT as presented in [24, p. 4-5]. Additionally the two track algorithm will be able to handle three or more track cases as well. For three tracks originating from the same vertex, the two track algorithm will produce three vertices instead of a single one. The algorithm will therefore overestimate a signal and worsen the spatial resolution. Since tracking as well as vertexing is only performed on hits in the same time-window (typically 5 or 10 ns) the potential overestimation of a signal in a counting experiment can be circumvented by counting the number of time-windows that contain at least one vertex, instead of counting the number of vertices. As far as improving the detector's resolution goes, however, developing algorithms for three or more tracks might be a viable option for the future.

An artistic render of a two pion antiproton annihilation is presented in figure 1.12. In reality, the firing fibers in FACT are not color-coded so that it is not clear which upper and lower super-layer hits belong together to form the tracks. The way in which the issue of combinatorics is addressed will be covered at the end of this section. For explaining the vertexing mechanism, however, the color coding will be used.

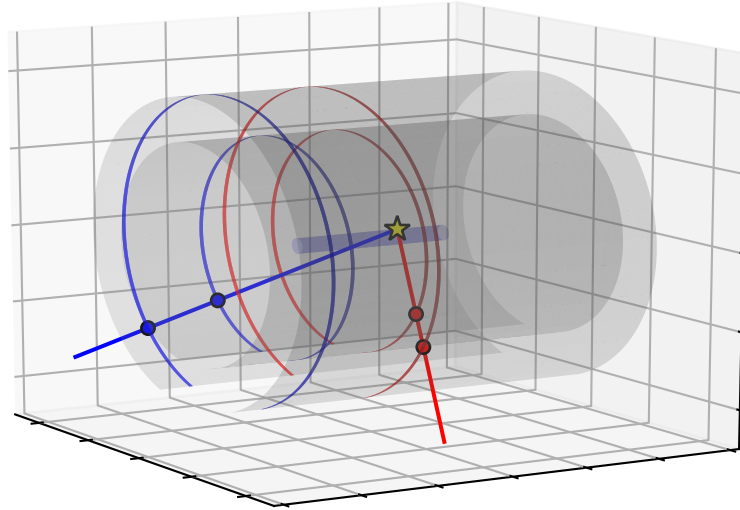


Figure 1.12: Example of an antiproton annihilation into two charged pions. The annihilation vertex is marked as the yellow star. It is located on the wall of the production trap represented by the smallest inner cylinder. The two tracks are color coded in red and blue as are their respective intersection points with the super-layers and the corresponding fibers which light up. The firing “fibers” are drawn to about twice the actual size for better visualization.

As derived in the preceding subsection, the information obtained from a particle track is quite limited and does not go beyond the fitting a straight line through two points. Therefore, the approach to find the common point of origin for two tracks cannot go beyond an approximation as well. In principle the process of finding the vertex approximation is rather straightforward, since it just involves fitting two secants through two points each and then intersecting them (both the reconstructed secants and their respective reflections). However, there is one caveat as seen in figure 1.13:

From initially just one common point, the “star” vertex from figure 1.12, now the curves seem to have two intersections. Mathematically speaking this is expected since according to Bézout’s theorem the number of intersection points of two curves is equal to the product of their degrees. Since two second degree polynomials are intersected, one would in principle expect four points but because we limit our coordinate space to  $r \geq 0$  this number is halved. A more intuitive explanation is that by taking away one coordinate, namely  $\varphi$ , the intersection of the tracks that originally only had one solution (the vertex as seen in figure 1.12) now becomes ambiguous, providing two possible solutions.

So although the fact that one ends up with two intersection points is expected, it is still a problem, since only one of the points corresponds to the real intersection point of the two 3D-curves. According to [24] the correct vertex is in almost all cases the one with the lower  $r$  value.



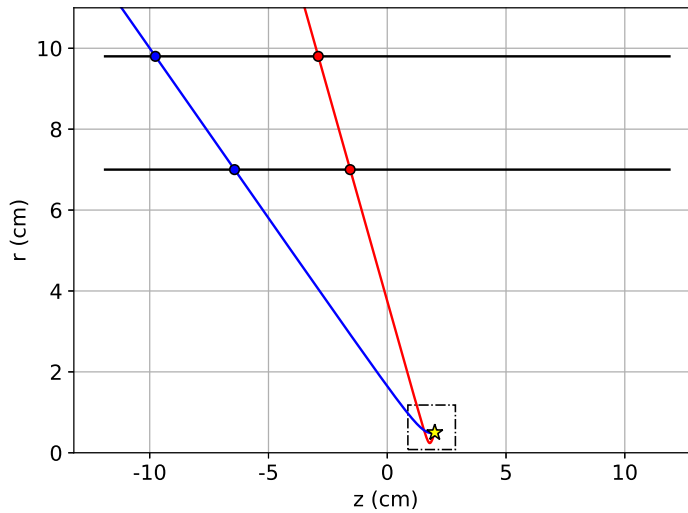
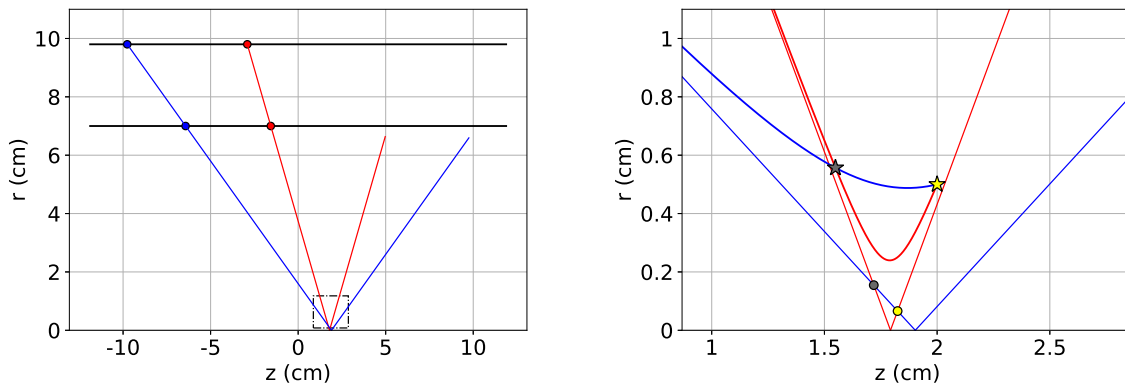


Figure 1.13: Direct conversion of the tracks and hits from figure 1.12 into FACT coordinates. The yellow star marks the annihilation vertex, however, a second intersection point emerges. The dash dotted window shows the intersection region that is presented enlarged in figure 1.14b.

With an understanding of the vertexing task and all tools for track reconstruction derived, an example reconstruction scenario is shown in figure 1.14:



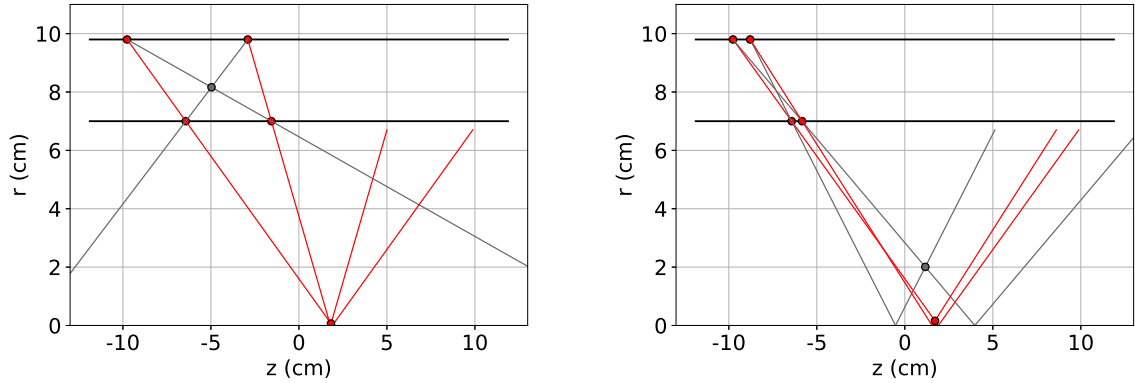
(a) View of the secant reconstruction for the two tracks from figure 1.13. The dash-dotted box shows the vertex region which is presented enlarged in figure 1.14b.

(b) This illustration shows both vertex regions from figures 1.13 and 1.14a. The secants are matched in color to their respective hyperbolae. The two stars mark the two intersection points of the hyperbolae with the yellow star denoting the real and the dark grey the fake vertex. The same color coding has been used for the circles that represent the intersections of the secants, i.e. the reconstructable vertex approximations.

Figure 1.14

As seen in figure 1.14b, the two secants intersect in two places as well and again the point with the smaller  $r$  value is the better approximation for the vertex. This point shall be referred to as  $(z_{reco}, r_{reco})$ . From numerical simulations presented in [24] we know that for the reconstructed and the real vertex the following relation holds  $r_{reco} \leq r_v$ . In any given reconstruction scenario the detector will always underestimate and maximally equal the radial position of the actual vertex.

Coming back to the issue that in a real reconstruction scenario, the firing fibers are of course not color coded. This produces the problem of choosing the correct two fibers for the tracks and subsequently the vertices. Two example situations are illustrated in figure 1.15.



(a) Same hit combination as in figure 1.14a. Choosing the correct combination is easy since the two grey lines intersect in-between the detector layers. Additionally both grey lines have  $z_s$  values that lie beyond the detector volume, where no particle is expected to originate from.

(b) Different hit combination, where the track on the right was moved closer to the one on the left. This leads to a more problematic, less obvious situation, since both the grey and the red tracks intersect inside the detector volume. Also the  $z_s$  value of both grey tracks are within the detector volume and cannot be excluded a priori.

Figure 1.15

The two situations from figure 1.15 are just two example cases but they serve to illustrate the problem of track multiplicity. As soon as there are four<sup>10</sup> or more clusters, the reconstruction task for tracks and vertices is no longer unambiguous. The number of possible tracks is equal to the product of the number of hits on the upper and the number of hits on the lower layer. In case of figure 1.15 we have the relatively small number of  $2 \times 2 = 4$  possible tracks, but in case of three or more charged particle tracks or noise hits this number can quickly become large. In an attempt to identify the correct tracks and in turn vertices we have to look at the properties we can reconstruct.

The only information that we obtain from a track is the  $z_s$  value and the angle  $\theta_s$ .  $\theta_s$  holds no information on whether or not a combination is correct since we expect angular isotropy in the charged pion emission spectrum. Given the region in  $z$  where the annihilations are expected to originate from,  $z_s$  can be used to exclude certain combinations. For antihydrogen production the region depends on the exact trapping configuration. Generally speaking, any track that originates from outside of FACT can be excluded. Looking at figure 1.15a both grey tracks could be eliminated, however as seen in 1.15b it can happen

<sup>10</sup>i.e. the minimum requirement for any kind of vertex reconstruction

that both fake tracks have  $z_s$  values which are well within the expected region. For vertices the situation looks better since in most cases only one intersection point will have a value of  $r_{reco} \leq 5$  mm (i.e. inside the production trap). It is not guaranteed, however, that only one combination fulfills this criterion.

In order to realistically assess the detector's vertex reconstruction capabilities accounting for all uncertainties regarding the errors in the reconstruction, the track multiplicity and the finite resolution of the 1 mm diameter fibers, a Monte Carlo simulation was developed. The main points, as presented in [24], are:

- Without any noise in the detector, the annihilation vertex of a two pion decay can be reconstructed with a resolution of about 6 mm in  $z$ .  $z_{reco}$  also serves as an unbiased estimator for  $z_v$ .
- The error in  $r_{reco}$  scales linearly with  $r_v$ . Additionally, for  $r_{reco}$  the relation  $r_{reco} \leq r_v$  holds.
- The  $r$  resolution is not good enough to infer any details about the processes inside the production trap ( $r \leq 5$  mm).
- Since we cannot say for sure which hits on the upper and lower super-layer belong together all possible combinations are considered. However, with cuts in  $r$  and  $z$  nonphysical cases can be ruled out and the number of fake tracks and vertices can be reduced.

For the detection of antihydrogen this lack of  $r$ -reconstruction capability is bad news. This is because one of the main sources of background in detecting antihydrogen is annihilations of antiprotons. Those annihilations can happen in one of two ways. An antiproton can be too fast to be contained by the trap and fly off until eventually hitting the trap wall in the same way as antihydrogen is expected to do. As from the detector's point of view an antiproton and an antihydrogen annihilation already produce the same particles, distinguishing one from the other becomes impossible if both also happen at the same radial distance.

The second way, however, is annihilation on rest gas atoms while still being held at the center of the trap. As was covered in this section, the FACT's radial resolution is unfortunately not sufficient to distinguish between annihilations in the center of the trap and the trap walls.

Nonetheless, there is valuable insight to be gained from reconstructing tracks and vertices. The software that was developed for performing these reconstruction steps from the ROOT-files which are produced by FACTDriver to the final plots used for analysis is subject of subsection 1.3.4.

### 1.3.3 Cosmic Ray Tracking

While subsections 1.3.1 and 1.3.2 focused on approximating the tracks and vertices of charged pions, there is one use case of FACT where full hyperbolic track reconstruction is possible. This is the detection of cosmic minimum-ionizing charged particles, mainly muons. Due to the fact that these muons originate from outside of the detector they cross each super-layer twice. This results in a typical amount of eight fibers firing, that are combined to form four clusters. Using these four clusters, estimates for the three parameters of the hyperbola ( $r_{min}, z_0, \theta$ ) can be obtained. An example of a cosmic muon track is illustrated in figure 1.16.

The four intersection points of the muon track with the super-layers of FACT will always form a trapezoid shape as seen in figure 1.16b. More specifically they form an isosceles trapezoid where the side along the upper super-layer will always be longer or equal than the side along the lower super-layer. This characteristic "cosmic-fingerprint"

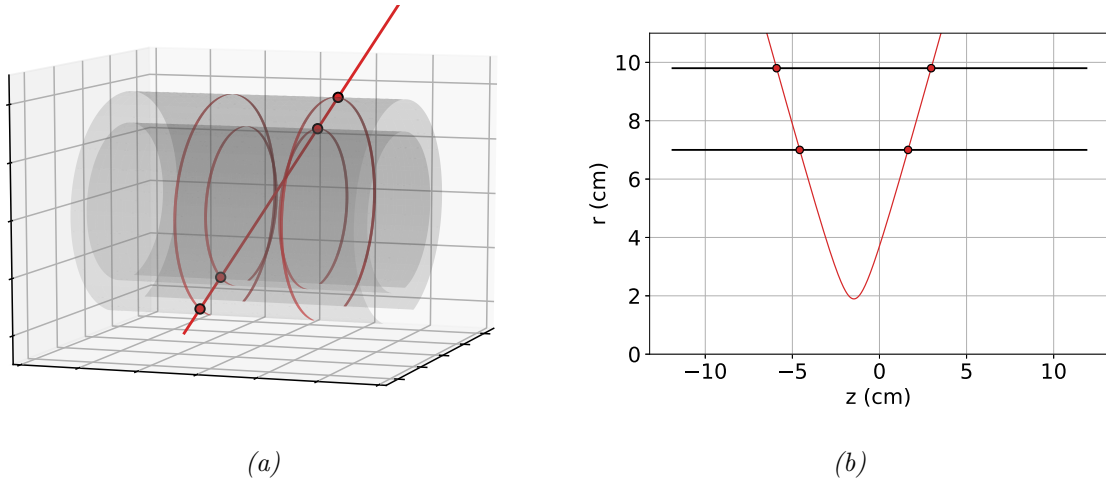


Figure 1.16: Illustration of a cosmic muon crossing FACT. A 3D view is shown in (a) and the 2D conversion in (b). Each super layer is crossed twice, resulting in four clusters, enabling the reconstruction of the hyperbola in figure 1.16b. Figure 1.16b also shows the hit characteristic hit pattern in form of an isosceles trapezoid. It is referred to as a “cosmic-fingerprint”.

is used to identify cosmic rays in FACT. Since the hyperbola has three parameters, the reconstruction can still be performed if one of the corners of the trapezoid is missing. In fact, a hyperbola can already be reconstructed with just three of the possible eight fibers firing, provided they each occupy a different corner of the trapezoid.

While measuring cosmic radiation is not directly linked to the main purpose of FACT, detecting antihydrogen, it can be used to assess and improve the efficiency of the detector. Higher detection efficiency means that a possible antihydrogen signal can be measured more easily. The process of measuring the efficiency is subject of chapters 2 and 3.

### 1.3.4 Analysis Software

Data from different detectors and sensor systems across the experiment are sent to the central AEGIS DAQ system and saved in ROOT-files. The ROOT files are given consecutive number referred to as a run-number. In order to have a common analysis platform and to enable the possibility of more elaborate and combined analyses between different detector systems a data analysis framework has been developed. This program is called gAn (AEGIS Offline Analysis) and written as a library of C++ based ROOT v6 macros. gAn is still under active development with new features being added on frequently. gAn is run via the command-line interface (CLI). The command to run a gAn analysis always follows the same structure: `gAn [name of the analysis] [run-number of the data]` (the square brackets are only used for cleaner visual separation of the inputs and not part of the actual command). The run-number input can be given in one of three forms: a single run, a list of runs separated by commas or a range of runs given by the first and the last run separated by a hyphen.

This section focuses on describing the necessary steps from raw FACT data to the final plots in a conceptual way. An overview of the C++ code for the classes and scripts used for analyzing FACT data can be found in appendix A. All classes mentioned in the following are written in a typewriter type font and linked to appendix A where more detailed

descriptions can be found. Used in conjunction, this section and appendix A may serve as a starting point for getting started with the analysis of FACT data.

The smallest unit of information in a recording of FACT is called a hit (`AEgFACTHit`). A hit is the bundle of the three different pieces of information:

- fiber number: 0-793 (containing the information of the spatial position in  $(z,r)$  of the fiber)
- time of the discriminator threshold crossing (rising edge)
- time over threshold (ToT)

The last two values are read directly from the root file as they are already saved in the correct format by `FACTDriver`. The fiber number, however, cannot be obtained directly because `FACTDriver` can only save the information about which MPPC within which FPGA produced a signal. Using a mapping, this “FPGA, MPPC” combination (as seen in figure 1.7) is translated into a fiber number that is linked to the location of the fiber in  $(z, r)$ . The complete mapping is found in tables B.1 and B.2 in appendix B. The mapping is executed using the `FiberMapper` class located inside the `AEgFACT` class.

The data from the root file is saved as a vector consisting of hits, sorted by rising edge times. As the track and vertex reconstruction should only be done on hits originating from the same charged particle crossing FACT, it is important to group them together by rising edge time. The charged pions generated in the antiproton annihilations have velocities close to the speed of light and cross the 2.8 cm between the two super-layers in about 0.1 ns. With the time resolution of FACT of 5 ns, it is very unlikely that hits from one and the same track end up in different time bins. Therefore, for the usual analyses which are run on FACT data one would normally only group hits originating in the same 5 ns-time-bin together. However, as was found out in late 2018, the rising edge of the trigger signal gets smeared out as it is sent to the FPGAs. Since the distance that the signal has to travel through the cable from the trigger generator to the FPGAs in the order for ten meters, the smearing effect is quite strong. As a result, the FPGAs start acquiring data at different times, with differences of up to 10 ns. Therefore, until this issue is fixed from the hardware side, the default setting is to consider a 5 ns timebin along with two neighboring bins. For the reconstruction of cosmic muons even longer time windows are considered. The reason for this is that the muons cross the entire detector, meaning they need to cover a distance of at least 20 cm (around seven times more than the pions from the center of the trap). As the muons are relativistic particles, they need a little under 1 ns to traverse FACT entirely. Therefore, even in an ideal case where all FPGAs start recording at exactly the same point in time, by only considering a single 5 ns time bin, one risks losing about a fifth of all cosmic tracks. Taking into account the uncertainty of the starting times of the FPGAs, the default time window for cosmic data is three time bins.

The grouping of hits is performed by the `BuildEvents` function in the `AEgFACT` class. For every group of hits an instance of the `AEgFACTEvent` class is created. The `AEgFACTEvent` event class holds a vector of all hits that were grouped together as well as a timestamp that corresponds to the average starting time of its constituent hits. `BuildEvents` returns a vector of all `FACTEvents` sorted by event time.

The reconstruction process for charged pions, with the three steps of clustering, track and vertex reconstruction is carried out by the `AEgVertexReconstructor` class. It takes an `AEgFACTEvent` instance as an input and performs the reconstruction steps as requested during an analysis. A visual overview of the `VertexReconstructor` class is given in figure 1.17.

In the first reconstruction step called clustering (`AEgFACTCluster`), spatially neighboring hits within the same super-layer are grouped together. Figure 1.10 illustrates this process. Since each individual hit inside a cluster has a position  $(z_{fiber}, r_{fiber})$  a combined position for the cluster can be calculated. Currently this is done by computing the av-

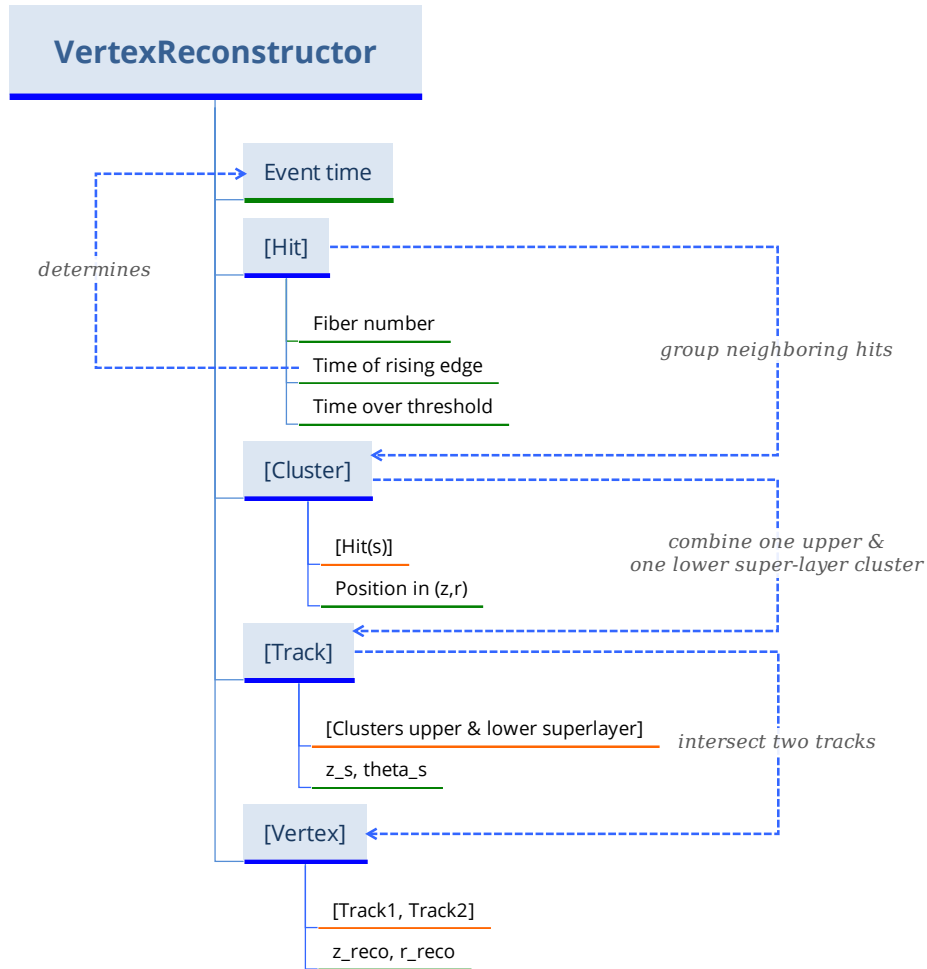


Figure 1.17: Overview of the *VertexReconstructor* class and the reconstruction steps from hits to clusters, tracks and vertices. All green underlined fields are properties obtained by the detector or the reconstruction algorithm and can be plotted for analysis. All orange fields signal a reference to the instances of the previous class that are combined to form the current instance (e.g hits are combined to form clusters, clusters to tracks ...). Square brackets around the class name indicate that the encapsulating class holds a collection (a pair or a vector) of instances of the current class.

In an effort to save computational time, the steps of clustering, track and vertex reconstruction are only carried out if required during the analysis.

erage of all hit positions. For the future, there is the idea to use the relation between time over threshold and the deposited energy in the fiber to calculate a weighted average based on the energy a the fiber received. The clusters are stored in a vector inside the `VertexReconstructor` instance.

The next step of combining clusters to form tracks (`AEgFACTTrack`), looks as follows: If the vector of clusters contains at least one cluster on each super-layer, a track can be reconstructed using the secant method derived in chapter 1.3.1. The track reconstruction is performed by “exploding” the clusters back into the individual hits and performing a linear regression to fit a line through all the hits, yielding  $z_s$  and  $\tan\theta_s$  values of the fitted line. The “exploding” into individual hits is done in order to ensure that clusters with more hits get more weight in the fitting process. As mentioned at the end of chapter 1.3.2 all possible cluster combinations are used to generate tracks. Geometric cuts to reduce multiplicity are only performed before filling the final histograms.

If the vector of tracks contains at least two tracks, that do not share a common cluster, the vertex reconstruction (`AEgFACTVertex`) is carried out as described in chapter 1.3.2.

In case a `FACTEvent` features insufficient hits, clusters, etc... for the next reconstruction step, the corresponding vectors are left empty.

For analyzing cosmic data a class called `AEgCosmicReconstructor` is used. The class takes a `VertexReconstructor` instance as an input as uses the reconstructed clusters. As a first step it is checked if the cluster configuration has the shape of a “cosmic-fingerprint” as shown in figure 1.16b. If this is the case, the fitting of the hyperbolic track as defined in formula 1.11 is performed using the ROOT `TMINUIT` class.

Figure 1.17 provides with a quick overview of the detector’s tracking capabilities. All information is timestamped with 5 ns precision (due to the smearing of the trigger signal the current effective time resolution is closer to 15 ns). Marked in green are the different pieces of information obtained during the course of the reconstruction algorithm, the two most important ones being  $z_s$  and  $z_{reco}$ . Along with those geometric properties, frequencies of hits, clusters etc. can provide valuable information as well. The `VertexReconstructor` structure is the basis of almost all `FACT` analyses. With this central class, that holds all the information recovered by the detector, a number of standard analyses, shown in appendix A, have been developed. Additionally, developing a new analysis from scratch can be done in a short amount of time. By looping over the vector of `FACTEvents` which is built automatically and calling the `VertexReconstructor`, the quantities of interest (the green fields from figure 1.17) can be obtained and filled into histograms. Common histogram types include 1D histograms showing the number hits/clusters/etc... vs. time, reconstructed  $z$  values from tracks and vertices as well as 2D histograms of the same reconstructed quantities vs. time.



Die approbierte gedruckte Originalversion dieser Diplomarbeit ist an der TU Wien Bibliothek verfügbar.  
The approved original version of this thesis is available in print at TU Wien Bibliothek.



## Chapter 2

# Efficiency Measurement Method

Though this be madness, yet  
there is method in't.

— WILLIAM SHAKESPEARE  
*Hamlet*

One of the most important characteristics of any particle detector is its detection efficiency. This chapter concerns itself with the process of determining the FACT detector's efficiency on the single fiber level.

The first part covers deriving an efficiency measurement method without the need of an external reference detector. As particle source the method can make use of either charged pions from antiproton annihilations or cosmic radiation. Initially, the method is deduced in a purely mathematical way. Its software implementation is covered afterwards. As the precision of the efficiency measurement depends on the acquisition time, subsection 2.1.1 covers calculating how much antiproton annihilations or cosmic radiation is needed for a precise measurement.

In order to test the method's capabilities of determining the efficiency values of single fibers, it is tested against Monte Carlo generated data. For this test, both antiproton annihilations as well as cosmic radiation are used.

Finally, as the detector is currently limited to recording 21.5 seconds of data at a time, the software written to automate longer measurements, particularly the acquisition of cosmic radiation, is covered in section 2.4.

This chapter also introduces two features of this thesis related to data analysis and future investigations in particular. Firstly, most plots presented in the current and in the following chapter come with links to the AEGIS-TWiki where additional information is provided. Secondly, for the analyses carried out with gAn, the CLI command used to generate the presented plot is provided at the end of the figure's caption. The name of the gAn analysis which is part of the command, is linked to appendix A where details about the inner workings of the analysis is given. These two features were added to enable a smooth transition from the work presented in this thesis to future analyses.

## 2.1 Derivation of the Method

The overall efficiency of the FACT detector is determined by the efficiencies of its fibers. The fiber efficiency describes how likely a fiber is to produce a signal when hit by a charged particle. It is calculated by comparing how many times a fiber was hit by a charged particle and how many of those times it actually produced a signal. In order to obtain the number of times a fiber has been hit (regardless of whether or not it fired<sup>1</sup>), a reference is needed. This reference can be a second detector with known efficiency, or, in the case of FACT, the detector itself can act as its own reference.

This is achieved by making use of the detector's tracking capabilities. Through reconstructing tracks and checking if the fibers along the trajectory were firing or not "hits" and "misses" for each individual fiber are counted.

This process of repeatedly carrying out a measurement with two possible outcomes (hit or miss) is called a binomial experiment. For a given probability (the fiber efficiency  $E$ ) for success, the number of successes (hits) in  $n$  trials (hits+misses) follows a binomial distribution. The probability density function of this distribution is given in equation 2.1 with  $h$  as the number of hits and  $m$  the number of misses for  $n$  trials.

$$f(h|n, E) = \binom{n}{h} E^h (1 - E)^{n-h} = \binom{n}{h} E^h (1 - E)^m \quad (2.1)$$

Using the Bayesian interpretation of probability (as described in [25, p. 155-165]) information about the fiber efficiency can be obtained. The idea is to start with a prior assumption about the probability distribution  $\pi(E)$  of the sought parameter. Next, the experiment is carried out, in our case track reconstruction and counting of hits and misses. Given the experiment's outcome, a likelihood function  $p(h, m|E)$  is constructed that models the probability of the outcome of the measurement for a given value of  $E$ . This likelihood function is constructed according to the underlying probability distribution. Since the distribution in our case is binomial, the likelihood function looks as follows:

$$p(h, m|E) = \binom{n}{h} E^h (1 - E)^m \quad (2.2)$$

By multiplying the prior distribution with the likelihood function and normalizing the result, the so-called posterior distribution is obtained:

$$p(E|h, m) = \frac{p(h, m|E)\pi(E)}{\int_0^1 p(h, m|E)\pi(E)dE} \quad (2.3)$$

This posterior distribution can be interpreted as the complement to the likelihood function. While the likelihood function contains information about how probable the measurement is, given a value of the parameter, the posterior distribution describes how likely the parameter has a certain value given the outcome of the measurement. The a posteriori distribution can be used to get an estimate of the parameter, construct confidence intervals, test hypotheses, etc...

In order not to introduce any bias in the posterior distribution, a uniform prior distribution ( $\pi(E) = \text{unif}(0, 1)$ ) is chosen. The posterior distribution then has the following form:

$$p(E|h, m) = \frac{\binom{n}{h} E^h (1 - E)^m}{\int_0^1 \binom{n}{h} E^h (1 - E)^m dE} \quad (2.4)$$

<sup>1</sup>In the context of this chapter "fiber" describes the entire detection element composed of a scintillating fiber, a light guide and an MPPC. The term "to fire" is used to describe that the MPPC produces a signal.

By using the definition of the beta distribution  $Be(x; a, b)$ :

$$Be(x; a, b) = \frac{x^{a-1}(1-x)^{b-1}}{\int_0^1 x^{a-1}(1-x)^{b-1} dx} \quad (2.5)$$

the a posteriori distribution can be written as:

$$p(E|h, m) = Be(E; h+1, m+1) \quad (2.6)$$

As an estimator  $\hat{E}$  for the value  $E$ , the mode (i.e. the maximum of  $p(E|h, m)$ ) is used. This value is given by:

$$\hat{E} = \frac{h}{h+m} \quad (2.7)$$

which is consistent with the maximum-likelihood estimator for  $E$ .

Along with the estimated value for  $E$  it is important to assess its uncertainty. In order to do this we can use a confidence interval  $[E_{min}, E_{max}]$ . A confidence interval describes a region in the parameter space where the real parameter is located with high certainty. A standard value for this high certainty is 95%. In general, the confidence interval is constructed by using the quantile function associated with the underlying probability distribution of the random variable. A quantile function  $Q(p)$  computes for a given probability  $p$ , a value  $X$  of the random variable so that the probability of the variable being smaller or equal than  $X$  is equal to  $p$ . For the 95% confidence interval using the quantile function of the beta distribution  $Q_{Be(a,b)}$  we get:

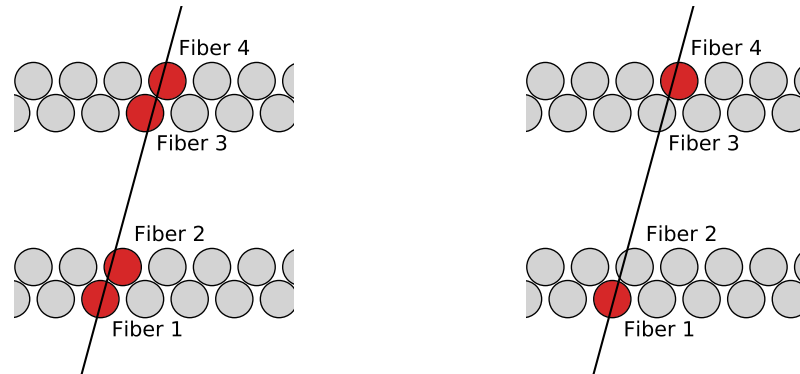
$$\begin{aligned} E_{min} &= Q(0.025)_{Be(h+1, m+1)} \\ E_{max} &= Q(0.975)_{Be(h+1, m+1)} \end{aligned} \quad (2.8)$$

As a measure of the total amount of uncertainty, the length of the 95% confidence interval can be used:

$$\Delta E = E_{max} - E_{min} = Q(0.975)_{Be(h+1, m+1)} - Q(0.025)_{Be(h+1, m+1)} \quad (2.9)$$

For a sufficiently high number of trials ( $n \sim 200$ ) the value of  $\Delta E$  scales with  $\sim n^{-\frac{1}{2}}$ .

Now that the statistical foundation has been covered we can take a look at the process of counting hits and misses illustrated with two examples in figure 2.1.



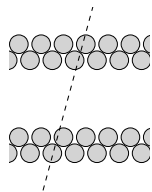
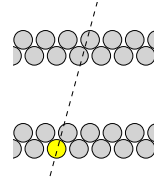
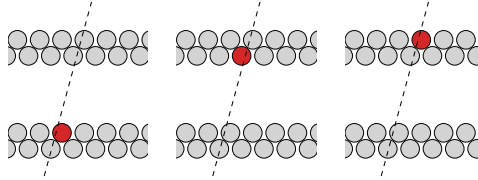
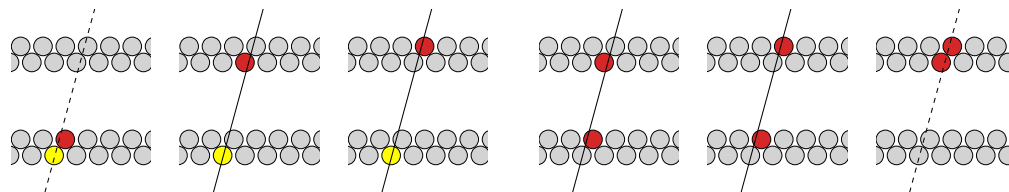
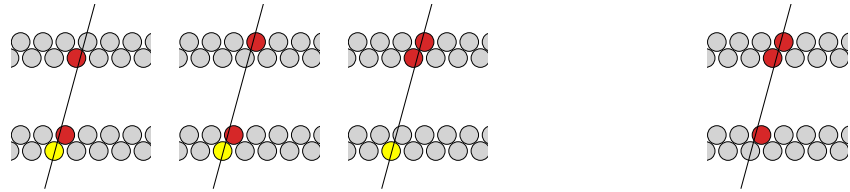
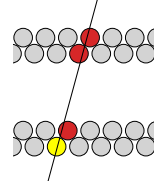
(a) Particle track with all four fibers along the trajectory firing. All four fibers are counted as hits.

(b) Particle track with fiber 2 and 3 missing. Fibers 1 and 4 are counted as hits and fibers 2 and 3 as misses.

Figure 2.1: Two different examples for hit configurations. The nomenclature of fibers 1 to 4 is carried out throughout this section. Red color-coding marks a firing fiber while grey denotes an idle channel.

Looking at figure 2.1 it is obvious that there are many more configurations of hits and misses possible (e.g. fibers 1, 2 and 3 firing with fiber 4 missing, etc...). To be exact, for four fibers with two states each (firing or not firing) we get a total of  $2^4 = 16$  different configurations. In order to keep the uncertainty of the efficiency estimator as small as possible we want to make use of the maximum amount of configurations. As a visual guide to all 16 different configurations, the complete classification is shown in table 2.1.

Table 2.1: Overview of all possible configurations for a track crossing 4 fibers from the point of view of fiber 1 (named according to figure 2.1). The abbreviation “AFF” in the first column stands for “amount of fibers firing” and was used for layouting reasons to keep the table in a single page. The configurations are divided into two columns “Hit” and “Miss” depending on whether or not fiber 1 is firing. For a clearer visual representation, fiber 1 is marked in yellow when firing instead of red. The underlying particle track is drawn as a solid line if the configuration features at least one hit on each super-layer, indicating that track reconstruction possible. If this is not the case the track is drawn as a dashed line.

AFF	Hit	Miss
0		 <p>(a)</p>
1	 <p>(b)</p>	 <p>(c) (d) (e)</p>
2	 <p>(f) (g) (h) (i) (j) (k)</p>	
3	 <p>(l) (m) (n) (o)</p>	
4	 <p>(p)</p>	

Using table 2.1 as a reference, we can estimate the efficiency of fiber 1 based upon the different observable cases (all cases will be referenced by the corresponding lower case letters.)

A successful track reconstruction is necessary to assess which fibers should fire. Therefore, only “trackable” cases (denoted by solid lines in table 2.1) can be used. From the initially 16 different configurations, the reconstruction can be carried out for 6 “Hit” (g, h, l, m, n, p) and for 3 “Miss” configurations (i, j, o).

In order to calculate the probability of those 9 usable cases we assign each fiber an efficiency  $E_i$ . This is necessary because the different cases are not equally probable. In order to minimize notational overhead, we make use of the following shorthand  $E_i \cdot E_j \cdot E_k = E_{ijk}$  (Inspired by the Einstein notation).  $E_i$  denotes the probability to hit. The probability to miss is  $E_{i'} = 1 - E_i$ . This notation also yields following relation:  $E_i + E_{i'} = 1$ . An overview of all 9 usable cases grouped by hit or miss is shown in table 2.2.

Table 2.2: Probabilities for the all “trackable” cases

	Case	Probability
Hits	g	$E_{12'34'}$
	h	$E_{12'3'4}$
	l	$E_{1234'}$
	m	$E_{123'4}$
	n	$E_{12'34}$
	p	$E_{1234}$
Misses	i	$E_{1'234'}$
	j	$E_{1'23'4}$
	o	$E_{1'234}$

In an attempt to minimize the uncertainty we use all hits and misses according to table 2.2 to estimate the efficiency of fiber 1 as presented in formula 2.7:

$$\begin{aligned}
 \hat{E}_1 &= \frac{\text{hits}}{\text{hits} + \text{misses}} = \\
 &= \frac{E_{12'34'} + E_{12'3'4} + E_{1234'} + E_{123'4} + E_{12'34} + E_{1234}}{E_{12'34'} + E_{12'3'4} + E_{1234'} + E_{123'4} + E_{12'34} + E_{1234} + E_{1'234'} + E_{1'23'4} + E_{1'234}} = \\
 &= \frac{E_1(E_2(E_{34'} + E_{3'4} + E_{34})) + E_{2'}(E_{34'} + E_{3'4} + E_{34})}{E_1(E_2(E_{34'} + E_{3'4} + E_{34}) + E_{2'}(E_{34'} + E_{3'4} + E_{34})) + E_{1'}E_2(E_{34'} + E_{3'4} + E_{34})} = \\
 &= \frac{E_1(E_2 + E_{2'})}{E_1(E_2 + E_{2'}) + E_{1'}E_2} = \frac{E_1}{E_1 + E_{1'}E_2}
 \end{aligned} \tag{2.10}$$

As can be seen in equation 2.10 this approach of simply counting all hits and misses leads to an expression for the efficiency for fiber 1 that depends on the efficiency of fiber 2. This poses a problem because for any value  $E_2 \neq 1$  the denominator of equation 2.10 will be smaller than 1 and the efficiency for fiber 1 will be overestimated. In order to understand how the biased overestimation arises we can look back at table 2.2. By adding 6 different hit configurations compared to only 3 misses to the efficiency formula we are tipping the scales strongly in favor of the hits, thereby overestimating the efficiency. This means that the straightforward approach of counting all hits and misses as shown in figures 2.1b and 2.1a does not yield an unbiased estimator of a fiber’s efficiency.

In order to avoid the biased overestimation, we have to understand the criterion that determines whether or not adding a particular hit will tip the scales. The key in keeping the balance is to only add a hit configuration if the corresponding miss configuration is “trackable”. Corresponding means that the only difference between a hit and a miss configuration is the presence of the studied fiber (in this case fiber 1). We are only allowed to add hit-miss pairs to our estimation. Looking at table 2.1, those pairs can be found easily. The idea is to start on any row in the hit column, move to the miss column and go up one row. The corresponding miss configuration is found at the same position within the row as the hit. Using all 16 cases (disregarding “trackability” for a moment) we can build up a complete table of all 8 hit and miss combinations and sort them in usable and non-usable, yielding the following:

Table 2.3: All 8 different hit and miss combinations. A combination is only usable if both the hit and the miss are “trackable”.

	Hit	Miss
usable	l	i
	m	j
	p	o
non-usable	b	a
	f	c
	g	d
	h	e
	n	k

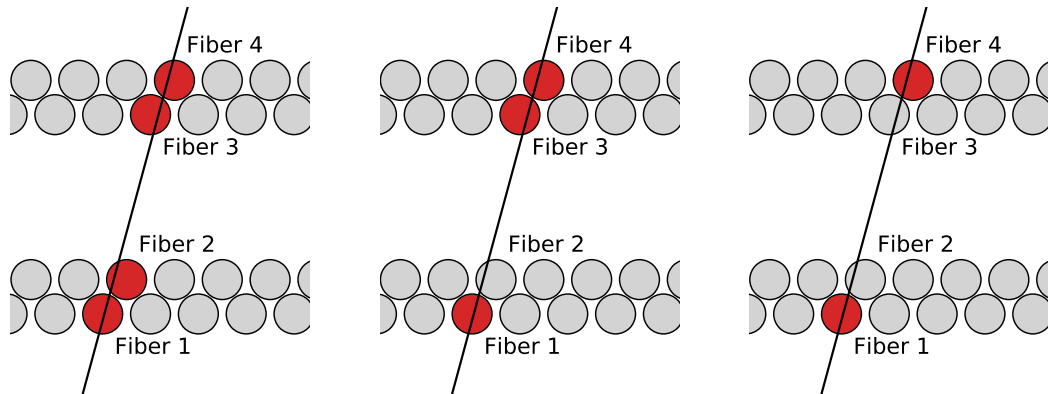
Looking at the non-usable combinations, the initial problem with using all “trackable” hits from table 2.2 can be identified. Configurations g, h and n were added to the efficiency calculation in equation 2.10 and while those three cases are “trackable”, their respective miss counterparts (k, d and e) are not, rendering the whole combination non-usable. This leaves us with three usable pairs (l, i), (m, j), and (p, o). Combining all three pairs yields the following expression:

$$\begin{aligned}
 \hat{E}_1 &= \frac{E_{1234'} + E_{123'4} + E_{1234}}{E_{1234'} + E_{123'4} + E_{1234} + E_{1'234'} + E_{1'23'4} + E_{1234}} = \\
 &= \frac{E_1 E_2 (E_{34'} + E_{3'4} + E_{34})}{E_1 E_2 (E_{34'} + E_{3'4} + E_{34}) + E_{1'} E_2 (E_{34'} + E_{3'4} + E_{34})} = \quad (2.11) \\
 &= \frac{E_1}{E_1 + E_{1'}} = E_1
 \end{aligned}$$

As opposed to equation 2.10, equation 2.11 does produce an unbiased estimator of the efficiency of fiber 1. Additionally, it also makes use of the maximum amount of configurations leading to the smallest uncertainty possible.

Now that an expression of the efficiency of fiber 1 has been found, the next step is to generalize the approach so that the efficiency of any fiber involved in a given track can be assessed. Apart from producing unbiased, minimum uncertainty efficiency estimators for all fibers involved in a track this generalized approach also needs to be able to be implemented software-wise. In order to find a general rule we need to recap what we have learned in deriving the efficiency estimator for fiber 1.

We are only allowed to add hit and miss cases in pairs. In order to find the corresponding miss for a hit configuration, the studied fiber is removed. If the new configuration is still “trackable”, the combination is usable and we are allowed to add the hit. When it comes to adding a miss the rules are less strict. As we saw when going from table 2.2 to table 2.3 we were allowed to keep all three miss cases. This is because in order to identify a fiber as missed we need an already “trackable” combination. This means that the corresponding hit configuration will always be “trackable” as well. Therefore, without checking anything we are allowed to add all missed fibers as missed to the estimator. The generalized approach is illustrated using three example configurations presented in figure 2.2.



(a) All four fibers 4 can be added as hits since removing any fiber will always leave at least one fiber in each super-layer, thereby preserving “trackability”.

(b) According to our rule for missed fibers, fiber 2 can be added as a miss. Fibers 3 and 4 can be added as hits since removing either will preserve “trackability”. Fiber 1, however, must not be added as a hit since removing it leaves just fibers 3 and 4.

(c) Again fibers 2 and 3 can be added as missed. Fibers 1 and 4, on the other hand, must not be counted since if either one is removed, just one hit remains and track reconstruction is no longer possible.

Figure 2.2



With a general rule deduced, the algorithm that was implemented in gAn to carry out the efficiency measurement can be written in pseudocode as shown in algorithm 2.1.

```

Input: trackvector; // vector of reconstructed tracks
Output: fiber efficiency estimator; // amount of hits and misses per fiber

// cycle over all tracks
foreach track of trackvector {
    Identify missing fibers;
    Add all missing fibers to the estimator;
    // cycle over all hits from the current track (track.Hits)
    foreach hit of track.Hits {
        /* check if the remaining configuration which consists of all
           hits from track.Hits except for the currently studied hit can
           still reconstruct a track */
        if remaining_configuration is trackable {
            Add hit to the estimator;
        }
    }
}

```

Algorithm 2.1: Pseudocode outline of the efficiency measurement algorithm that produces unbiased estimators of the efficiency values of single fibers.

While the steps presented in algorithm 2.1 are fairly straightforward to implement, there is one caveat. The process of identifying missing fibers relies on having a tracking algorithm in place that correctly reconstructs particle tracks. Errors in the tracking will identify fibers wrongly and lead to incorrect results in the efficiency estimation<sup>2</sup>.

This concludes the derivation of the efficiency measurement method for FACT. Expressions for the estimator (formula 2.7), its bounds (formula 2.8) and the total amount of uncertainty (formula 2.9) have been derived as well as a way to implement the approach software-wise.

Importantly for the FACT detector, the method is not limited to charged pion tracks from within the detector volume but can be applied to cosmic radiation as well. As covered in subsection 1.3.3, for cosmic radiation a maximum of eight firing fibers is expected and full hyperbolic track reconstruction is possible. Eight fibers translate to a total of  $2^8 = 256$  different configurations. Grouping and categorizing all of them by hand would be a very tedious task and therefore it is highly convenient that the algorithm in 2.1 works for cosmic radiation as well.

More generally speaking, the method can be used to assess the efficiency of individual pixels of any pixel or pixel-like tracking detector without the need of any external reference or a fully characterized particle source.

Due to the fact that this method works self-consistently without external reference it shall be called the “Münchhausen”-efficiency-method<sup>3</sup> (MEM for short).

<sup>2</sup>As there is always uncertainty in track reconstruction there is the possibility to use fuzzy instead of Boolean logic. Rather than singling out specific fibers that should fire along the particle’s path, this approach would make use of a weighted likelihood area across multiple fibers according to the amount of uncertainty.

<sup>3</sup>Named after Baron Munchhausen from the eponymous 1,786 book by Rudolf Erich Raspe. The Baron’s countless adventures include rescuing himself and his horse from a swamp by pulling himself out on his own hair.

### 2.1.1 Required Amount of Particles

Before conducting any efficiency measurement it is important to assess how many charged particles are needed to determine the efficiency of all of the 794 FACT fibers with a given uncertainty. For the context of this thesis, a target uncertainty of 0.1, as defined in formula 2.9, is used. The calculation for the required amount of particles works slightly differently for each of the two sources of particles, charged pions and cosmic muons. Both are addressed in the following, starting with the charged pions.

As the antiprotons that produce the charged pions during annihilations are normally confined in the production trap of the AEGIS-experiment, one of two different procedures is used to annihilate them in large numbers. The first procedure involves lowering the trapping potential of the downstream (positive  $z$  direction in FACT-coordinates) trapping electrode which causes the plasma to spill out of the trap. As the antiprotons escape the trap they eventually reach a micro-channel plate detector. This detector is called the HDMCP (hydrogen detector microchannel plate), located at around 13.6 cm downstream of the center of FACT. Upon impact the antiprotons annihilate, making the HDMCP act as an almost point like charged pion source.

The other possibility is using the rotating wall electric field, that is normally used for compression, in the opposite way. By applying a reverse rotating wall, the antiproton plasma is expanded until the particles hit the trap walls and annihilate. This type of procedure is called radial blow-up<sup>4</sup>.

Regardless of the method used to annihilate the antiprotons, the important figure is how many antiproton annihilations it takes to achieve an efficiency estimate with an accuracy of 0.1. The starting point for this estimate is the average charged pion multiplicity which is around 3 for a  $\bar{p}$ -annihilation. The next step is to quantify the solid angle coverage, i.e. how many of those potential 3 pions are expected to actually hit the FACT detector. While the HDMCP can be approximated as a pion point source, the radial blow-up procedure has the antiprotons annihilating along the  $z$  direction between  $-6$  cm and  $0$  cm. The two source regions are illustrated in figure 2.3.

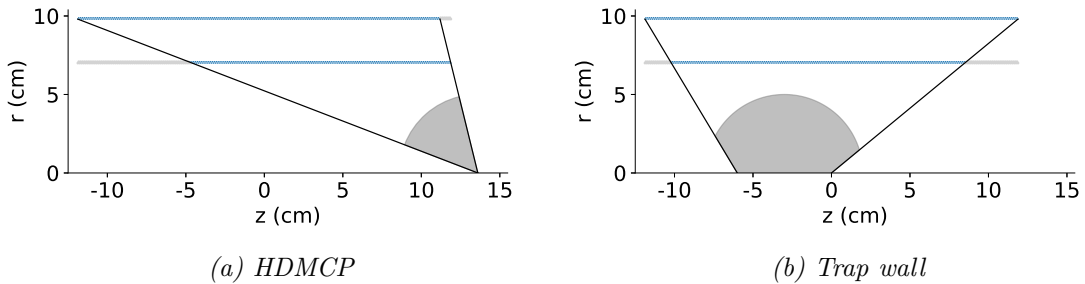


Figure 2.3: Regions in  $z$  for the two different sources of signal. For (a) a planar angle (denoted in grey) of  $\vartheta_{HDMCP} \sim 55.2^\circ$  is calculated, for (b) the average planar angle for the region of  $-6$  cm to  $0$  cm is  $\vartheta_{Trap} \sim 98.7^\circ$ . The fibers which are excluded by geometry are marked in grey. For (a) this grey fraction is about 132 fibers while for (b) it is 84.

Before  $\vartheta_{HDMCP} \sim 55.2^\circ$  and  $\vartheta_{Trap} \sim 98.7^\circ$  can be used in the estimation, the two planar angle values have to be converted to solid angle values. Additionally, they need to be corrected for the opening angle of FACT in the  $\varphi$ -direction (as defined in figure 1.3). The two FACT super-layers have different opening angles of  $22^\circ$  (6.1% relative to  $360^\circ$ ) for the inner and  $40^\circ$  (11.1%) for the outer super-layer. The solid angle values need to be corrected by the bigger amount of 11.1% for two reasons. Firstly, both super-layers are need to be crossed by the charged particle to enable track reconstruction. Secondly,

<sup>4</sup>Details about the settings of the antiproton trap can be found here: <https://aegisgateway.cern.ch:8443/eLog/RunLog/4590>

particle tracks originating closely to the center of FACT, have, in first approximation, a constant  $\varphi$  value. As particle tracks are required to have their (almost) constant  $\varphi$  value in the acceptance region of both layers, the opening angle of the outer super-layer needs to be used for the correction.

Calculating the solid angle values yields 27.2 % for the HDMCP and 48.7 % for the antiproton trap. From the on average around 3 charged pions ( $\pi^\pm$ )<sup>5</sup> per antiproton annihilation we therefore expect about 0.82 for the HDMCP and 1.46 for the trap wall to end up crossing FACT. In order to get an estimate of the number of particle crossings that each fiber experiences on average per antiproton annihilation, the number of charged pion tracks within the detector volume is multiplied by four (number of fibers crossed per track) and divided by the number of available fibers (marked in blue in figure 2.3).

$$\eta_{HDMCP} = 3 \frac{\pi^\pm}{\bar{p}} \cdot 27.2\% \cdot \frac{4 \cdot \text{crossings}}{\pi^\pm} \frac{1}{662 \cdot \text{fibers}} = 4.9 \times 10^{-3} \frac{\text{crossings}}{\bar{p} \cdot \text{fiber}} \quad (2.12)$$

$$\eta_{Trap} = 3 \frac{\pi^\pm}{\bar{p}} \cdot 48.7\% \cdot \frac{4 \cdot \text{crossings}}{\pi^\pm} \frac{1}{710 \cdot \text{fibers}} = 8.2 \times 10^{-3} \frac{\text{crossings}}{\bar{p} \cdot \text{fiber}} \quad (2.13)$$

To put this somewhat abstract definition in perspective, the number of antiproton annihilations required so that each fiber is expected to be crossed at least once can be calculated by taking the inverse of  $\eta_{HDMCP}$  and  $\eta_{Trap}$ . Resulting in around 200 antiprotons for the HDMCP and around 125 for the trap.

For cosmic radiation the  $\eta$ -parameter is defined slightly differently. Since cosmic radiation is hitting the detector at a constant low rate ( $\sim 150 \text{ Hz m}^{-2}$ ) it makes sense from an experimental point of view to define  $\eta$  as the amount of crossings that each fiber sees per second. More precisely, as the efficiency assessment only works if a particle track can be reconstructed, the value  $\eta$  is the rate of crossings each fiber sees, provided cosmic track reconstruction is possible (i.e. at least three corners of the trapezoid shown in figure 1.16 are present). As cosmic particles can in principle hit FACT from every possible direction, a number of muons end up only crossing a total of one or two super layers. In order to correctly assess the expected amount of clusters, and the resulting fraction of cosmic radiation where track reconstruction is possible, a Monte Carlo simulation was carried out. For the simulation the Geant4 software package with a self-developed cosmic muon generator was used. The momentum and angular distributions generated are modeled based on experimental data. A total of  $2.2 \times 10^6$  cosmic muons were generated on a half sphere that encompasses FACT. The half sphere has a radius of 100 cm and is centered around the detector. In order to fully enclose FACT, the half sphere is shifted downwards by 9.8 cm so that lines up with the outer super-layer of FACT. The half sphere covers FACT in the same way a cloche covers a plate of food in fine dining. An illustration of the layout is shown in figure 2.4.

The amount of cosmic muons generated for the simulation corresponds to about 20 h of cosmic radiation in the real world. In those simulated 20 h, a total of around  $5.21 \times 10^5$  cosmic muons left at least one cluster in FACT. This results in a rate of 7.24 Hz across the entire detector. In order to assess the fraction of muons where track reconstruction is possible, the complete distribution of the number of clusters for cosmic muons is shown in table 2.4.

<sup>5</sup>The exact numbers are 3.02 charged pions for an antiproton annihilating on a proton and 3.2 for annihilation on a neutron. The numbers are calculated using the branching ratios from table 1 in [26]

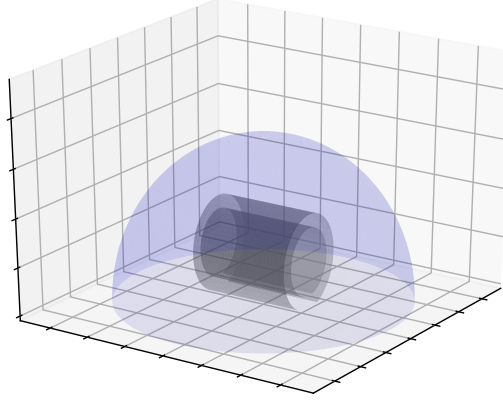


Figure 2.4: Illustration of the half sphere which is used as a source for the cosmic radiation Monte Carlo simulation. For better visualization, the half sphere is only drawn to a third of its actual size.

Table 2.4: Distribution of the number of clusters per simulated cosmic muon. Around 60 % of all muons leave less than three clusters, making tracking only possible for the remaining 40 %.  
Data: 30016

Number of Clusters	Fraction (%)
1	18.83
2	40.65
3	15.40
4	24.42
$\geq 5$	0.70

As table 2.4 shows, track reconstruction is only possible in around 40 % of the cases. This means that the actual rate of cosmic muons across the detector is reduced from 7.24 Hz to  $40\% \cdot 7.24 \text{ Hz} = 2.9 \text{ Hz}$ . Of the 40 % of muons that leave three or more clusters, the three cluster fraction makes up 38 %, while the four cluster fraction is 62 % (as the amount of 5+ cluster cosmic muons makes up less than 1 % of the whole distribution it is disregarded in the context of this thesis).

In order to avoid confusion, the Monte Carlo simulation was carried out with 100 % fiber efficiency, therefore the fact that the distribution contains numbers of clusters smaller than the expected amount of four, is purely a result of the detector's geometry. Additionally, using the MC simulation, the average number of fibers affected by a reconstructable cosmic muon (three or more clusters) was determined to be around 7.0 fibers.

With all numbers derived, the  $\eta$  value for cosmic radiation can be calculated as the product of the cosmic rate that the detector sees as a whole (7.24 Hz), the reconstructable fraction (40 %) and the average amount of fibers affected (7.0) divided by the total amount of FACT fibers (794):

$$\eta_{\text{Cosmics}} = 7.24 \text{ Hz} \cdot 40\% \cdot \frac{7.0}{794} = 25.5 \times 10^{-3} \frac{\text{crossings}}{\text{s} \cdot \text{fiber}} \quad (2.14)$$

To put this figure in perspective as well,  $(\eta_{\text{Cosmics}})^{-1}$  is the expected time for each fiber to be crossed once by a cosmic muon, which is around 39 s. The  $(\eta_{\text{Cosmics}})$  value is to be taken as an average, as it fails to take into account the non-uniform distribution of cosmic muons frequency across the FACT detector.

The next step is to consider fiber efficiencies of  $< 1$  and to calculate how the average fiber level efficiency affects the detector capabilities to reconstruct pions and cosmic muons. As a particle usually crosses a total of two fibers per super-layer and at least one of the fibers is required to fire, the average efficiency of a super-layer ( $\overline{E}_{sl}$ ) can be defined as follows:

$$\overline{E}_{sl} = 1 - (1 - \overline{E}_f)^2 \quad (2.15)$$

Since both super-layers are required to fire in order to reconstruct a pion track, the average tracking efficiency for pions ( $\overline{E}_{Pions}$ ) as a function of the average super-layer efficiency can be calculated easily:

$$\overline{E}_{Pions} = \overline{E}_{sl}^2 \quad (2.16)$$

For cosmic muons, the formula is slightly more complicated. As seen in table 2.4, of all muons where track reconstruction is possible, around 62% feature four clusters, or four super-layer crossings. From those four crossings, at least three are required for reconstruction. The remaining 38% are three cluster cases, meaning all three super-layers that were crossed by the muon are required to fire in order to enable reconstruction. In an attempt to realistically assess the average tracking efficiency for cosmic muons ( $\overline{E}_{Cosmics}$ ), a weighted average of the two cases is used:

$$\overline{E}_{Cosmics} = 0.62 \cdot \left( \binom{4}{3} \overline{E}_{sl}^3 (1 - \overline{E}_{sl}) + \overline{E}_{sl}^4 \right) + 0.38 \cdot (\overline{E}_{sl}^3) \quad (2.17)$$

Apart from calculating the “trackable” fractions, it is also important to calculate the “usable” fraction. The “usable” fraction is comprised of all hit and miss configuration, that are allowed to be considered for the unbiased efficiency estimation. This “usable” fraction is essential in calculating the amount of signal needed for the efficiency assessment. For this thesis, the “usable” fraction was not calculated analytically, but rather numerically. This was done by iterating over all possible configurations for pions and cosmic muons, calculating the probabilities and checking for “usability” as defined at the end of section 2.1. As an example, the complete classification for pion and cosmic muon tracks at  $\overline{E}_f = 0.5$  is presented in table 2.5.

Table 2.5: Classification of particle tracks for  $\overline{E}_f = 0.5$ . All values are in percent, relative to the same 100% comprised of untrackable+trackable.

	Pions	Cosmic Muons
Untrackable	43.75	38.20
Trackable	56.25	61.80
Usable	37.50	49.92
Hits	18.75	24.96
Misses	18.75	24.96

The complete graph of the usable fraction as a function of the average fiber efficiency  $usable(\overline{E}_f)$  is shown as the dashed lines in figure 2.5. Additionally, the “trackable” fraction is shown as the solid lines in figure 2.5 which can be used to convert the average single fiber efficiency to the track reconstruction efficiency and vice versa.

As a (literal) side note, figure 2.5 features a grey link to the *AEgIS-TWiki* next to the plot. As mentioned in the introduction to this chapter, links like this can be found in combination with most plots in the following. The corresponding *TWiki* pages feature information and attachments such as raw data, Python analysis scripts or .csv files of the analysis results.

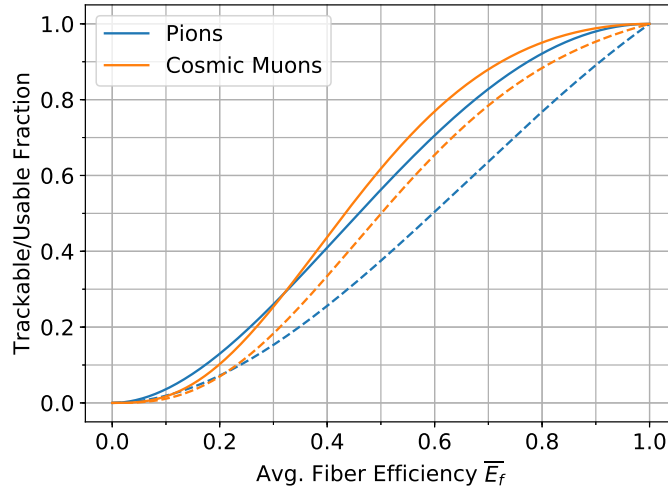


Figure 2.5: Plot of the “trackable” (represented by solid lines) and “usable” (represented by dashed lines) fractions as a function of the average fiber efficiency. The blue solid line is defined in equation 2.16 and the orange solid line in equation 2.17. The dashed lines were calculated numerically.

Utilizing the usable fraction, the required amount of signal (number antiproton annihilations  $n_{\bar{p}}$  or cosmic radiation acquisition time  $t_{Cosmics}$ ) for an efficiency measurement with a given total uncertainty can be calculated. As this figure depends on the average fiber efficiency, the expected number of usable hits  $\hat{h}_{\bar{p}}$  and misses  $\hat{m}_{\bar{p}}$  per antiproton annihilation is given as:

$$\begin{aligned}\hat{h}_{\bar{p}}(n_{\bar{p}}, \bar{E}_f) &= \eta_{HDMCP/Trap} \cdot usable_{e_{\bar{p}}}(\bar{E}_f) \cdot n_{\bar{p}} \cdot \bar{E}_f \\ \hat{m}_{\bar{p}}(n_{\bar{p}}, \bar{E}_f) &= \eta_{HDMCP/Trap} \cdot usable_{e_{\bar{p}}}(\bar{E}_f) \cdot n_{\bar{p}} \cdot (1 - \bar{E}_f)\end{aligned}\quad (2.18)$$

For cosmic muons, the calculation works in the same way, but instead of the number of antiprotons, the acquisition time is used together with the usable fraction of cosmic muons:

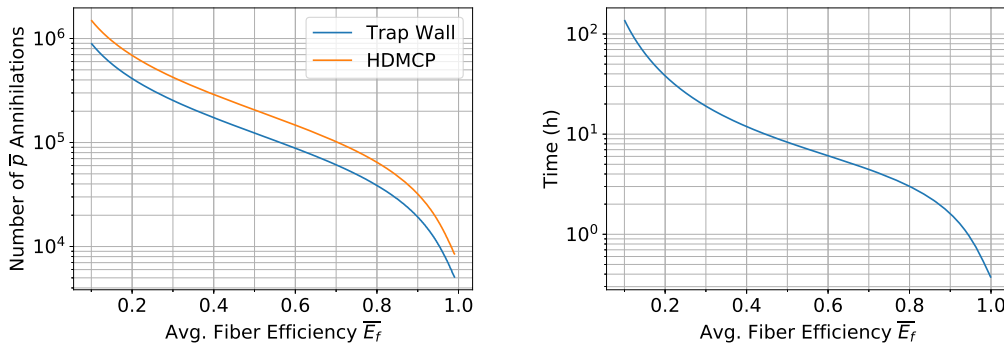
$$\begin{aligned}\hat{h}_{Cosmics}(t_{Cosmics}, \bar{E}_f) &= \eta_{Cosmics} \cdot usable_{Cosmics}(\bar{E}_f) \cdot t_{Cosmics} \cdot \bar{E}_f \\ \hat{m}_{Cosmics}(t_{Cosmics}, \bar{E}_f) &= \eta_{Cosmics} \cdot usable_{Cosmics}(\bar{E}_f) \cdot t_{Cosmics} \cdot (1 - \bar{E}_f)\end{aligned}\quad (2.19)$$

For the final step, the expected amount of hits and misses is used in the definition of the total uncertainty from formula 2.9:

$$\Delta E = 0.1 = Q(0.975)_{Be(\hat{h}+1, \hat{m}+1)} - Q(0.025)_{Be(\hat{h}+1, \hat{m}+1)}\quad (2.20)$$

The values  $\hat{h}$  and  $\hat{m}$  depend on the fiber efficiency as well as the number of antiproton annihilations or the acquisition time for cosmic radiation. In order to get the required amount of antiproton annihilations or cosmic radiation acquisition time for a given average fiber efficiency and to reach a precision of 0.1, equation 2.20 needs to be solved numerically. The result for antiprotons is shown in figure 2.6a and for cosmic muons in 2.6b.

To put the numbers from figure 2.6a in perspective, per shot of antiprotons from the AD, around  $3 \times 10^5$  antiprotons are available inside the final production trap of the AEGIS-experiment. This means that for fiber efficiency values  $> 0.2$  the efficiency estimation can be done within a few shots from the AD.



(a) Number of  $\bar{p}$  annihilations for both (b) Required acquisition time for cosmic re-charged pion sources: HDMCP and trap wall.

Figure 2.6: Required amount of  $\bar{p}$  annihilations shown in (a) and cosmic radiation acquisition time shown in (b) for a target total uncertainty of  $\Delta E = 0.1$ .

Similarly, for cosmic radiation, as shown in figure 2.6b, excluding efficiency values  $< 0.2$ , the acquisition of a sufficient amount of cosmic radiation should not take longer than 40 h. This means that both particle sources can be used to assess the efficiency of the FACT detector in an independent way.

The next step towards an actual measurement is to test the Münchhausen-efficiency-method (MEM) against Monte Carlo simulated data in order to check its results.

## 2.2 Antiproton Monte Carlo

Before the efficiency of the FACT detector can be measured experimentally, the MEM needs to be tested with Monte Carlo (MC) generated data in order to verify if it actually produces unbiased estimators.

For the test, a total of  $2.5 \times 10^5$  antiproton annihilations were simulated for two different scenarios, annihilation on the trap wall inside of FACT and on the HDMCP. The antiproton annihilations were simulated using the Geant4 software package with the the FTFP\_BERT\_TRV library. The simulation was carried out twice. For the first run, the 794 FACT fibers were assigned random efficiency values sampled from a normal distribution  $\mathcal{N}(\mu, \sigma^2)$  with  $\mu = 0.5$  and  $\sigma = 0.15$ . The mean value of 0.5, resulting in a symmetric fiber efficiency distribution, was chosen so that any asymmetries in the reconstructed efficiency values can be attributed to the MEM. The standard deviation was chosen to be as large as possible without a too high probability of efficiency values smaller than zero or bigger than one.

The second run featured perfect fiber efficiencies in order to be used as a reference. An overview of the  $z_s$  distributions (as introduced in subsection 1.3.1) is shown in figure 2.7.

*As a side note, the caption for figure 2.7 features the gAn CLI command that was used to generate the plots. The name of the analysis “FACT\_rec\_min” is linked to appendix A for more information. In order to get same behaviour from this and other analyses in the following, the gAn version from the git branch “philip\_thesis” needs to be used. Details about the installation of gAn and the location of the branch can be found in appendix A as well. Additionally, the raw data specified by their run-numbers are also listed.*

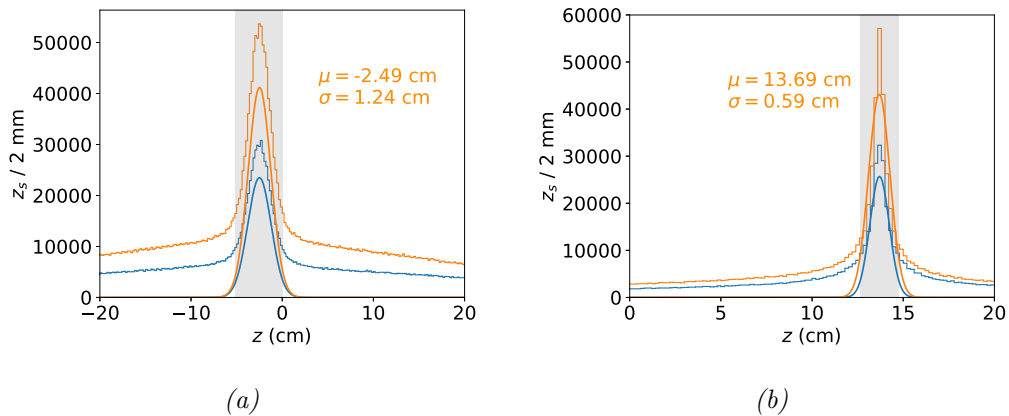


*Figure 2.7: Histograms of the reconstructed  $z_s$ -values for MC antiproton annihilations on the trap wall (a) and on the HDMCP (b). The blue histograms represent the simulated measurements with random fiber efficiencies sampled from  $\mathcal{N}(0.5, 0.15^2)$ . The orange histograms represent a reference measurement with perfect fiber efficiency. All four histograms were fitted with a sum of two Gaussian distributions for signal and background. The signal part of the fitted functions are plotted in the corresponding colors.*

*The mean ( $\mu$ ) and standard deviation ( $\sigma$ ) of the gaussian fits for the perfect efficiency histograms are shown.  $\mu$  and  $\sigma$  are used to define the signal regions as  $\mu \pm 2\sigma$  shown as the grey areas. In order to be used for the efficiency assessment a track's  $z_s$  value needs to fall within this region.*

*Data for (a): full efficiency: 21026,  $\mathcal{N}(0.5, 0.15^2)$ -efficiency: 11026*

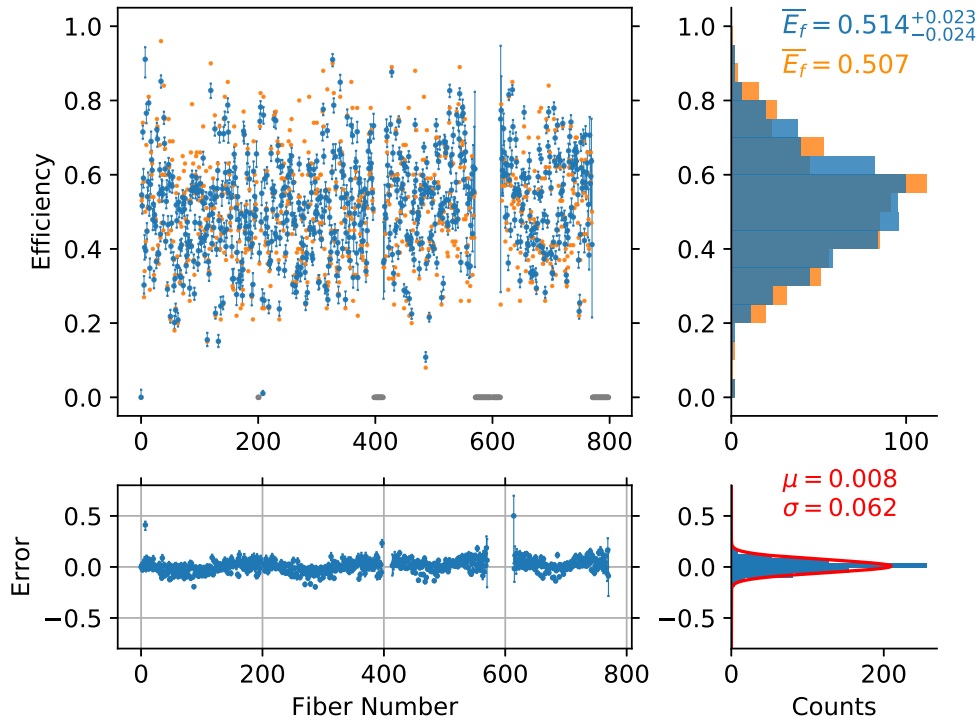
*Data for (b): full efficiency: 21027,  $\mathcal{N}(0.5, 0.15^2)$ -efficiency: 11027*

*gAn FACT\_rec\_min [runnumber]*

<https://twiki.cern.ch/twiki/bin/view/LEGIS/FACTPbarmc>



In order to test the performance of the MEM-algorithm, it was provided the Monte Carlo generated trap wall annihilation data with the random fiber efficiencies. An overview of the results is shown in figure 2.8.



<https://twiki.cern.ch/twiki/bin/view/AEGIS/FACTPbArMC>

Figure 2.8: Overview of the MEM's performance for Monte Carlo simulated antiproton trap wall annihilations.

Top left: The real fiber efficiency values are shown as the orange points and the reconstructed values with error bars in blue. The grey markers represent the fibers that are excluded by the geometric limitations (as seen in figure 2.3b).

Top right: Histograms of the real and the reconstructed values along with the average efficiency values in orange and blue. The two numbers next to the average reconstructed efficiency are the average limits of the 95% confidence interval of the beta function that models the likelihood of the efficiency value.

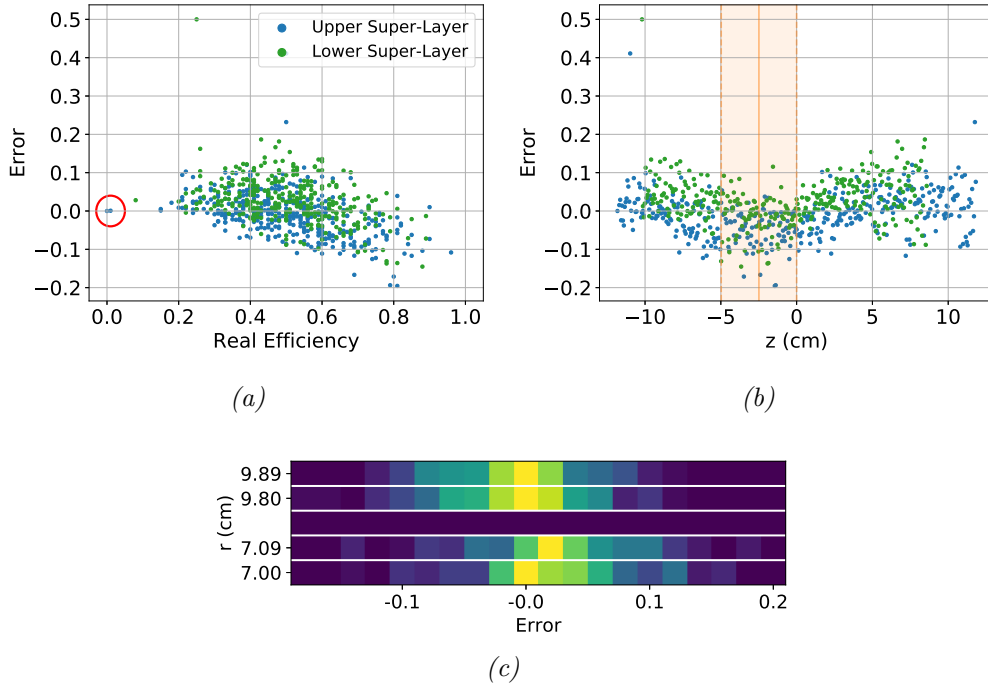
Bottom left: Difference between the blue and the orange values from the top left.

Bottom right: Histogram of the differences including a Gaussian fit and its fit parameters. The value  $\mu$  is called mean signed deviation and represents the bias of the measurement.

*gAn FACT\_Trap\_Eff 11026*

Figure 2.8 shows that for antiprotons annihilating on the trap walls, the MEM is successful in producing an estimator of the average fiber efficiency with a bias ( $\mu = 0.008$ ) smaller than the limits of the statistical uncertainty ( $\sigma = \pm 0.062$ ).

From the bottom left plot in figure 2.8, it can be inferred that the error is correlated to the fiber number. In order to study this effect more closely, correlations between the error and three different fiber properties were investigated. The properties in question are the real efficiency value and the position in  $z$  and in  $r$ . The results are shown in figure 2.9.



<https://twiki.cern.ch/twiki/bin/view/AEGIS/FACTPbarmC>

Figure 2.9: Correlations between the error in the efficiency assessment of single fibers and different fiber properties based on Monte Carlo simulated trap wall annihilations. For figures (a) and (b) the two super-layers are plotted in different colors.

The plots show:

(a) Scatterplot of error vs. real fiber efficiency

(b) Scatterplot of error vs. fiber position in  $z$ . The signal region as defined in figure 2.7a is indicated in orange.

(c) Error distribution matrix for each sub-layer to investigate radial correlation (the separation in the middle of the plot was added to visualize the gap between the two super-layers)

Data: 11026

From figure 2.9a two points can be inferred. Firstly, dead fibers are identified correctly, as indicated by the red circle. Secondly, the more efficient a fiber is, the more its efficiency tends to be underestimated by the efficiency assessment and vice versa. In addition, when comparing the two super-layers to each other, the lower super-layer exhibits higher error values than the upper. This tendency can also be seen in figure 2.9c.

Figure 2.9b shows a second characteristic of the efficiency assessment using central trap wall annihilations. The closer a fiber is to the origin of the signal, indicated as the orange region, the more its efficiency tends to be underestimated.

The causes for the correlations in the errors of single fibers are currently not known. As further investigations into this topic would go beyond the scope of this thesis, more in-depth analyses were not carried out. Figure 2.9, however, may serve as a starting point for future studies.

In the same way as for the trap walls, the simulated HDMCP antiproton annihilation data were fed into the MEM-algorithm as well. An overview of the results is given in figure 2.10.

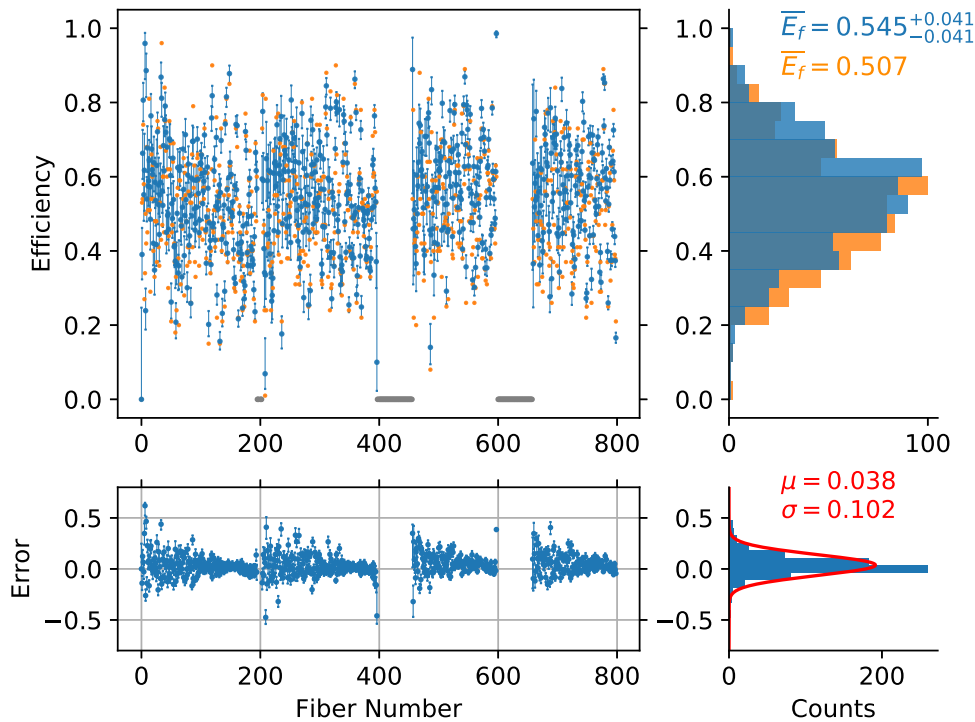
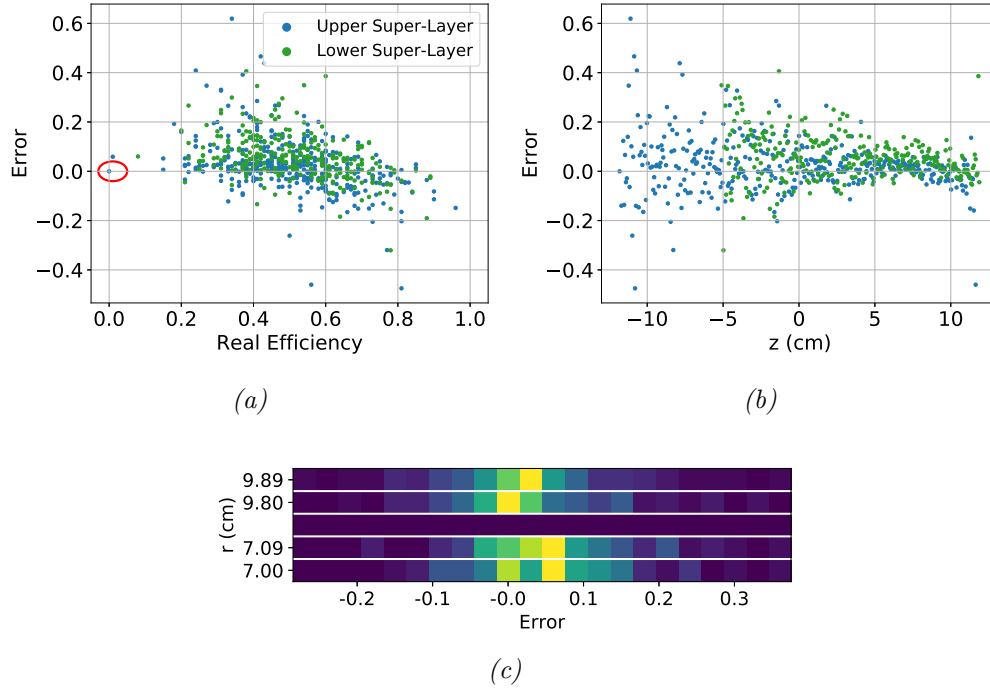


Figure 2.10: Overview of the MEM's performance for Monte Carlo simulated antiproton HDMCP annihilations  
(All plots and values are arranged in the same way as in figure 2.8)  
*gAn FACT\_HDMCP\_Eff 11027*

Compared to the trap wall results, figure 2.10 shows that for pions from the HDMCP the efficiency estimation has a positive bias ( $\mu \sim 0.038$ ). The reason for this is thought to be the shallower angle of the pion tracks from the HDMCP compared to the trap wall. Due to this angle, more than two fibers per super-layer can be hit and identifying the missing fibers becomes more difficult. This also results in a higher  $\sigma$  value in the distribution of the errors compared to the trap wall results.

Nonetheless, the overestimation is not dramatic, so pions annihilating on the HDMCP can still be used to get an idea of the average fiber efficiency of FACT.

In the same way as for the trap wall annihilations, correlations in the errors in the HDMCP based efficiency assessment were also investigated. The results are shown in figure 2.11.



<https://twiki.cern.ch/twiki/bin/view/AEGIS/FACTPbarmc>

Figure 2.11: Correlations between the error in the efficiency assessment of single fibers and different fiber properties based on Monte Carlo simulated HDMCP annihilations.

(All plots are arranged in the same way as in figure 2.9)

Data: 11027

In general, figures 2.11a and 2.11c exhibit similar characteristics as their “trap wall” counterparts.

Conversely, figure 2.11b shows a different pattern than its “trap wall” counterpart, due to the location of the HDMCP as the particle source at  $z = 13.6$  cm. As stated above, the hypothesized reason for the large errors in the upstream part of the FACT detector is that the small angle of the charged pions makes identifying the correct missed fibers a complicated task. Not only are more than two fibers per super-layer crossed, missing fibers also have a bigger impact on the reconstructed track.

As the current efficiency analysis uses an algorithm that cannot identify more than one missing fiber per sub-layer, developing a more sophisticated fiber identification algorithm might be of interest for future, in order to achieve more accurate efficiency measurements.

In summary, antiproton annihilations on both the trap wall and the HDMCP can be used to assess the average fiber efficiency and identify dead fibers.

In order to get highly accurate measurements on the single fiber level, however, more detailed investigations into the causes for the error correlations and developments in the fiber identification algorithm are needed. For any new approach, figures 2.9 and 2.11 may serve as a starting point and benchmark. The reason for this is that every new method needs to be tested for possible correlations as well.

## 2.3 Cosmic Radiation Monte Carlo

In the same way as for antiproton annihilations, the MEM is tested with Monte Carlo simulated cosmic radiation<sup>6</sup> as well. As detailed in subsection 2.1.1, for the simulation a total of  $2.2 \times 10^6$  cosmic muons were generated on a half sphere around FACT. The simulation was carried out twice, with random normally distributed efficiencies ( $\mathcal{N}(\mu = 0.5, \sigma = 0.15)$ ) and with perfect fiber efficiencies for comparison.

In the first step of the analysis of cosmic data, “cosmic-fingerprints” (as described in section 1.3.3) are identified.

Before the track reconstruction is carried out, the number of cosmic-fingerprints can be used to define the “counting”-efficiency. This counting-efficiency quantifies how many cosmic-fingerprints were found relative to the expected amount for 100 % efficient fibers. For the perfect efficiency Monte Carlo data, a total of 206,635 cosmic-fingerprints were found, in comparison to the 127,117 for the 50 % average efficiency simulation. This results in a counting-efficiency of  $127,117/206,635 = 61.5\%$ . This figure can be used to cross-check the model derived in formula 2.17.

As mentioned before, the fiber efficiency values for the MC simulation were randomly sampled from a normal distribution with a mean value of 0.5. The random sample that was used had sample mean of  $\overline{E_f} = 0.51$ . Therefore 0.51 is used in the following calculation.

$$E_{Cosmics}(\overline{E_f} = 0.51) = 0.635 \quad (2.21)$$

This shows the model from equation 2.17 predicts the “counting efficiency” with a relatively small offset of 0.02.

As a side note for possible future investigations, one way to address this discrepancy could be by performing more extensive Monte Carlo studies. By simulating a range of different average fiber efficiencies, a conversion table can be built to replace the analytic model presented in equation 2.17.

In the next step of the track reconstruction process, the  $r$  and  $z$  values of the fibers from the cosmic-fingerprint are used as input values for the hyperbolic fitting procedure. The fitting is carried out using the MIGRAD and MINOS functions from the ROOT class TMINUIT. Next, the resulting curves are filtered using a three level filter. This results in a grouping of the reconstructed curves into four categories. The first category is related to the return value of the ROOT minimization functions, MIGRAD and MINOS. If these functions return anything other than 0, it indicates that something in the fitting procedure has failed<sup>7</sup> and the muon track is classified as “fitting failed”. The remaining trajectories are considered to be successfully reconstructed and are filtered based on their geometric properties. Examples for all three categories are presented in figure 2.12.

<sup>6</sup>Again using the Geant4 software package with the self-developed cosmic muon generator.

<sup>7</sup>For details see the ROOT documentation of the TMinuit Class: <https://root.cern.ch/doc/v614/classTMinuit.html>

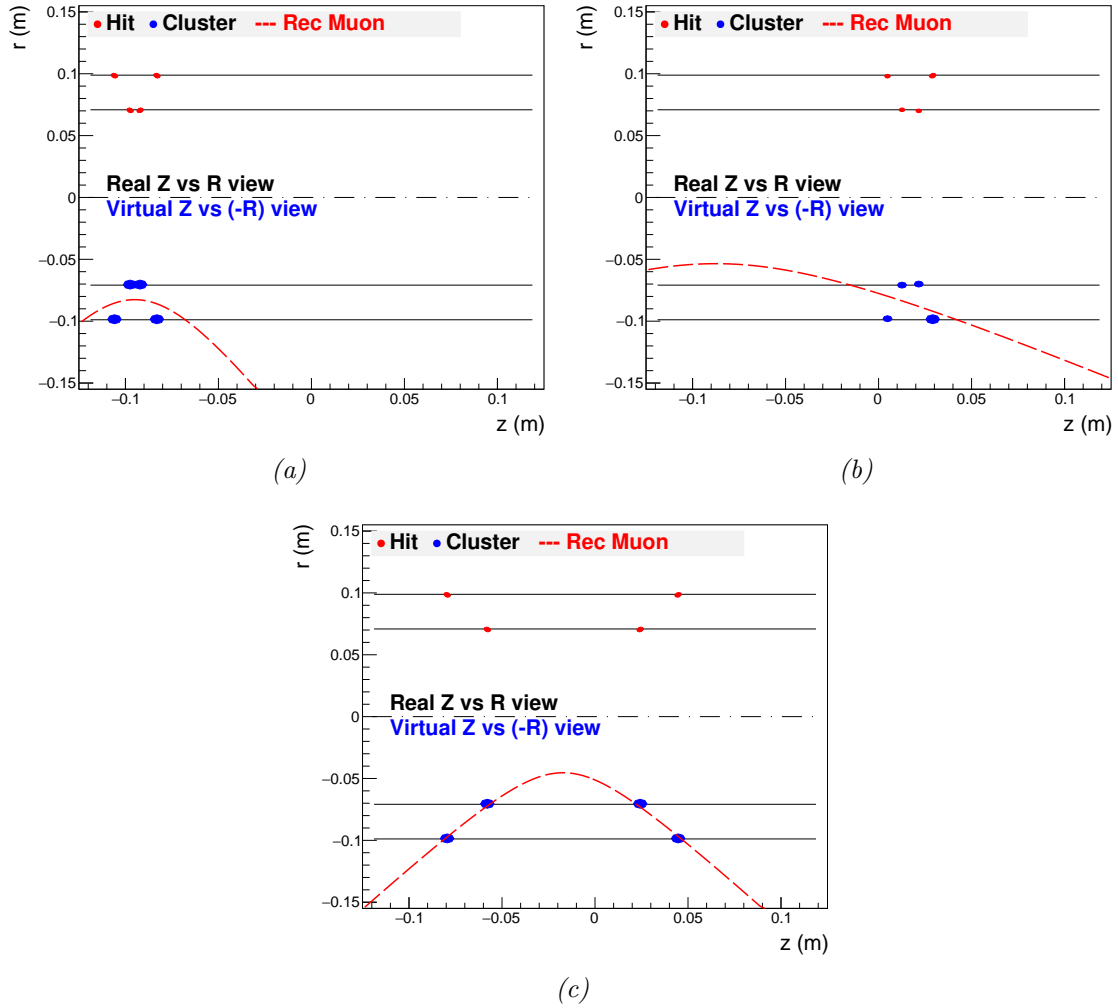


Figure 2.12: Examples for the three different categories of successfully reconstructed cosmic muon trajectories taken from the “Cosmics Viewer” of *gAn*. The horizontal black lines represent the layers of FACT. The bottom half of the plots ( $r < 0$ ) is a mirror image of the upper part where the hits (in red) have been grouped into clusters (in blue). In order to avoid confusion, the reconstructed hyperbola is only drawn once.

(a) Successful fit, but the  $r_{min}$  or  $z_0$  value is not within the detector volume ( $r_{min} \leq 7$  cm and  $-11.88$  cm  $\leq z_0 \leq 11.88$  cm); classified as a “geometry-cut”

(b) Successful fit,  $r_{min}$  and  $z_0$  value are within the detector volume but all firing fibers are missed by the reconstructed trajectory; classified as a “complete miss”

(c) Successful fit; none of the above filters apply, therefore it is classified as a “good cosmic”

*gAn* FACT\_cosmics\_rec 30016 with the *IsVis* option activated

The filtering of the data into the four categories to get the “good cosmics” is carried out in the order in which they were introduced. This means that firstly any trajectories where the fitting procedure failed are removed. In the next step, it is checked if the reconstructed parameters  $r_{min}$  and  $z_0$  fall within the detector’s volume (figure 2.12a). Finally, the fibers which should have fired according to the reconstructed trajectory are compared to the ones that actually did fire. In order to account for some of the uncertainty in the track reconstruction, the “fibers which should fire” are identified using the following strategy. In a first step, the reconstructed hyperbola is intersected with each of the four FACT sub-layers. For each one of the eight resulting intersections points, the five closest FACT fibers are identified. If none those predicted fibers is found in the list of fibers that actually

fired, the trajectory is classified as a “complete miss” (figure 2.12b).

A cosmic muon that passes all those filters is classified a “good cosmic” (figure 2.12c). An overview of the fitting algorithm’s performance for both the full efficiency and the 50 % average efficiency Monte Carlo simulated data is given in table 2.6.

Table 2.6: Fitting algorithm performance based on the distributions of the four different categories of reconstructed tracks. The “Total Amount” figure corresponds to the total amount of cosmic-fingerprints identified during the analysis.

Category	$\overline{E}_f = 1$		$\overline{E}_f = 0.5$	
	Amount	Fraction (%)	Amount	Fraction (%)
Fitting Failed	7,963	3.85	6,509	5.12
Geometry Cut	78,590	38.03	42,587	33.50
Complete Miss	13,760	6.66	11,906	9.37
Good Cosmics	106,322	51.46	66,115	52.01
Total Amount	206,635	100.00	127,117	100.00

What can be seen from table 2.6 is that the performance of the fitting algorithm is relatively unaffected by the average fiber efficiency. Nonetheless, a success rate of around 50 % means that there is room for future improvements in the track reconstruction algorithm. As a next step, the distributions of the reconstructed parameters from the cosmic hyperbolae, namely  $z_0$ ,  $r_{min}$  and  $\theta$ , for the filtered “good cosmics” are shown in figure 2.13.

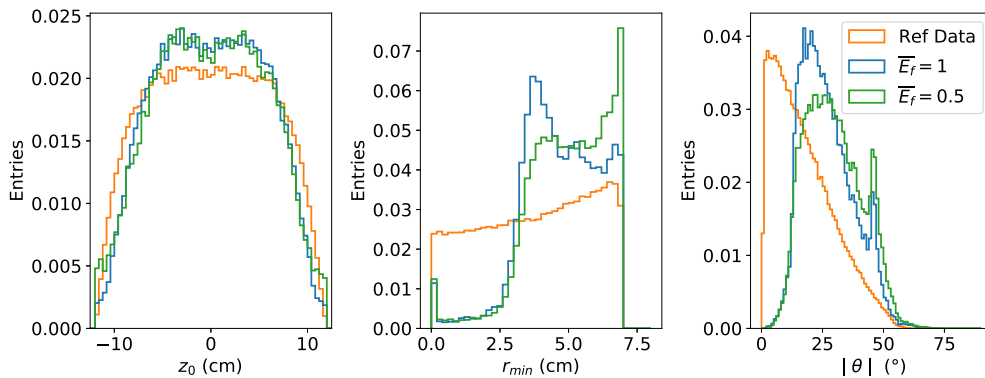


Figure 2.13: Distributions of the three reconstructed parameters for cosmic radiation. As a reference the true generated values of the cosmic muons that leave a “cosmic-fingerprint” are plotted in orange.

All distributions are normalized to the sum of their bins to allow for easier qualitative comparison.

Data: full efficiency: 30016,  $\mathcal{N}(0.5, 0.15^2)$ -efficiency: 30006

gAn FACT\_cosmics\_Eff 30016 and 30006 respectively

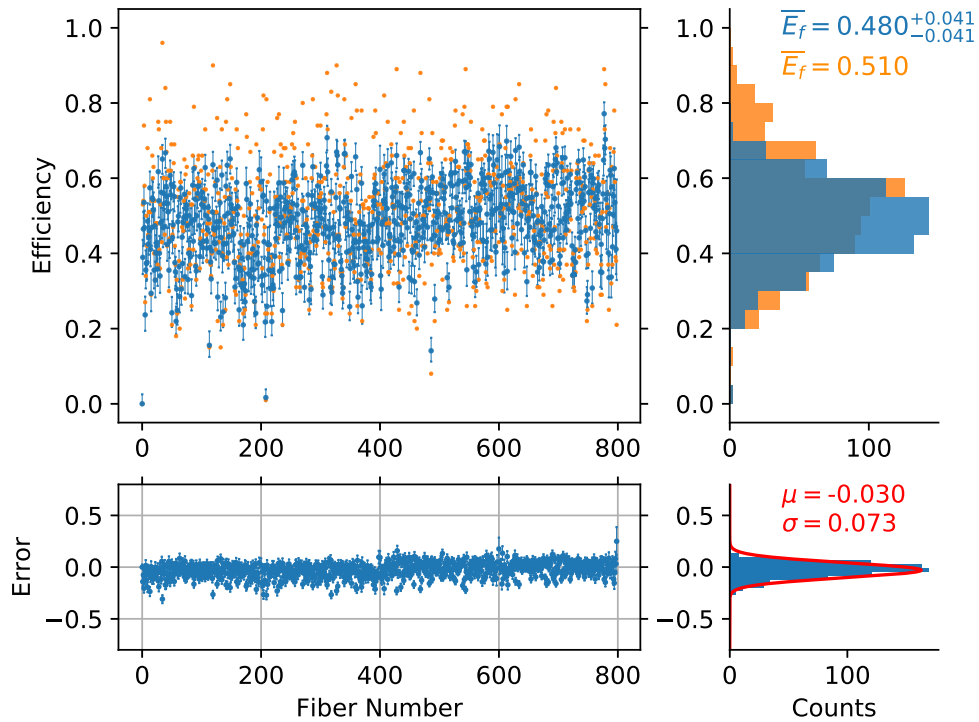
gAn FACT\_cosmics\_read\_MC [placeholder data] for the reference histograms

As figure 2.13 shows, the reconstruction algorithm is successful at  $z$ -reconstruction, whereas for  $r$  and  $\theta$  the reconstructed values differ from the reference. Especially for  $r$ , values below 3 cm are almost non-existent with a small spike around 0 cm, while values around 7 cm seem to be favored. For  $\theta$  the reference curve peaks at around  $3^\circ$  while the reconstructed curves appear shifted to around  $20^\circ$ . As far as correctly identifying the efficiencies of single fibers goes, this is bad news as all three distributions should be close to the reference

https://twiki.cern.ch/twiki/bin/view/AEGIS/FACTCosmicMC

curve in orange. For future investigations especially towards true fiber level efficiency measurements, improving the fitting algorithm and possibly making use of machine learning techniques can be suggested.

Despite the discrepancies in the reconstructed parameters, the MEM was tested for the random efficiency Monte Carlo data with the results shown in figure 2.14.



<https://twiki.cern.ch/twiki/bin/view/AEGIS/FACTCosmicSMC>

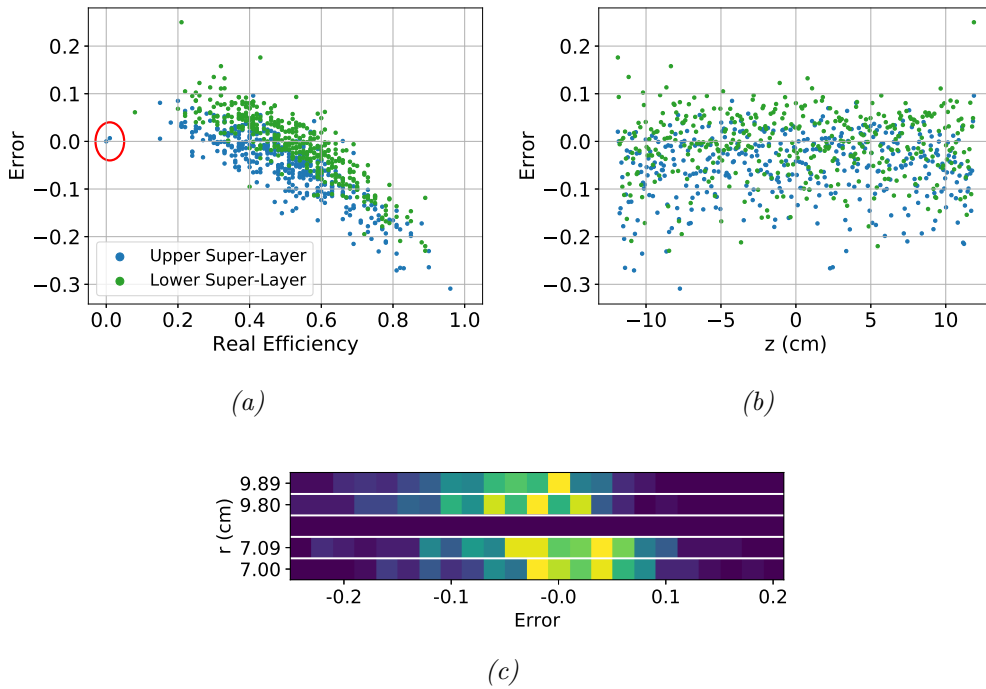
Figure 2.14: Overview of the MEM's performance for Monte Carlo simulated cosmic radiation.

*gAn FACT\_cosmics\_Eff 30006*

A few points can be read from figure 2.14. Firstly, the average fiber efficiency is slightly negatively biased, but all in all the effect is not threatening for a measurement of the average efficiency. Secondly, there is a “compression” effect that can be seen in the top right plot. Compared to the orange reference, the blue histogram appears compressed. Thirdly, as seen in the bottom left plot, the errors seem to be uncorrelated to fiber number and position within the detector. Intuitively, this is what one would expect as the cosmic muons do not have a single point of origin but rather hit the detector from all directions. Therefore they should not favour any particular region of FACT.



In order to further investigate any correlations in the errors that might be washed out by just considering the fiber number, the same correlation analysis as for the antiproton Monte Carlo measurement was carried out. The results are presented in figure 2.15.



<https://twiki.cern.ch/twiki/bin/view/ARGIS/FACTCosmicSMC>

*Figure 2.15: Correlations between the error in the efficiency values of single fibers and different fiber properties based on Monte Carlo simulated cosmic radiation. (All plots are arranged in the same way as in figure 2.9) Data: 30006*

Starting at figure 2.15b, the scatterplot shows the expected lack of correlation between error and  $z$  value. As seen before in the antiproton Monte Carlo simulation, there is the tendency for the lower super-layer to feature a higher bias than the upper super-layer. This can also be seen in figure 2.15c.

Perhaps the most interesting plot, however, is shown in figure 2.15a. The tendency to underestimate high efficiency fibers and overestimate low efficiency ones which could already be seen in figures 2.9a and 2.11a is much more prominent here. The MEM-algorithm acts in a similar way to a dynamic range compressor used in audio signal processing. The correlation between real efficiency values and errors is the reason that the blue histogram in the top right plot of figure 2.14 appears compressed compared to the orange one. Another point worth mentioning is that, in contrast to the results of the antiproton annihilation Monte Carlo simulations, figure 2.15a does not feature any extreme outliers in the error values.

The reason for the “compression” behavior is currently not known. However, as there are already large discrepancies between reconstructed and reference values in figure 2.13 it is obvious that improvements in the cosmic track reconstruction algorithm are needed. Since reconstructed tracks are used directly to identify missing fibers, it is highly likely that an improved reconstruction algorithm will also greatly benefit the MEM for cosmic radiation.

## 2.4 Cosmic Daemon

As calculated in figure 2.6b it takes hours of cosmic radiation to measure the efficiency of the FACT accurately. Since the detector can currently only acquire data 21.5 s at a time, a daemon was written in Python 3 to automate longer measurements. The daemon is able to perform the following tasks:

- (re)-starting of FACTDriver and auto-triggering every 21.5 s:  
An instance of FACTDriver is launched as a subprocess from the daemon by executing a CLI command. FACTDriver is given a period of 5 seconds to start up and establish a network connection with all 17 FPGAs. After that, the daemon sends an HTTP request to the aegisfact1 webserver to generate a trigger. After the trigger has been sent, FACTDriver is given 23 seconds to receive the trigger, acquire data and stream out the results to the DAQ server. After these 23 seconds the process is queried every 0.3 s to check if it has terminated. If it has, a new instance of FACTDriver is launched to acquire the next 21.5 s of data. If it has not concluded its operations and is still running after an additional 15 seconds it is assumed that something has gone wrong and the process is terminated. The cosmic daemon waits for the termination to be confirmed before starting the next instance of FACTDriver in order not to have multiple instances running at the same time. After the termination is confirmed a new instance of FACTDriver is launched.
- re-equalizing in order to compensate for temperature drifts:  
The equalization routine is currently run once per hour of acquisition. Since this procedure is known to occasionally fail, a fail-safe has been installed that attempts the procedure three times and after three failed attempts power-cycles the entire system including FPGAs and MPPCs.
- shutting down cleanly when issued a SIGKILL signal:  
As the cosmic daemon launches subprocesses it is important to ensure that all of them are terminated before the daemon itself shuts down. For this reason, whenever issued a SIGKILL signal, the cosmic daemon sends SIGKILL signals to all its subprocesses and waits for their termination. Only after confirmation that all subprocesses have terminated, the cosmic daemon itself shuts down.
- following a pre-programmed schedule:  
The ability to schedule the daemon has been achieved in two steps. Firstly, upon start-up, a schedule file is read. Every measurement cycle has a start and a stop time. If the current time falls in-between the two, the daemon assumes operation until the current time exceeds the stop time. Secondly, the daemon has been installed in cron on the aegisfact1 server and is invoked every minute in order to check for any scheduled measurements. If it does not find any scheduled measurement matching the current time, it shuts down. If it finds another instance of itself running and in a working state, it shuts down as well. Only if the time is correct and no other instance of the cosmic daemon is running, it will assume operation.
- protocol its actions:  
The daemon makes heavy use of the python logging module. Different levels of logging can be set. On the lowest level called “debug” the program produces a high amount of detailed output, mostly for developing purposes so that the program’s every step can be followed. On the higher “info” and “warning” levels the program’s output is much smaller and just gives basic information about the current state of operations and eventual warnings.

- veto ObsessiveFACT:  
Since the Cosmic daemon starts and terminates the FACTDriver instances on its own, it would run into conflict with the ObsessiveFACT daemon, which runs FACT-Driver instances as well. In order to avoid collisions between the daemons, the cosmic daemon places a veto for ObsessiveFACT that is revoked as soon as the cosmic daemon concludes operations.

Details about the location of the code can be found on the AEGIS Twiki<sup>8</sup>.

---

<sup>8</sup><https://twiki.cern.ch/twiki/bin/view/AEGIS/FACTCosmicDaemon>



Die approbierte gedruckte Originalversion dieser Diplomarbeit ist an der TU Wien Bibliothek verfügbar.  
The approved original version of this thesis is available in print at TU Wien Bibliothek.

## Chapter 3

# Efficiency Measurement Results

My drawing was not a picture of  
a hat. It was a picture of a boa  
constrictor digesting an elephant.

— ANTOINE DE SAINT-EXUPÉRY  
*Le Petit Prince*

This chapter covers the results of the efficiency measurements of the FACT detector. The first part is based on the measurements using antiproton annihilations. The MEM algorithm is applied to measurements of antiprotons annihilating on the trap walls and on the HDMCP. The efficiency results of both studies are compared and discussed with suggestions for future improvements.

In the next point, the feasibility of an efficiency cross-check through a comparison measurement between FACT and another detector system in the AEGIS experiment is explored. The second part of this chapter focuses on the analysis results of cosmic radiation data. The steps in the analysis closely follow the procedure introduced during the study of Monte Carlo simulated cosmic radiation.

Finally, results and starting points for future investigations are discussed in the third part of this chapter.

### 3.1 Antiproton Annihilations

The data for the trap wall antiproton annihilation efficiency analysis are runs from 139100 to 139103. The four runs were carried out as a scan over different rotating wall frequencies for the  $\bar{p}$  plasma expansion<sup>1</sup>. In order to get an idea of what the data from those runs look like, a standard analysis called `FACT_rec` is used. It has become a central workhorse and starting point for almost any FACT analysis as it is a good representation of what the detector “sees”. The analysis computes track and vertex reconstruction as detailed in subsections 1.3.1 and 1.3.2. It produces histograms of the  $z_s$  values for the tracks and  $z$  values of the vertices. Additionally, a histogram of the number of tracks per time as well as a 2-D histogram of  $z_s$  values per time are computed.

---

<sup>1</sup>Details about the antiproton trap settings can be found in the AEGIS run log: <https://aegisgateway.cern.ch:8443/eLog/RunLog/4590>

As an example for the trap wall annihilation procedure, the FACT\_rec output for run 139102 is shown in figure 3.1.

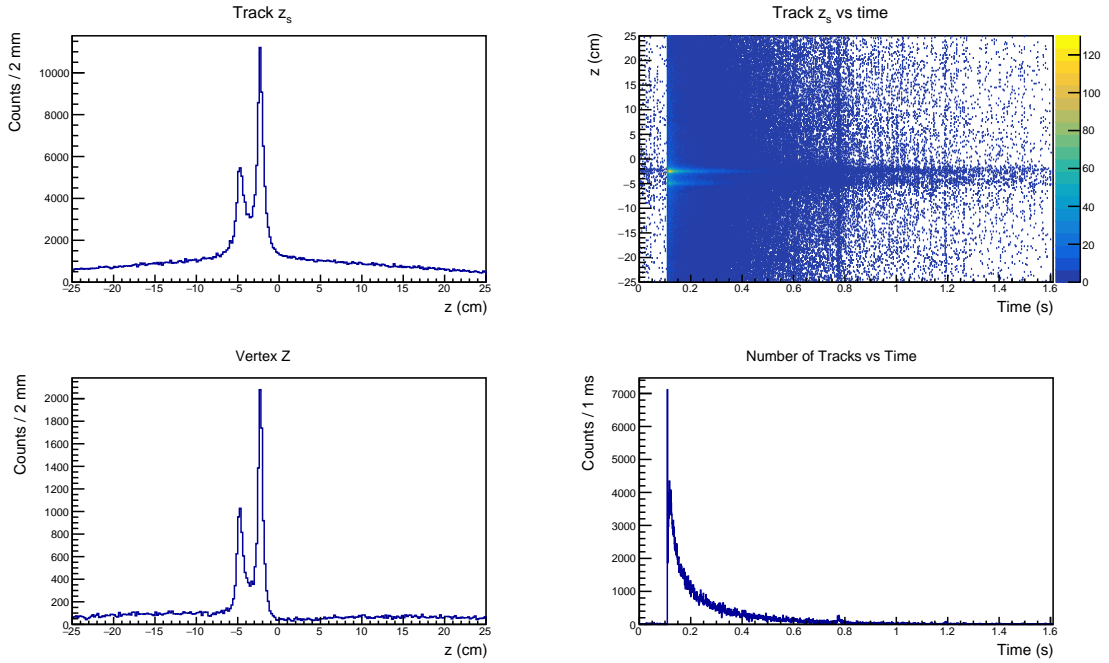


Figure 3.1: FACT\_rec analysis of the radial antiproton plasma expansion procedure  
 Top left: 1-D Histogram of the  $z_s$  values of all reconstructed tracks  
 Top right: 2-D Histogram of the  $z_s$  values of all reconstructed tracks along the  $y$ -axis vs. time along the  $x$ -axis  
 Bottom left: 1-D Histogram of the  $z$  values of all reconstructed vertices  
 Bottom right: 1-D Histogram of the number of tracks against time  
 gAn FACT\_rec\_min 139102

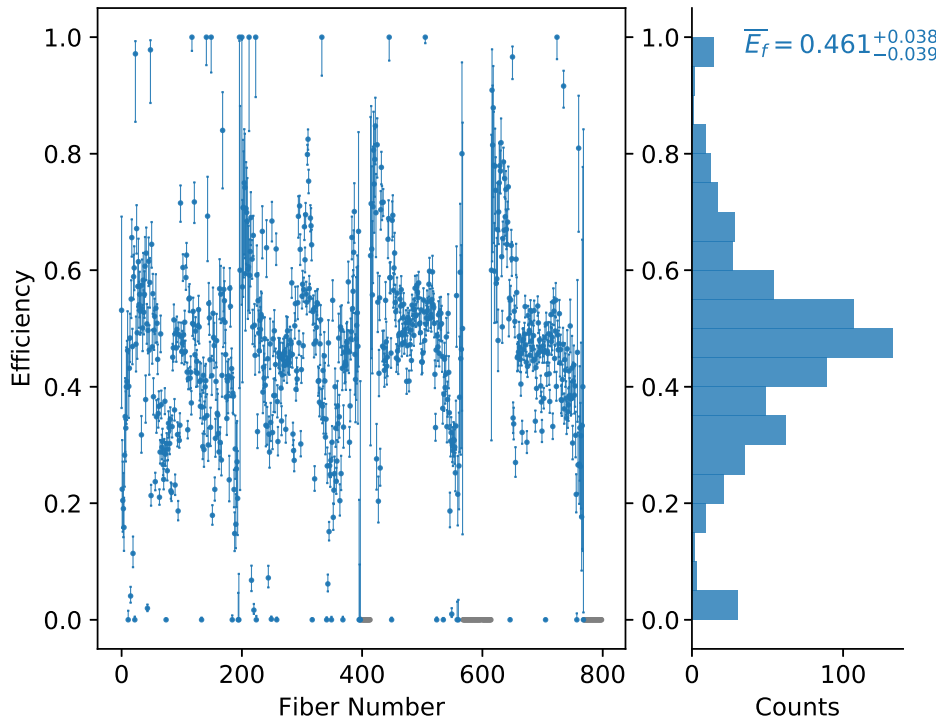
The left column of figure 3.1 shows a “double-peak” structure for both the track  $z_s$  and the vertex  $z$  distribution. Similar double-peak structures in the axial annihilation profile of trapped antiproton plasma have been observed by the ATHENA collaboration in 2004 [27]. The team found that the maxima in the annihilation profile coincided with the edges of the trapping electrodes. As a possible reason for this effect, it was hypothesized that slight displacements between neighboring electrodes resulted in an  $E \times B$  force acting to the antiprotons pushing them towards the trap walls where they annihilated. This effect was particularly pronounced at the two confining electrodes. The position of the trapping electrodes of the AEGIS-apparatus in FACT coordinates is currently not known to millimeter precision. However, the approximate position and distance between trapping electrodes are in good agreement with the plots in the left column of figure 3.1. Therefore it is likely that the same effect of increased antiproton annihilations due to imperfections in the trap is seen here as well.

The right column of figure 3.1 shows time information and can be used to study details about the dynamics of the antiproton plasma. One possible use case could be to find the best trap settings for annihilating the antiprotons as slowly as possible.

Despite the different settings in the antiproton trap parameters, all four runs 139100–139103 were used as input for the MEM algorithm.

Before the results of the analysis can be shown, one caveat needs to be addressed. There are a number of antiproton manipulation steps that need to be carried out by the AEGIS experimental apparatus before the radial expansion procedure can be performed. During these preparatory steps and also during the expansion procedure itself, the AD is periodically supplied with new antiprotons which are then transferred to the AEGIS experiment. During both of those steps, the injection of antiprotons into the AD and from the AD into the AEGIS experiment, a large number of antiprotons annihilate. This causes FACT to record a high number of tracks that are not related to antiproton annihilations in the trap. Since the timings of the AD relative to the start of the FACT acquisition are known, it can easily be checked if they fall within the acquisition window of FACT and therefore need to be vetoed. This was the case for runs 139100 and 139103, where time regions around 5.58s had to be excluded from the analysis. An automated check for any possible collisions between AD activity and the FACT acquisition window has been implemented in the `GetFACTs()` function of the `AEgFACT` class which is called at the beginning of every FACT analysis.

Now that interference from AD related activity has been addressed, the results of the analysis are presented in figure 3.2.



<https://twiki.cern.ch/twiki/bin/view/AEGIS/FACTEffRes>

*Figure 3.2: MEM for the trap wall antiproton annihilations*

*The left plot shows the individual fiber efficiency values with error bars and the right plot the distribution of the efficiencies. The average fiber efficiency with the average errors is shown in the top right.*

*gAn FACT\_Trap\_Eff 139100–139103*

As was concluded in section 2.2, the two results in figure 3.2 that can be trusted are the average fiber efficiency and the identified dead fibers. The average fiber efficiency as calculated by the MEM is around  $46^{+4}_{-4}\%$ , which translates to a charged pion tracking efficiency of  $50^{+6}_{-6}\%$ . The asymmetric uncertainty notation was used to indicate that the

uncertainty interval is in general not symmetric. A total amount of 26 dead fibers could be identified using the results of the MEM. Details and a complete list of all dead fibers found in both antiproton annihilation based efficiency studies can be found in appendix C.

As a side note, the average fiber efficiency value was calculated for all fibers, including the dead ones. The average efficiency without the dead fibers is around  $48^{+4}_{-4}\%$ . For further analysis, the complete fiber efficiency results of all efficiency studies, using antiprotons annihilations and cosmic radiation, can be found at the link next to figure 3.2.

The left plot of figure 3.2 shows patterns in the efficiency curve that indicate some correlation between a fiber's number and its efficiency value. Considering the results of the Monte Carlo simulation presented in figures 2.8 and 2.9, this is not surprising. However, as there is currently an incomplete understanding of the causes of the correlations, no Monte Carlo based corrections have been applied to the data. Therefore, results for efficiency values of single fibers need to be taken with a grain of salt. In order to get a more accurate measurement, improvements of the fiber identification algorithm are needed. One possible approach could be to use a weighted likelihood area around the reconstructed tracks instead of just identifying individual fibers.

Even though the efficiency values of single fibers need to be taken with a grain of salt, it is still worth investigating if there is any correlation between the bias setting of an MPPC and its fiber efficiency. This is particularly interesting as the efficiency of FACT could potentially be improved by increasing the gain values on low efficiency MPPCs. Figure 3.3 shows the correlation plot between fiber efficiency and bias value.

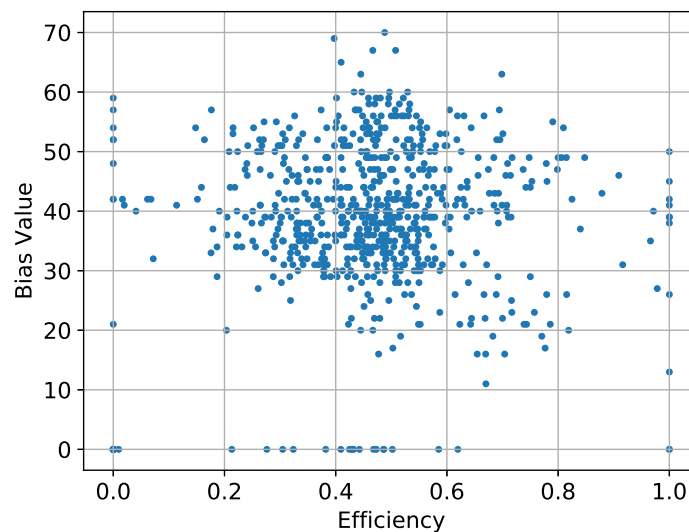


*Figure 3.3: Correlation plot of a fiber's measured efficiency and its bias value (gain of the MPPC) for antiproton annihilations on the trap wall.*

*Data: 139100–139103*

As stated above, the results shown in figure 3.3 need to be taken with a grain of salt as the fiber efficiency values are not completely reliable. Nonetheless, it is interesting that according to current knowledge fiber efficiency and bias value across the detector seem to lack correlation. This does not mean, however, that a fiber's efficiency cannot potentially be improved by increasing the bias of its MPPC. What the data in figure 3.3 suggest is that the optimal bias operating point is different for each MPPC. This hypothesis is



supported by the fact that the bias distributions of the high and low efficiency regions in figure 3.3 are not distinctly different. Additionally, even for a bias value of zero, there is a spread in efficiency values, suggesting that for some MPPCs the minimum bias setting is already enough to produce efficiencies  $> 0$ .

The second data source for the antiproton annihilation based MEM analysis are annihilations on the HDMCP. The data set for this analysis consists of runs 148020 to 148023<sup>2</sup>. FACT\_rec is used again to get an idea of the data, showing the results for run 148020 in figure 3.4.

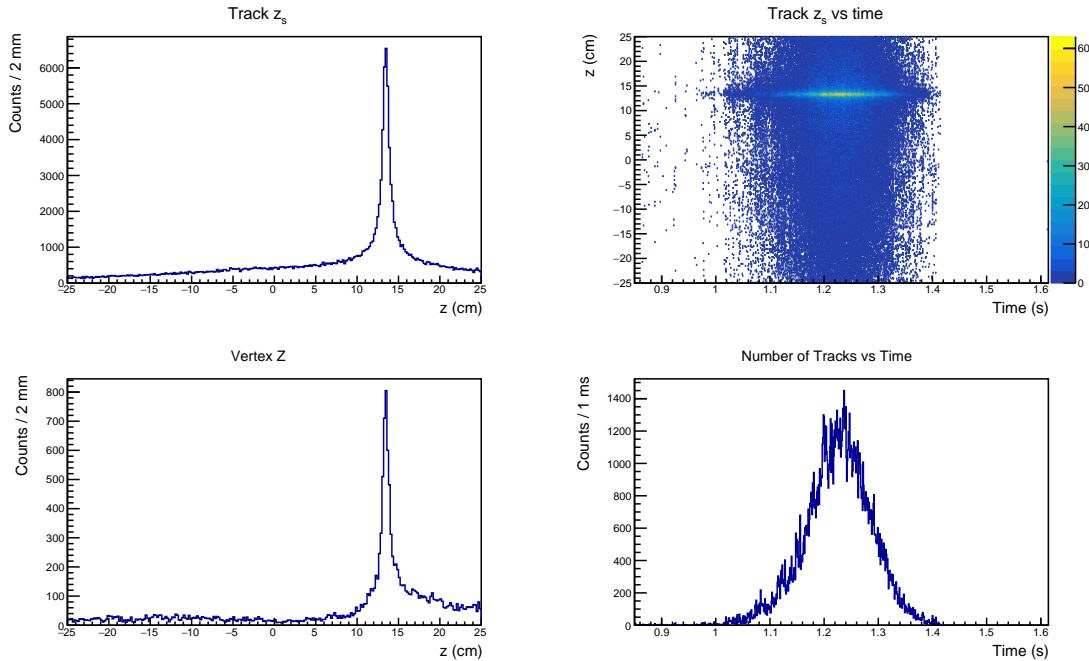


Figure 3.4: FACT\_rec analysis of antiproton annihilations on the HDMCP.  
gAn FACT\_rec\_min 148020

The peaks in the plots of the left column of figure 3.4 show the position of the HDMCP at around 13.6 cm. In the right column it can be seen that it takes around 300 ms for the antiproton plasma to completely spill out of the trap. The bottom right plot shows the number of tracks per time and can be used to get an estimate of the temperature of the antiproton plasma inside the trap. By fitting the rising edge of the blue curve with an exponential function, the temperature can be estimated from the resulting fit parameters. Before running the MEM analysis on the four HDMCP annihilation runs, they were checked for any interference with AD related activity but no overlaps with the FACT acquisition windows were found. Therefore, the four runs could be used as is for the MEM analysis and the results are shown in figure 3.5.

Similarly to the trap wall results, the two figures that can be trusted are the average fiber efficiency at around  $47^{+6}_{-6}\%$ , and the 21 dead channels that were identified. The average fiber efficiency translates to around  $52^{+9}_{-10}\%$  charged pion tracking efficiency. There is, however, a caveat to the average fiber efficiency value. As presented in figure 2.10, the average fiber efficiency had a bias of 0.038. Using this value to correct the measurement, however, is problematic. The reason can be seen in figure 2.11a which shows that the error in the MEM reconstructed efficiency correlates with the real efficiency value. Since the bias corresponds to the average error, it is safe to assume, that it is correlated with the

<sup>2</sup>Details can be found in the corresponding run log: <https://aegisgateway.cern.ch:8443/eelog/RunLog/4732>

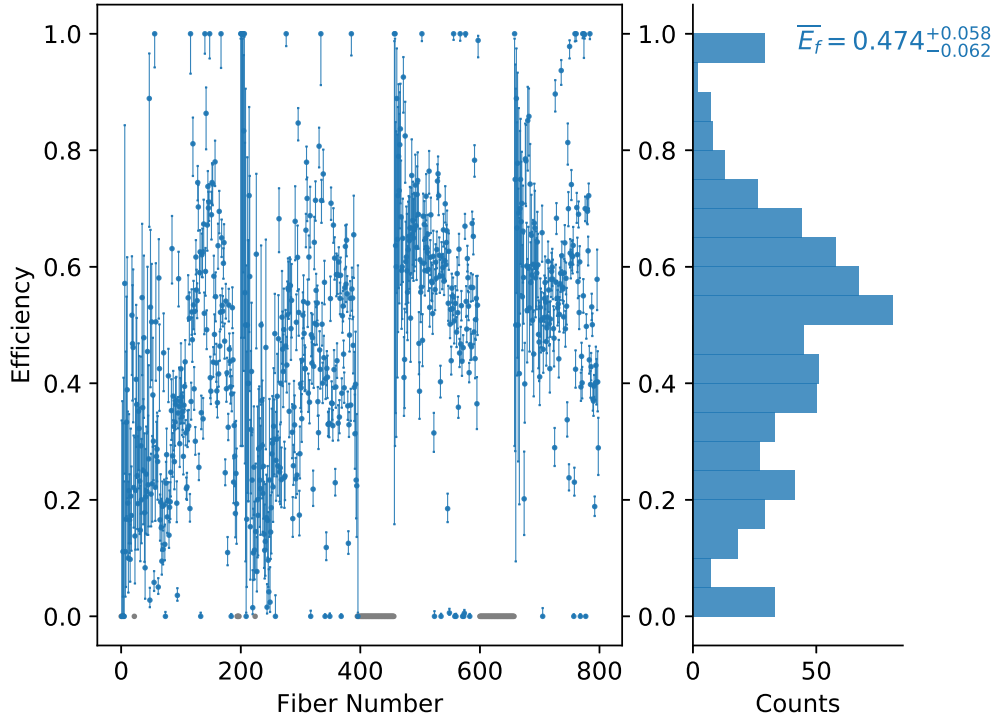


Figure 3.5: MEM results using antiproton annihilations on the HDMCP  
*gAn FACT\_HDMCP\_Eff 148020-148023*

average fiber efficiency as well. In other words, the bias of the average fiber efficiency depends on the value of the real average fiber efficiency. Therefore the aforementioned bias of 0.038 can only be considered to be applicable for 51% average fiber efficiency as used in the Monte Carlo study. In order to correct the values in figure 3.5 accurately, more in-depth Monte Carlo simulations of different fiber efficiencies are needed. As this information is currently not available, applying any correction to the results at this point would not be scientifically sound.

For the sake of completeness, it has to be said that the same argument of a biased average fiber efficiency result can also be made about the antiproton trap wall annihilation analysis. The only difference is that the bias value calculated in the Monte Carlo simulation (figure 2.8) is around four and a half times smaller than for the HDMCP annihilations. Therefore the influence on the measurement can be expected to be less dramatic. Nonetheless, for a highly accurate measurement, more Monte Carlo studies of antiproton annihilations on the trap wall are needed.

Another interesting detail that can be deduced from figure 3.5 concerns the average efficiency of the two super-layers. At around 0.4 it is significantly lower for the upper super-layer (fibers number 0–398) than for the lower super-layer (fibers number 400–798) where a value of 0.57 was measured.

In the same way as for antiproton trap wall annihilations, the single fiber efficiency values as measured using HDMCP annihilations cannot be considered to be completely reliable. As figure 2.9 shows, there are correlations in the fiber efficiency values whose origins are currently not understood.

Nonetheless, it is worth checking if the same lack of correlation between fiber efficiency and bias settings that was discovered for antiproton trap wall annihilations (figure 3.3) is also present for HDMCP annihilations. The results are shown in figure 3.6.

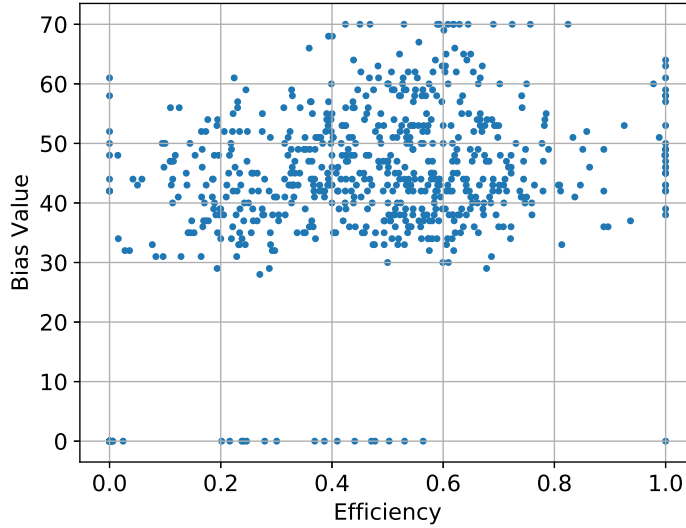


Figure 3.6: Correlation plot of a fiber’s measured efficiency and its bias value for antiproton annihilations on the HDMCP.

Data: 148020–148023

While the plot in figure 3.6 looks different to figure 3.3, the same general trend can be seen. Fiber efficiency and bias value do not seem correlated. For possible future efficiency improvements of FACT by bias increase it is therefore necessary to track the behavior of each fiber individually.

As an overview, table 3.1 shows the average fiber efficiency values calculated in this section together with the converted charged pion tracking efficiency along with their respective 95% confidence intervals.

Table 3.1: Overview of the average fiber efficiency values as determined by antiproton annihilations on the trap wall and on the HDMCP. The “CI” (confidence interval) column specifies the 95% confidence interval of the measured values.

Source Location	$\overline{E_f}$		Pion Tracking Eff.	
	Value	CI	Value	CI
Trap Wall	0.461	[0.422, 0.499]	0.503	[0.443, 0.560]
HDMCP	0.474	[0.411, 0.531]	0.522	[0.427, 0.609]

As there is currently insufficient information on the biases of the measured average fiber values, no corrections have been applied to the results shown in table 3.1. That being said, even taking into account possible corrections, the two values obtained through independent measurements are in good agreement as figure 3.7 shows.

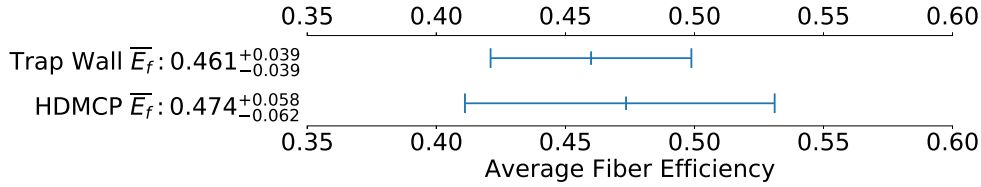


Figure 3.7: Visual representation of the two average fiber efficiency values from the trap wall and HDMCP annihilation efficiency analysis.

### 3.1.1 Comparison with the Outer Scintillators

While chapter 2 and the majority of the current chapter focus on determining the FACT efficiency without external reference, there is the possibility of a comparison measurement between FACT and another detector within the AEGIS experiment.

Located on the outside along the apparatus are a series of 12 scintillating slabs. Due to their location and detection mechanism they are referred to as the “Outer Scintillators”. The scintillating slabs are half pipe shaped, 10 cm long and 1 cm thick plastic elements made from EJ200<sup>3</sup>. As they are located on the outside of the AEGIS experimental apparatus, the slabs have an inner radius of 70 cm and cover an angle of 120°. Each slab is read out on both ends using photo-multipliers. The photo-multipliers are numbered and their numbers are used to name the individual scintillating slabs. The name of each slab starts with “SC” (for scintillator) followed by the two numbers of its photo-multipliers (e.g. SC2122, using photo-multipliers number 21 & 22). The photo-multipliers are used in coincidence mode and read out with a time resolution of 100 ns. This time resolution does not allow for any angular information on the particle’s intersection point with a given slab. Therefore, the Outer Scintillators act as counting detectors. Due to their coarse temporal and spatial resolution as well as their small solid angle coverage (around 2% per slab) for the production trap compared to FACT, the Outer Scintillators cannot be used to measure the efficiency values of single FACT fibers. What can be done is a comparison between the amount of tracks FACT is able to reconstruct and the amount of counts the Outer Scintillators record.

Ideally, we would want to use the ratio of FACT tracks and Outer Scintillator counts to obtain a value for the overall efficiency of the FACT detector. This could be used to cross-check the results of the MEM presented in the previous section. However, as will be discussed in the following, determining the overall efficiency of the FACT detector through comparison with the Outer Scintillators is a challenging task.

The first step towards such a measurement is determining the expected ratio  $X_{expected}$  of FACT tracks ( $FT$ ) and Scintillator counts ( $SC$ ). In order to calculate this figure, we need to know how many FACT tracks and Scintillator counts are expected per antiproton annihilation. The process of obtaining these values using Monte Carlo simulations will be covered later in this section. In order to account for the efficiency of both detectors, the Tracks/ $\bar{p}$  and the Counts/ $\bar{p}$  values need to be multiplied with their respective detection efficiencies. For FACT this is the average pion tracking efficiency  $\bar{E}_F$  as a function of the

<sup>3</sup><https://eljentechnology.com/products/plastic-scintillators/ej-200-ej-204-ej-208-ej-212>

average fiber efficiency  $\overline{E}_f$ , defined in formula 2.16. For the Outer Scintillators this is the overall efficiency ( $E_S$ ) which includes light attenuation in the slabs and efficiency of the photo-multipliers. Using those four quantities, the expected ratio can be calculated as follows:

$$\frac{Tracks/\overline{p} \cdot \overline{E}_F}{Counts/\overline{p} \cdot E_S} = X_{expected} \cdot \overline{E}_F \quad (3.1)$$

The average pion tracking efficiency  $\overline{E}_F$  of FACT was not included in  $X_{expected}$  since this is the quantity that we aim to measure.

Now that a model for the expected ratio has been derived, the next step is to conduct an antiproton annihilation measurement, acquire data with FACT and the Outer Scintillators and calculate the ratio of the signals:

$$\frac{FT}{SC} = X_{measured} \quad (3.2)$$

By equating expressions 3.2 and 3.1, the average pion tracking efficiency of FACT can be calculated:

$$\begin{aligned} X_{expected} \cdot \overline{E}_F &= X_{measured} \\ \overline{E}_F &= \frac{X_{measured}}{X_{expected}} \end{aligned} \quad (3.3)$$

Equation 3.3 defines the approach of the efficiency measurement of FACT through comparison with the Outer Scintillators. In order to carry out the measurement, the value for  $X_{expected}$ , which is comprised of  $Tracks/\overline{p}$ ,  $Counts/\overline{p}$  and  $E_S$ , needs to be calculated.

Starting with  $Counts/\overline{p}$ , this value has been calculated using the Monte Carlo simulation package Geant4, taking into account all the relevant geometrical parameters and the material composition of the experimental apparatus [28]. As the Outer Scintillators are spread out over the entire length of the AEGIS apparatus, the  $Counts/\overline{p}$  value varies from slab to slab. For this analysis SC2122 is used as it has the biggest solid angle overlap with FACT. Additionally, the  $Counts/\overline{p}$  value depends on the minimum energy deposited ( $E_{minS}$ ) inside the scintillator material which is needed for the photo-multipliers to register a particle. Table 3.2 shows values for three different values of required minimum deposited energy.

Table 3.2:  $Counts/\overline{p}$  for SC2122 for three different minimum deposited energies  $E_{minS}$  inside the detector material.

$E_{minS}$ (MeV)	$Counts/\overline{p} \times 10^{-2}$
$\geq 0.1$	$7.51 \pm 0.12$
$\geq 0.5$	$6.15 \pm 0.11$
$\geq 1$	$5.66 \pm 0.11$

As table 3.2 shows, for an efficiency measurement as introduced in equation 3.3, the  $Counts/\overline{p}$  value needs to be treated as a function of the minimum energy deposited  $E_{minS}$ . Currently,  $E_{minS}$  is not known accurately, which already adds uncertainty to a possible comparison measurement.

The next figure in formula 3.1 is the efficiency of the Outer Scintillators  $E_S$ . In previous measurements using cosmic radiation,  $E_S$  was determined at around 0.9 to 0.95.

In order to determine the Tracks/ $\bar{p}$  value for FACT, the solid angle coverage calculated in subsection 2.1.1 can be used. For antiprotons annihilating on the trap walls it is around 48.7% and for the HDMCP around 27.2%. Using those values around, 1.46 and 0.82 Tracks/ $\bar{p}$  respectively can be expected. However, those values do not take into account “fake” tracks that are reconstructed by the FACT as a result of track multiplicity (as defined in subsection 1.3.2). Also secondary low-energy particles generated by the interactions between direct antiproton annihilation products (mostly charged pions) and the materials of FACT, can result in additional tracks to be registered. The Monte Carlo simulations presented in figure 2.7 take into account both the track multiplicity and secondary particles and can be used to get a more accurate estimate of the Tracks/ $\bar{p}$  values. The calculation is done by counting the amount of tracks inside the grey signal-regions in figure 2.7 and comparing this amount to the  $2.5 \times 10^5$  antiprotons that were generated for the simulation. Since Monte Carlo simulations for perfect as well as 50% average fiber efficiency were carried out, the Tracks/ $\bar{p}$  value was calculated for both scenarios. This was done in order to check if the pion tracking efficiency  $\overline{E}_F$  can accurately predict by how much the Tracks/ $\bar{p}$  value decreases compared to perfect efficiency fibers. An overview of the results is shown in table 3.3.

*Table 3.3: Overview of the amount of tracks in the signal-regions for  $2.5 \times 10^5$  Monte Carlo simulated antiproton annihilations as seen in figure 2.7. The Tracks/ $\bar{p}$  values for 100% and 50% efficient fibers are shown along with the values calculated by solid angle.*

Source Location	$\overline{E}_f = 100\%$		$\overline{E}_f = 50\%$		Solid Angle
	Tracks	Tracks/ $\bar{p}$	Tracks	Tracks/ $\bar{p}$	Tracks/ $\bar{p}$
Trap wall	$8.62 \times 10^5$	3.45	$4.97 \times 10^5$	1.99	1.46
HDMCP	$3.27 \times 10^5$	1.31	$2.28 \times 10^5$	0.91	0.82

A number of points can be inferred from the results presented in table 3.3.

Firstly, the Tracks/ $\bar{p}$  values obtained through the Monte Carlo simulation are significantly higher than the solid angle would predict, even for 50% efficient fibers (the solid angle calculation assumes perfect efficiency).

Secondly, depending on the location of the source, the Tracks/ $\bar{p}$  values behave quite differently under changing fiber efficiency. For trap wall annihilations, the value decreases to around 58% which is very well in line with what the average pion tracking efficiency predicts  $\overline{E}_F(\overline{E}_f = 0.51) \approx 0.58$ . For the HDMCP on the other hand, Tracks/ $\bar{p}$  remains at 81% of the value for perfect fiber efficiency. This means that at least for the HDMCP annihilations  $\overline{E}_F$  defined according to formula 2.16 cannot be used to predict the change in Tracks/ $\bar{p}$  which would be necessary for an efficiency measurement. The exact curve, which describes  $\overline{E}_F(\overline{E}_f)$  as a function of the average fiber efficiency, can most likely only be obtained numerically by simulating a range of different average fiber efficiency values. For achieving accurate results this should be done for both antiproton annihilation locations.

Perhaps more importantly, though, Tracks/ $\bar{p}$  also depends on the minimum deposited energy  $E_{minF}$  which is required for the MPPCs to register a hit.

An estimate of this energy can be obtained using the numbers presented in [21]. Using a Monte Carlo simulation, the average energy deposited by a minimum ionizing particle crossing a scintillating fiber in FACT is calculated to be  $199 \pm 139$  keV. The scintillating fiber generates between 7000 and 10000 scintillation photons per 1 MeV of deposited energy. Together with the trapping efficiency of the scintillating fiber (around 5.4%) and the MPPC’s photon detection efficiency (around 20%), the average deposited energy trans-

lates to around 20 scintillation photons detected by the MPPC. For the newer MPPC model (Hamamatsu S12571-100C) the spectrum of detected scintillation photons for minimum ionizing particles was measured experimentally (figure 3.2 in [21]). The maximum of the spectrum was determined at  $(124 \pm 36)$ mV. Using the gain of the the MPPC of  $(6.3 \pm 0.11)$ mV per scintillation photon the maximum of the spectrum can be converted to  $20 \pm 6$  scintillation photons. In order to suppress thermal noise from the MPPC a default discriminator threshold of 32 mV is used. Assuming a gain of 6.3 mV per scintillation photon (this depends on the bias setting and the temperature of the sensor and also differs between individual MPPCs), this means that at least six scintillation photons need to be registered for the signal to be above the threshold. As 200 keV deposited energy correspond to around 20 scintillation photons, 6 scintillation photons correspond to around 60 keV of deposited energy. Using these 60 keV as  $E_{minF}$ , however, is problematic. The reason is that the scintillation photon spectrum (figure 3.2 from [21]) was measured in a test setup and not on the actual FACT detector using only the newer MPPC model. In order to use  $E_{minF}$  to accurately assess the FACT detector's efficiency through comparison with the Outer Scintillators, it should be measured for the FACT detector as it is currently mounted in the AEGIS experiment.

In the Monte Carlo simulation used to calculate the values in table 3.3 there is currently no minimum energy requirement used ( $E_{minF} = 0$  keV), so the values serve as upper limit estimations.

Updating equation 3.4 with the newly gained insight yields the following expression for the efficiency of FACT:

$$\overline{E}_F(\overline{E}_f) = \frac{X_{measured}}{X_{expected}} = \frac{FT}{SC} \cdot \frac{Counts/\overline{p}(E_{minS}) \cdot E_S}{Tracks/\overline{p}(E_{minF})} \quad (3.4)$$

Formula 3.4 contains three currently unknown parameters, the constants  $E_{minS}$  and  $E_{minF}$  as well as the variable  $\overline{E}_F(\overline{E}_f)$ . At least for trap wall annihilations  $\overline{E}_F(\overline{E}_f)$  seems to behave according to formula 2.16, although this should be double checked for Monte Carlo simulations for different average fiber efficiencies.

In short, the current understanding of FACT and the Outer Scintillators does not allow for an efficiency measurement of the FACT detector through comparison.

There is, however, a different way to look at formula 3.4. That is, not viewing it as an efficiency cross-check for the MEM results, but instead to use the  $\overline{E}_f$  value from the MEM as an input in order to calculate the minimum energy deposited  $E_{minF}$  needed for FACT to register a hit. Provided that the value of  $E_{minS}$  and the shape of  $\overline{E}_F(\overline{E}_f)$  are known, equation 3.4 can be used to experimentally determine  $E_{minF}$ . This could be particularly interesting as it provides a way to measure the previously estimated value of 60 keV.

Even though neither the efficiency cross-check nor the minimum energy measurement is currently possible, there is still valuable insight to be gained by comparing the signals of the two detectors.

### 3. EFFICIENCY MEASUREMENT RESULTS

The data-set for the comparison analysis consists of the same runs that were used in the previous section for antiproton annihilations on the trap wall and on the HDMCP. Keeping the same order and starting with the trap wall annihilation data, the time-resolved comparison analysis is shown for run 139013 in figure 3.8.

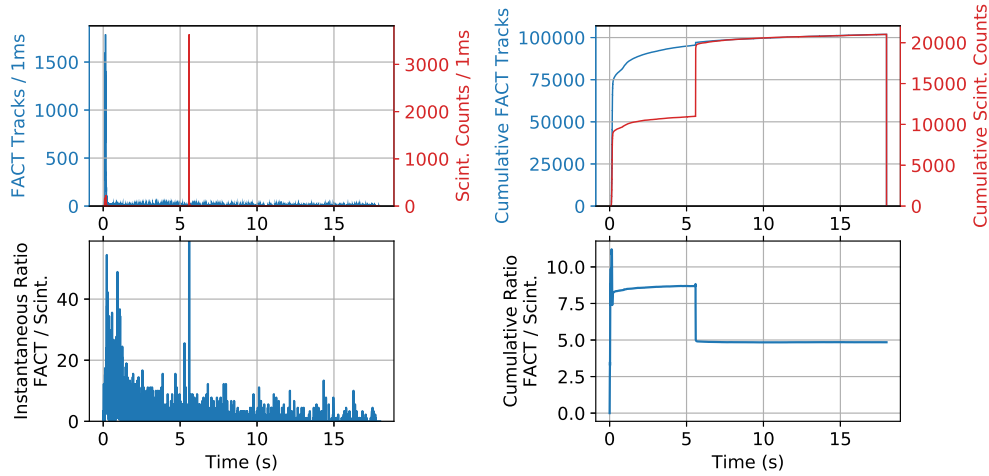


Figure 3.8: Time-resolved comparison between the amount of tracks recorded by FACT and the counts of SC2122 for antiproton annihilations on the trap wall.

Top left: FACT track and SC2122 count rates per 1 ms.

Top right: Cumulative curves of the top left plot.

Bottom left: Instantaneous ratio of FACT tracks and SC2122 counts

Bottom right: Ratio of the cumulative curves.

`gAn FACT_HDMCP_eff 139103`

`gAn Scints 139103`

The first feature that immediately stands out from the top left plot in figure 3.8 is the peak in the count rate of SC2122 shortly after 5 s. This peak is caused by antiprotons annihilating during the injection from the AD into the AEGIS experiment. As this is not related to any activity in the final trap of the experiment, this time region needs to be excluded in order to get an accurate value for the ratio of FACT tracks and SC2122 counts. It is worth nothing, though, that the AD activity related antiproton annihilations cause the cumulative of SC2122 counts to rise dramatically more than the number of tracks for FACT. The reason for this behaviour can be found by focusing on the beginning of the acquisition shown in figure 3.9.

<https://twiki.cern.ch/twiki/bin/view/AEGIS/FACTScintComp>



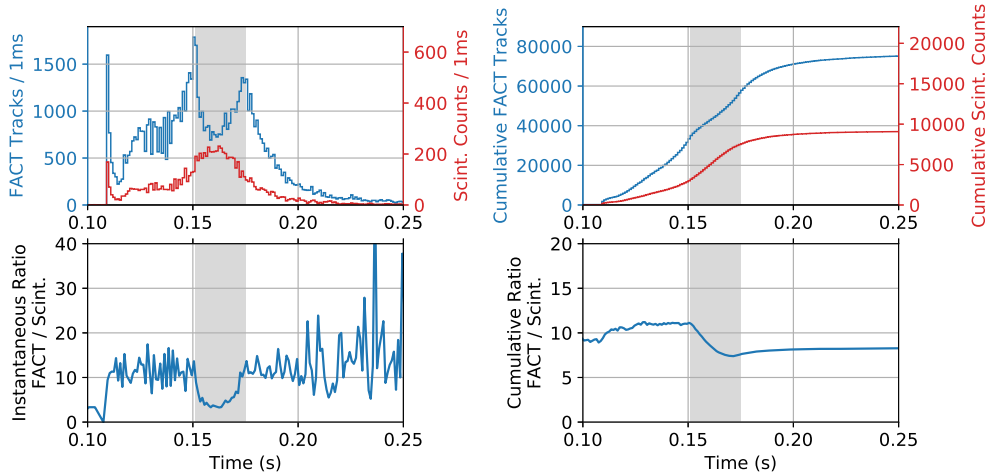


Figure 3.9: Zoomed in view of figure 3.8. The grey areas mark the saturation region for FACT. Here the rate of FACT tracks drops down rapidly while the count rate of SC2122 continues to rise. After around 250 ms FACT seems to stabilize again and the instantaneous ratio returns back to the previous level.

`gAn FACT_HDMCP_eff 139103`

`gAn Scints 139103`

<https://twiki.cern.ch/twiki/bin/view/AEGIS/FACTScintComp>

As the top left plot in figure 3.9 shows both curves have similar shapes until they enter the area marked in grey. Starting at around 0.15s the rate of FACT tracks drops down while the count-rate from SC2122 continues to rise. After around 250 ms the FACT track rate stabilizes again. This temporary loss in efficiency can be seen clearly in the bottom left plot as the instantaneous ratio decreases sharply. The most likely reason for this behaviour of FACT is a too high antiproton annihilation rate. Since the FACT MPPCs are operated in avalanche mode, they have a recovery time of between 100 ns and 200 ns. Any additional scintillation photons that reach the sensor in this time period, can only be registered with a very low detection efficiency. The rate of FACT tracks which peaks at 1600 tracks per ms (1.6 MHz) seems to be too high for the MPPCs to recover in time to register the next charged particle. The saturation effect also explains why the AD activity related peak in figure 3.8 has a more dramatic impact on SC2122 than on FACT. The antiproton annihilation rate is so high that after an initial surge in tracks, FACT saturates and does not record any more charged pions while SC2122 does not saturate and keeps detecting charged particles.

After the saturation effect was discovered, the rest of the data-set, runs 139100–139102, were investigated for similar signs of saturation. Run 139102 was found to also feature a region of decreased FACT efficiency as a result of a too high instantaneous antiproton annihilation rate. Conversely, the runs 139100 and 139101 did not show any signs of saturation.

The presence of saturation regions impacts the amount of tracks that FACT is able to record. Therefore, including those regions in the comparison measurement would lead to a wrong picture of the normal, non-saturated, efficiency of FACT. As a result, table 3.4 shows the cumulative ratios of FACT tracks and SC2122 counts excluding the saturation regions. Another figure which impacts the analysis in a much less dramatic way, but plays a role nonetheless is the noise rate of the SC2122. For the numbers presented in table 3.4 a typical noise rate of 100 Hz was used.

Table 3.4: Overview of the number of FACT tracks, SC2122 counts and the cumulative ratios, excluding all saturation regions and AD activities.

Run Number	FACT Tracks	SC2122 Counts	Ratio
139100	41,607	3,668	11.34
139101	33,989	3,583	9.49
139102	106,184	9,872	10.76
139103	70,913	6,399	11.08
$\Sigma$	252,693	23,522	10.74

As runs 139102 and 139103 were found to feature saturation regions, a possible influence on the results of the MEM analysis presented in the previous section was investigated. Interestingly enough, excluding the saturation regions was found to have no significant impact on the results of the MEM. The most likely explanation for this somewhat counter intuitive robustness of the MEM against saturation effects, is that the MEM can only work with the tracks FACT reconstructs. This means that tracks which are missing can, per definition of the MEM, not have any influence on the result.

The same comparison analysis as for the trap wall annihilation data was carried out for antiproton annihilations on the HDMCP as well. As an example, the result for run 148020 is shown in figure 3.10.

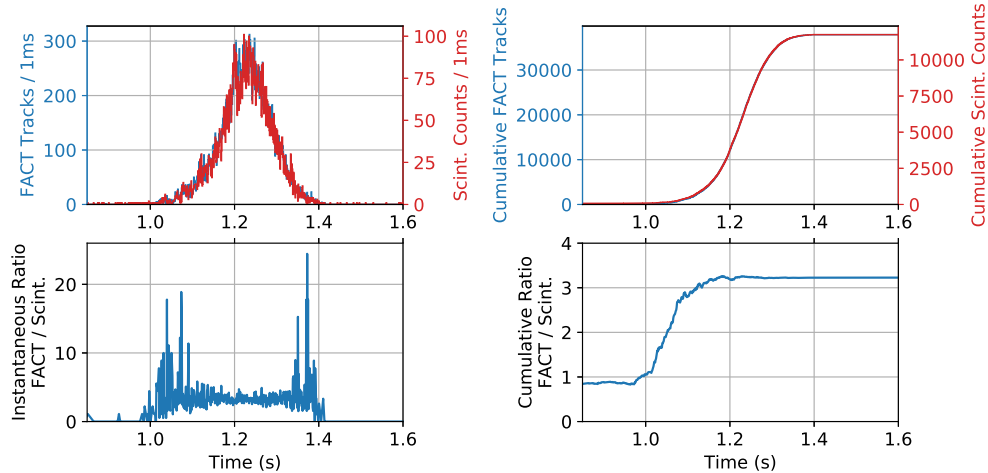


Figure 3.10: Time-resolved Comparison between the amount of FACT tracks and the counts of SC2122 for antiproton annihilations on the HDMCP.

*gAn FACT\_HDMCP\_eff 148020*

*gAn Scints 148020*

<https://twiki.cern.ch/twiki/bin/view/AEGIS/FACTScintComp>

Compared to the results from the trap wall annihilations, the run shown in figure 3.10 as well as the three other runs that were analyzed do not show any signs of a saturation effect. The final results of the cumulative ratios for each run are shown in table 3.5.

As a side note for future analyses, the fact that runs 148020–148023 did not show any signs of a saturation effect of FACT does not mean it can be excluded in general for antiprotons annihilating on the HDMCP. In any analysis that includes the absolute number of reconstructed FACT tracks, one should always use the Outer Scintillators to check for any saturation regions.

Table 3.5: Overview of the number of FACT tracks, SC2122 counts and the cumulative ratios for measured antiproton annihilations on the trap wall .

Run Number	FACT Tracks	SC2122 Counts	Ratio
148020	37,909	11,710	3.24
148021	39,583	12,249	3.23
148022	37,416	11,270	3.32
148023	36,808	11,632	3.16
$\Sigma$	151,716	46,861	3.24

In conclusion, even though the comparison between FACT and the Outer Scintillators can currently not be used to cross-check the FACT efficiency or determine the value of  $E_{minF}$  it is still important to compare the two detectors. Particularly the saturation effect that occurs for FACT for too high antiproton annihilation rates cannot be identified otherwise. Additionally, the calculated ratios can still be used as a benchmark for future tests and optimizations of the FACT efficiency.

## 3.2 Cosmic Muons

For the MEM measurement with cosmic radiation, a total of 787 20-second long segments of data were acquired with FACTDriver. This amounts to a total time of 15,740 s or 4 h22 min20 s.

The analysis was carried out as outlined in section 3.2, starting with the identification of cosmic-fingerprints. In the recorded 15,740 seconds of data, a total of 18,530 cosmic-fingerprints were found.

Assuming that the amount of cosmic muons in a time window follows a Poisson distribution, the uncertainty in the amount of cosmic-fingerprints recorded can be estimated as:  $\sqrt{n} = \sqrt{18530} \approx 136$ . This corresponds to a recorded “counting-rate” of:  $(18530 \pm 136)/15740 = (1.18 \pm 0.01)$  Hz.

From the cosmic radiation Monte Carlo simulation we know to expect around 2.9 Hz  $\pm 10\%$ . This figure was calculated without a minimum energy deposited requirement so it should be regarded as an upper limit to rate which can realistically be expected.

Using the recorded and the expected counting rate, a lower limit to the cosmic counting-efficiency ( $CCE$ ) of FACT defined as ratio of the two rates can be calculated:

$$CCE = \frac{1.18 \pm 0.01}{2.9 \pm 0.29} = 0.407 \pm 0.041 \quad (3.5)$$

With the model for cosmic muon counting efficiency as defined in equation 2.17, a lower limit to the average fiber efficiency that corresponds to the measured cosmic counting efficiency can be calculated. The value for the lower limit to the average fiber efficiency based on the cosmic counting efficiency was calculated to be  $0.38_{-0.020}^{+0.024}$ . As covered in section 3.2 following equation 2.21, the model from equation 2.17 that relates average fiber efficiency and cosmic counting efficiency is not perfectly accurate. However, as the discrepancy is not too dramatic and not studied thoroughly enough at the moment, no corrections were applied.

After the identification of cosmic-fingerprints, the next step in analysing cosmic radiation data is track reconstruction. The performance of the fitting algorithm is shown in table 3.6.

Table 3.6: Performance of the fitting algorithm for 15,740 seconds of cosmic radiation data. The quantity “Total Amount” corresponds to the number of cosmic fingerprints identified in the analysis.

Category	Amount	Fraction (%)
Fitting Failed	846	4.57
Geometry Cut	6,933	37.41
Complete Miss	2,389	12.89
Good Cosmics	8,362	45.13
Total Amount	18,530	100.00

Compared to the performance of the fitting algorithm for Monte Carlo simulated data shown in table 2.6 it can be noted that the difference lies mostly in the lower percentage of “good cosmics”.

With the track reconstruction done and the “good cosmics” identified, the next step is to analyze the distributions of the reconstructed  $z_0$ ,  $r_{min}$  and  $\theta$  values shown in figure 3.11.

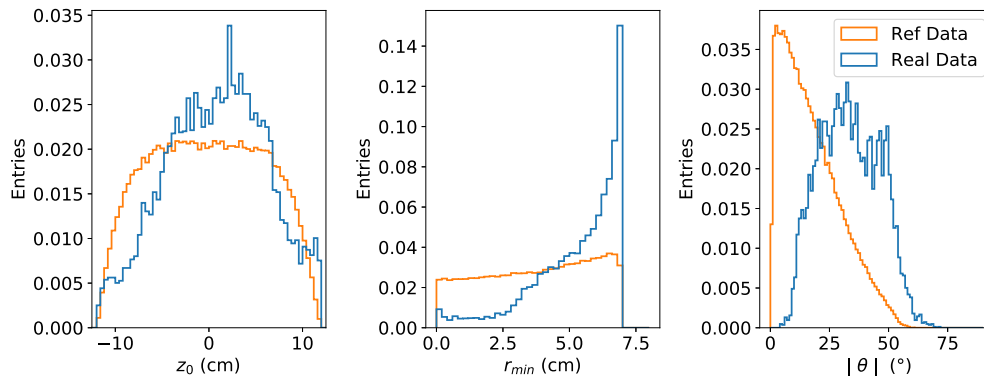


Figure 3.11: Distributions of  $z_0$ ,  $r_{min}$  and  $\theta$  for “good cosmic” trajectories. The reconstructed values from the 15,740 seconds of recorded cosmic data are shown in blue. As a reference for the shape of the target distributions, the Monte Carlo generated values of cosmic muons (as seen in figure 2.13) are plotted in orange. All distributions have been normalized to the sum of their bins to allow for easier qualitative comparison.

`An FACT_cosmics_Eff_bin [placeholder data]`

When comparing the measured curve in blue to the orange reference in figure 3.11, it becomes clear that especially the  $r_{min}$  and  $\theta$  values differ drastically from the reference. Interestingly, the preference for high  $r_{min}$  values and the shift in the  $\theta$  distribution are both features that were previously observed in figure 2.13. The distributions of the simulated 50% average fiber efficiency data, shown as the green curves, exhibited similar albeit less extreme characteristics. This means that for developing and testing a better cosmic track reconstruction algorithm, a Monte Carlo simulation with imperfect fiber efficiency values, appears to be a solid starting point.

As a side note for future analyses, the raw cosmic radiation data are located on the aegisfact1 server in the following folder `aegisfact1:/Omnibus/FACTDatabase/CosmicData_Baseline`. The data is stored in binary files in the following format: two 1-byte long unsigned integers and two 8-byte long unsigned integers. The two 1-byte integers spec-

<https://twiki.cern.ch/twiki/bin/view/AEGIS/FACTEffRes>

ify the FPGA and MPPC number and the two 8-byte long integers describe the rising edge time and the time over threshold both in nanoseconds. The gAn analysis `FACT_cosmics_Eff_bin` can read those binary files and performs the cosmic radiation analysis. More details can be found on the AEGIS-TWiki page that the link next to figure 3.11 points to.

As the MEM depends on accurate track reconstruction in order to correctly identify missing fibers, the discrepancies in the  $r_{min}$  and  $\theta$  distributions seen in figure 3.11 are worrisome. With the current cosmic track reconstruction algorithm, an MEM based analysis cannot be expected to produce correct results. Nonetheless, in order to investigate how the shortcomings of the current track reconstruction algorithm manifest themselves, the MEM analysis was performed for the recorded cosmic data. The results are shown in figure 3.12.

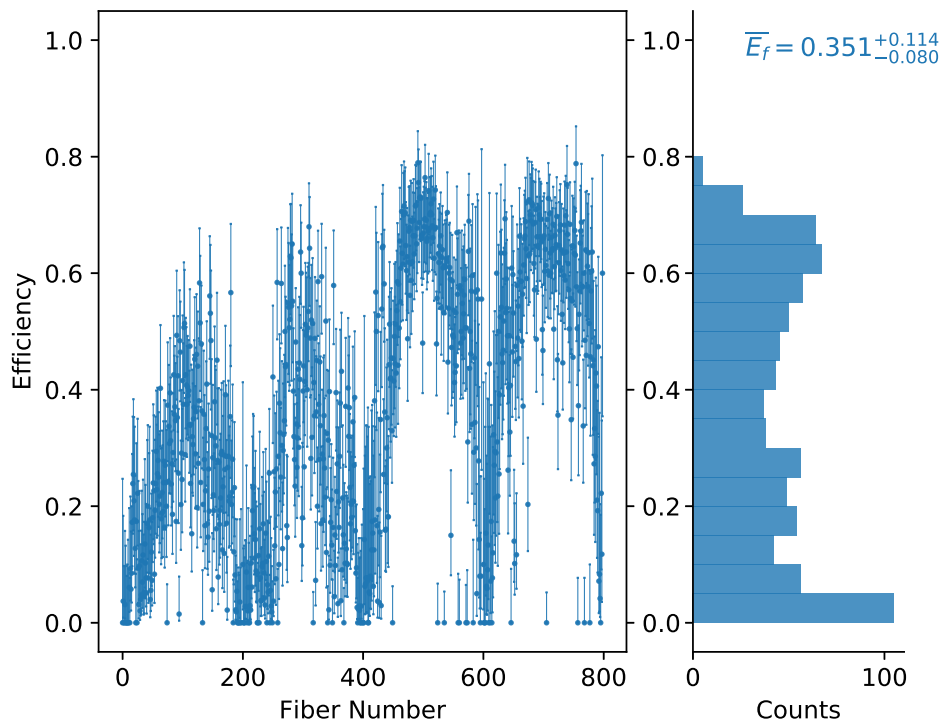


Figure 3.12: Results of the MEM based on 15740 seconds of cosmic radiation  
gAn `FACT_cosmics_Eff_bin` [placeholder data]

Figure 3.12 shows a clear correlation between fiber number and efficiency value. More precisely, two different correlations can be identified.

Firstly, fibers towards the center of a layer (fiber numbers around 100, 300, 500 and 700) exhibit significantly higher efficiencies than fibers on the layer's borders (fiber numbers around 0, 200, 400, 600 and 800). This correlation is unexpected, considering that the results of the Monte Carlo simulation shown in figure 2.14 showed no signs of such a pattern. As stated before, rather than investigating the reasons for this correlation it is advised to first improve the reconstruction algorithm in order to enable the use of cosmic radiation for efficiency measurements.

The second correlation concerns the average values of each super-layer (fibers 0–398 form the outer, fibers 400–798 the inner super-layer). The inner super-layer features an average efficiency of 0.46 while the outer super-layer has a significantly lower value of 0.24. This tendency was already observed in the analysis of the simulated data, but it is much more prominent now.

Considering the discrepancies between simulation and real data seen in figure 3.11 and the patterns in figure 3.12, none of the MEM results, including the average fiber efficiency, can be classified as trustworthy.

The only figure from the current chapter which can be viewed as a reliable result is the cosmic counting rate of 1.18 Hz. Due to incomplete information on the minimum energy deposited which is required for the FACT to register a hit, the cosmic counting efficiency and the resulting average fiber efficiency, can only be considered lower limit estimates.

That being said, the state of measuring cosmic radiation with FACT is better than it may seem now. The theoretical groundwork of deriving the signals patterns that cosmic muons generate in FACT and the hyperbolic track reconstruction has been covered in subsection 1.3.3.

Using Monte Carlo generated data, the track reconstruction algorithm and the MEM were tested in section 2.3. Shortcomings in the hyperbolic fitting procedure were identified through the distributions of the reconstructed parameters.

Similar characteristics were seen in the distributions for the real recorded cosmic data presented in this section. This means that for improving the track reconstruction algorithm, which presents the current bottleneck of the analysis, a Monte Carlo simulations is a useful tool. During the studies of cosmic radiation, a number of C++ classes and analysis scripts were developed in gAn. Appendix A provides an overview of the current state and points to parts in the code where future improvements might start.

### 3.3 Discussion and Outlook

To begin the discussion, it is useful to remind ourselves of the current main goal of the AEGIS experiment in order to understand how an efficiency measurement of FACT ties into it. As this current goal is to establish the production of antihydrogen, it is important to know how many tracks per antihydrogen annihilation FACT is expected to record. Together with the expected amount of produced antihydrogen this figure can be used to calculate how much data taking is needed to establish the formation of antihydrogen with a given statistical certainty.

This amount of tracks per antihydrogen annihilation can be estimated back-of-the-envelope by taking the product of the average charged pion multiplicity (around 3), solid angle coverage (around 50 %) and pion tracking efficiency measured in section 3.1 (around 50 %):

$$\text{Tracks}/\overline{H} = 3 \cdot 0.5 \cdot 0.5 = 0.75 \quad (3.6)$$

In its current state FACT is expected to record 0.75 tracks for each antihydrogen atom produced and annihilated in the AEGIS experiment. In order to establish the formation of antihydrogen in the shortest time possible, it is important to maximise the value of  $\text{Tracks}/\overline{H}$ . Since the first two factors in formula 3.6 (the charged pion multiplicity and the solid angle coverage) are constants, the FACT efficiency is the only place where improvements can be made.

With its (theoretical) ability to determine the efficiency values of single fibers, the MEM can serve as a central tool in improving the detection efficiency of FACT. To be precise, there are two different ways, in which the MEM can be used in this process.

Firstly, it can identify dead MPPCs or faulty fiber connections which can be repaired for an immediate boost in detection efficiency. For this purpose, table C.1 in appendix C features a full list of the dead fibers found in the analysis of antiproton annihilations in section 3.1. This table can be used as is to improve the FACT efficiency on a hardware level.

Secondly, the overall efficiency of FACT may be improved by increasing the bias values of the least efficient fibers. This second part, however, is currently problematic as the efficiency measurement on the single fiber level has been found to contain biases (as shown in figures 2.9, 2.11 and 2.15). For antiproton annihilation based measurements the situation can most likely be improved by developing a better fiber identification algorithm. For cosmic radiation, the road block is the hyperbolic track reconstruction procedure. Appendix A shows the locations of the current versions of these algorithms inside the gAn C++ code (`AEgFACTEfficiency` and `AEgCosmicReconstructor`). In this way, starting points for improvements can be found easily. Once the biases in the efficiency measurement have been addressed, the efficiency of the FACT detector can be improved with the help of the MEM using either cosmic radiation or antiproton annihilations.

Additionally FACT should be combined with the Outer Scintillators in order to gain more information. As discussed in subsection 3.1.1 the comparison between the two systems can lead to valuable insights such as the saturation effect of FACT. Any type of FACT analysis which uses the absolute number of reconstructed tracks has to be cross-checked by comparison with the Outer Scintillators in order to avoid wrong conclusions.



Die approbierte gedruckte Originalversion dieser Diplomarbeit ist an der TU Wien Bibliothek verfügbar.  
The approved original version of this thesis is available in print at TU Wien Bibliothek.



# Conclusion

Time, Dr. Freeman? Is it really that time again? It seems as if you only just arrived.

— THE G-MAN  
*Half-Life 2*

The first step in achieving the goal of the AEGIS experiment, a gravity measurement of antihydrogen, is demonstrating its production. As the main detector for this task, FACT plays a central role in this endeavour.

The aim of this thesis was to provide an overview of the FACT detector's design, measurement capabilities, describe a way to determine its efficiency and present the results of the efficiency analysis. Additionally and equally, if not more, importantly, this thesis was written to be a starting point and a handbook for everyone working on FACT in the future.

The first chapter covered the basics of the detector and its measurement capabilities. Particularly important was the derivation of an analysis strategy for track and vertex reconstruction. The last part of chapter 1 described the analysis software gAn which was used to do all data analysis in this thesis. Appendix A provides a more technical, C++ code focused description of the classes and analysis scripts developed for this thesis. Combined, these sections are intended to serve as a manual for anyone interested in the analysis of FACT data.

In chapter 2 the derivation of a method to measure the efficiency of the individual fibers of FACT without the need of an external reference is described. By making use of the detector's tracking capabilities, a generalized approach dubbed the "Münchhausen efficiency method" was developed. This MEM can be used to measure the efficiency of the smallest units of any pixel or pixel-like particle tracking detector.

In the next step it was found that an accurate measurement of the efficiency of FACT is possible using a few antiproton shots from the AD or around a day of cosmic radiation. Following this investigation, Monte Carlo simulated data were used to test the newly developed MEM for its claimed abilities to accurately measure the efficiency of single fibers. While the average fiber efficiency reconstruction worked well, discrepancies were found on the individual fiber level. Investigations into the correlations of the fiber errors lead to conclude that the tracking and fiber identification algorithms are the places where future improvements should start.

In the third and final chapter, the results of MEM based efficiency studies with antiproton annihilations and cosmic radiation are presented along with a comparison measurement with the Outer Scintillators.

For the antiproton studies, annihilations on two different locations, the antiproton trap walls and the HDMCP were analyzed. In terms of the average fiber efficiency, the two sets of data showed good agreement with values of around 46 %.

Following the MEM studies, the possibility of cross-checking this efficiency value through a comparison measurement with the Outer Scintillators was explored. While this is currently

not possible due to insufficient information about both detector systems, a saturation effect of FACT was discovered. This temporary loss in detection efficiency as a result of a too high antiproton annihilation rate could only be identified through comparison with the Outer Scintillators and should always be considered in future analyses.

Lastly, the results of the cosmic radiation studies were presented. Unfortunately, the problems in the track reconstruction algorithm meant that none of the MEM's findings could be viewed as accurate. The positive results from the cosmic radiation studies include the measured counting rate and the developed acquisition and analysis software infrastructure.

The next step in the work for FACT is to improve its detection efficiency. Fixing the dead channels which can be found in appendix C is an immediate way to boost the detection efficiency of the detector.

The second, more sophisticated, way involves increasing the gain values on the least efficient MPPCs. With its ability to measure the efficiency of single fibers the MEM can play a central role in this process.

The method's current limitations and future improvements were discussed in detail in chapters 2 and 3 in order to enable a smooth continuation of the efforts to improve FACT and contribute to the overall success of the AEGIS experiment.

# Appendices



Die approbierte gedruckte Originalversion dieser Diplomarbeit ist an der TU Wien Bibliothek verfügbar.  
The approved original version of this thesis is available in print at TU Wien Bibliothek.

## Appendix A

# AEgFACT Analysis Index

In this section an overview of the FACT part of the AEGIS analysis software gAn is presented.

For any newcomer to FACT wanting to start writing their own analyses, this is the place to start. It is advised to carefully read this section in order to understand how the FACT analysis classes interlink. A tutorial analysis called `FACT_tutorial` was created to illustrate the steps from raw data to finished histograms. It consists of an extensively commented minimum working example of the `FACT_rec` analysis including some practice tasks. The solutions to the practice tasks can be found here<sup>1</sup>.

Instructions on how to download and install gAn as well as basics can be found on the AEGIS Twiki<sup>2</sup>.

The git repository used for development and distribution of gAn can be found here<sup>3</sup>.

The analysis tools for this thesis were originally developed on the git branch `philip_thesis` and then patched into the master branch.

As most C++ software gAn consists of two parts, classes that define the behavior of data structures and scripts which use instances of those classes to perform certain tasks.

---

<sup>1</sup>[https://twiki.cern.ch/twiki/bin/view/AEGIS/FACT\\_tutorial](https://twiki.cern.ch/twiki/bin/view/AEGIS/FACT_tutorial)

<sup>2</sup><https://twiki.cern.ch/twiki/bin/view/AEGIS/AEgISOffline>

<sup>3</sup><https://gitlab.cern.ch/aegis-offline/gAn>

Table A.1 provides an overview of all FACT related classes as well as the most important analysis scripts created for this thesis. All names written in typewriter font in table A.1 link to the detailed descriptions in this analysis index.

*Table A.1: Overview of all FACT related classes and the most important analysis scripts.*

Classes	Analysis Scripts
Containers	Track Reconstruction
AEGFACT	FACT_rec
AEGFACTEvent	FACT_rec_min
FACT Objects	FACT_cosmics_rec
AEGFACTHit	Efficiency
AEGFACTCluster	FACT_Tracp_Eff
AEGFACTTrack	FACT_HDMCP_Eff
AEGFACTVertex	FACT_cosmics_Eff
AEGFACTCosmic	FACT_cosmics_Eff_bin
Reconstructors	Misc.
AEGVertexReconstructor	FACT_tutorial
AEGCosmicReconstructor	FACT_cosmics_read_MC
Efficiency	FACT_positrons
AEGFACTEfficiency	FACT_source

For an easy overview the classes and analysis scripts in table A.1 have been grouped into categories.

The “Classes” column starts with the two containers, `AEGFACT` and `AEGFACTEvent`. `AEGFACT` implements a number of automated low-level tasks for reading and processing of raw data. The result of this processing step is a vector of `AEGFACTEvent` instances. Each `AEGFACTEvent` has a timestamp in nanoseconds and holds a vector of `AEGFACTHit` instances.

In order to perform clustering, track and vertex reconstruction, an `AEGVertexReconstructor` instance is created through input of an `AEGFACTEvent`.

For reconstruction of cosmic trajectories, an `AEGCosmicReconstructor` instance is created from an `AEGVertexReconstructor`. The `AEGCosmicReconstructor` object then holds instances of the `AEGFACTCosmic` class.

The `AEGFACTEfficiency` class takes a vector of `AEGFACTEvent` instances as input and performs the complete efficiency analysis automatically.

All classes are located in the folder `gAn/src/fact`.

The “Analysis Scripts” column features three categories.

The first, “Track Reconstruction” has two analyses for charged pions and one for cosmic particle tracking. `FACT_rec` is the standard analysis for reconstructing tracks and vertices of charged pions from antiproton annihilations. During the second half of the 2018 AD run a multi trigger scheme was adopted for FACT meaning that a single data file can now contain multiple FACT recordings. For this reason `FACT_rec` creates new histograms for each FACT trigger.

`FACT_rec_min` was originally created as a minimum working example (hence the name suffix “min”) of `FACT_rec`. The main difference is that `FACT_rec` adds all input data together instead of creating individual histograms. For most antiproton based studies `FACT_rec` can serve as a starting point for developing new analyses.

For analysing cosmic radiation data, the `FACT_cosmics_rec` analysis was created. It carries out the track reconstruction procedure, produces histograms of the reconstructed param-

eters and outputs a summary of the performance of the fitting algorithm.

The analyses of the “Efficiency” category generate a vector of `AEgFACTEvent` instances and pass it on to the `AEgFACTefficiency` class which performs the efficiency analysis. The analysis itself then manages the output of the `AEgFACTefficiency` class once the calculations are done.

An exception in the “Efficiency” category is `FACT_cosmics_Eff_bin` because of the way that input data is handled. For normal operation `gAn` requires input data the form of the `AEgIS` standard `.root` files. However, as the name suffix “bin” of `FACT_cosmics_Eff_bin` suggests, this analysis runs on binary data. This was necessary because a change in `FACT` hardware meant that the possibility of saving cosmic radiation data in the standard `AEgIS` root-file format was no longer given. Since `gAn` requires root-files as input and the class infrastructure was needed for the cosmic radiation analysis a workaround was created. Usually a `gAn` analysis is executed as follows: `gAn *name of the analysis* *input data*`. The trick is to provide `gAn` with an arbitrary run so that the program will start. In the analysis the provided data is then ignored and instead a custom read method is used. The method reads binary files and creates an `AEgFACT` instance. This hack can be used whenever non `AEgIS` standard data need to be analysed and the `gAn` infrastructure is needed.

All analyses are comprised of a `.cpp` and a `.h` file located at `gAn/analysis`.

A more detailed view of the classes and scripts from table A.1 in C++ style comments is provided in the following. The descriptions feature the most important attributes and methods but are by no means exhaustive. For complete information the source code should be read.

#### AEgFACT

```

/* The AEgFACT class implements low-level functionalities. Most of the
   functions are called automatically. The only functions that have to be
   called explicitly in every FACT analysis are GetFACTs and BuildEvents. */

vector<AEgFACT *> GetFACTs(AEgRun *IO, uint64_t MinT, uint64_t MaxT)
/* Provides the user with a vector of all the AEgFACT entries in the current
   data file. Each AEgFACT instance holds the data from one FACT trigger.
   Implemented in AEgFACT but normally gets called from the AEgRun object
   of the analysis. Contains the check for collisions with AD activity. Was
   placed at this point because this ensured that the check gets called
   every analysis. May be moved to a more fitting location. */
vector<AEgFACTEvent> BuildEvents(Int_t cycles)
/* Builds the FACTEvents. The cycles variable controls how many adjacent
   clock-cycles are considered for events. 0 means that only one single 5
   ns time frame is used. 1 means two time frames, 2 three frames etc... As
   the rising edge of the FACT trigger currently get smeared out due to a
   too long cable, the recommended setting is cycles=2. */
class FiberMapper
/* Implements the fiber mapper class that performs the conversion from
   FPAG;MPPC to fiber number with position in r and z. The mapping issue
   discussed in appendix B was fixed here. */
class FiberPointer
/* Baseclass for AEgFACTHit. Implements functionalities such as comparison
   for sorting and getter functions for r and z position of a fiber, its
   fiber ID and FPGA MPPC combination */
map<int, uint64_t> GetMaxTimeFpga()
/* Returns a map of FPGA number and the time of the last recorded hit for
   that FGPA. Format: map<FPGA number, stop time in ns> */

```

```
vector<ULong64_t> GetTriggersNs(AEgRun *IO)
/* Returns the time(s) in ns when the FACT acquisition started during the
run. Useful for comparisons with the Scintillators since they start
acquiring at the beginning of the run. */
```

**AEgFACTEvent**

```
/* Holds a vector of AEgFACTHit instances grouped by rising edge time in a
window set by the BuildEvents function of AEgFACT. Each AEgFACTEvent is
given a time in ns according to the average rising edge time of the hits
(GetTimeNs()). Used as an intermediate step to form an
AEgVertexReconstructor instance. As this class is currently only used as
an intermediate step from an AEgFACT instance to AEgVertexReconstructor,
it might be useful for future iterations of gAn to scrap this class
altogether. */
```

**AEgFACTHit : public AEgFACT::FiberPointer**

```
/* Implements the AEgFACTHit class inheriting from AEgFACT::FiberPointer. Each
hit has properties as inherited from FiberPointer and a start time and
time over threshold in ns. */
```

**AEgFACTCluster**

```
/* Implements the AEgFACTCluster class, which acts as a grouping of hits.
Holds a vector of its constituent hits. Each cluster is assigned an r and
z value according to the average values of its hits. */
Int_t GetNLayers()
/* returns how many different sub-layers are contained within the cluster */
Bool_t IsUp()
/* returns whether or not the cluster is on the upper super-layer */
```

**AEgFACTTrack**

```
/* Implements the AEgFACTTrack class as a straight line through two clusters on
each super-layer. The line equation of the track is defined as:  $z(r) = a + b * r$ 
in order to avoid division by zero when calculating the parameter b.
The parameter a corresponds to the  $z_s$  value of the track and b to
 $\tan(\theta) = z/r$ . The corresponding getter methods are GetZIntercept()
GetTanTheta() respectively. Each track holds its constituent upper and
lower clusters. */
void LinearRegression()
/* Calculates the parameters a and b for a given combination of an upper and
a lower super-layer cluster. */
void RecomputeGuts()
/* Calculates LinearRegression() and sets the vector<int> missing_fibers.
This vector contains the fiber numbers which should have fired but did
not according to the reconstructed track. Currently a maximum of one
fiber per sub-layer is identified. Possible improvements for the MEM
could include reworking this algorithm to use a weighted likelihood
area. */
```

**AEgFACTVertex**

```
/* Implements the AEgFACTVertex class as the intersection of two (or more)
tracks. Due to the geometry of FACT, only the z value of the vertex is
reliable. As all reconstructed objects before (clusters and tracks), the
AEgFACTVertex also holds a vector of its constituent tracks. */
```



**AEgFACTCosmic**

```

/* Implements the AEgFACTCosmic class that holds the information about the
reconstructed parameters by the cosmic fitting procedure.
* The internal names for the variables correspond to the definitions from
this thesis as follows: m_ro = r_min, m_zo = z_min, m_tg = 1/tan(theta).
The hyperbola is therefore defined as: z(r) = m_zo +-
sqrt((pow(r,2)-pow(m_ro,2))/pow(m_tg,2)). Apart from the corresponding
getter methods for the parameters, AEgFACTCosmic features helper
functions for the MEM implemented in AEgFACTEfficiency. */
void Hyperbola_ZfromR(double R, double& Z1, double& Z2)
/* Returns the two z values of the hyperbola for a given r value */
int FindFiberFromRZ(int layer, double Z)
/* Finds the FACT fibers that the reconstructed hyperbolic track intersected
for a given sub-layer (0 is the outermost, 3 the innermost sub-layer). */
vector<int> GetPotentialFibers()
/* Returns a vector of fiber numbers of all fibers that the reconstructed
track intersected. For an improvement of MEM based measurements using
cosmic radiation this function and the FindFiberFromRZ might need to be
modified. */

```

**AEgVertexReconstructor**

```

/* Implements the FACT vertex reconstruction process based on FACTEvents.
Features getter functions that return vectors of hits, clusters, tracks
and vertices (GetHits(), GetCluster(), ...). */
void CreateClusters()
/* Groups the provided vector of AEgFACTHits into clusters */
void ComputeTracks()
/* Forms all possible tracks by using every combination of an upper and
lower super-layer cluster */
void Compute2Prongs()
/* Combines two tracks to form a vertex. In general two tracks and their
mirrored secants will intersect in two points but just the one with the
smaller r is saved. Additionally, a maximum radius is set (default is
0.5cm). Any vertices with r_rec>0.5cm will be ignored. */

```

**AEgCosmicReconstructor**

```

/* Implements the hyperbolic fitting procedure for cosmic track
reconstruction. This is where improvements for an MEM based measurement
should start. */
Bool_t IsCosmicComb()
/* Checks if the given vector of clusters is a valid cosmic combination. If
the clusters are in a trapezoidal shape with maximum one corner missing
the combination is considered valid and the track reconstruction is
performed. */
double hyp_r_z(double z, double ro, double zo, double tg)
/* Defines the equation of the hyperbola r(z) = sqrt(pow(ro,2.) +
pow(tg*(z-zo),2.)) for the fitting procedure. Returns the r value for a
given z, ro, zo and tg. */
Double_t SSR(Double_t ro, Double_t zo, Double_t tg)
/* Returns the sum of the squared residuals divided by the total number of
hits in the given configuration. This is used as the target function to
be minimized in the fitting procedure */
void minuitFunction(int& nDim, double* gout, double& result, double par[], int
flg)
/* Sets the return values of the SSR(...) so that ROOT can use them */

```

```

vector<double> minimization()
    /* Fitting function that carries out the hyperbolic fitting procedure using
       the ROOT MIGRAD and MINOS functions. */
vector<double> minimization2()
    /* Duplicate of the minimization function with a more elaborate initial
       parameter estimation. */
void Reconstruct()
    /* Executes both minimization() and minimization2() and chooses the better
       trajectory based on the smaller SSR value. */

```

**AEgFACTEfficiency**

```

/* Implements the MEM for antiproton annihilations and cosmic radiation. */
struct FiberEff
    /* This struct is used to store relevant information for the efficiency
       analysis on a per-fiber basis. Attributes include: fiber number, FPAG,
       MPPC, position in z and r, number of hits, number of misses, efficiency,
       values of threshold and bias. For threshold and bias the values are
       stored in vectors as multiple acquisitions might be used for an
       efficiency analysis and the bias value might change. This can be the
       case if the equalization routine is run during the course of the
       measurement. */

void AddEventP(AEgVertexReconstructor& event) // p for pbar or pion
    /* Implementation of the MEM algorithm for antiproton annihilations. Tracks
       are only used if their z_s value falls within llim <= z_s <= rlim. llim
       and rlim are set to -6cm and 0 cm for antiproton annihilations on the
       trap wall and to 12.6cm and 14.6cm for the HDMCP. This method only takes
       a single AEgVertexReconstructor instance as input. For carrying out the
       measurement, it is recommended to use the more convenient AddEventsP
       method. This function will probably need to be updated for improvements
       to the MEM. */

void AddEventsP(vector<AEgFACTEvent>& events, bool cuttrap, double timeveto)
    /* takes a vector of AEgFACTEvents as input, performs the reconstruction and
       passes each AEgVertexReconstructor instance into AddEventP. If the
       boolean value cuttrap is true llim and rlim are set to -6cm and 0cm
       respectively, if false the values for the HDMCP are used (12.6cm and
       14.6cm). The timeveto value is used for excluding AD related activity. */

void AddEventC(AEgCosmicReconstructor& Event) // c for cosmic
    /* Implementation of the MEM algorithm for cosmic radiation. Sorts the
       reconstructed cosmic tracks into fitting failed, geometry cut, total
       miss and good cosmic. If a trajectory is found to be a "good cosmic", it
       is used for the MEM analysis. In the same way as for AddEventP, this
       function will probably also need to be reworked for improving the MEM
       along with the AEgCosmicReconstructor class. */

void AddEventsC(vector<AEgFACTEvent>& events)
    /* Wraps a loop around AddEventC and automates the generation of the
       AEgCosmicReconstructor instances. */

void AddEventsN(vector<AEgFACTEvent>& events) // n for noise
    /* Special case of using the AEgFACTEfficiency class' infrastructure to
       check for all 794 fibers how much noise each channel produced. Used for
       the dead channel analysis to identify channels that do not produce any
       noise despite sufficient gain setting. */

void ComputeEff()
    /* Calculates the efficiency of each fiber as nhits/(nhits+nmisses) with an
       uncertainty of 1./sqrt(nhits+nmisses). Details on the considerations of
       how to calculate the uncertainty can be found directly in the
       AEgFACTEfficiency.h file in the comments of the FiberEff::ComputeEff()
       function. */

```

```

void AddTB(AEgFACT * fact)
  /* Reads the threshold and bias values for each channel so that, for
   example, efficiency value and MPPC settings can be correlated. */
void WriteResults(ostream &stream, bool addTB)
  /* Most important output function as it writes the results of the Efficiency
   analysis to a given ostream (default is again std::cout). The output is
   tab separated so that it can be read easily with any other program and
   features the following informations for each fiber: number, FPGA, MPPC,
   R(m), Z(m), nhits, nmisses and optionally bias and threshold. Using this
   list of tab separated values correlations between the efficiency value
   and position, threhold and bias and other properties can be
   investigated. */
void WriteFittingResults(ostream &stream)
  /* Outputs the results of the fitting algorithm in the four categories
   fitting failed, geometry cut, total miss and good cosmic. The default
   for stream = std::cout but it can be redirected to any file. */
void WriteOffset(ostream &stream, double cutoff, int offset)
  /* Writes a list of fibers (specified by FPGA MPPC) that get an offset for
   their bias values to a given ostream. Fibers with efficiency values
   below cutoff (e.g. .25 for targeting fibers below 25% efficiency) will
   be given a change in bias given by offset. This function was written in
   preparation for a calibration of FACT by increasing the bias values of
   the lowest efficiency fibers.
   * IMPORTANT CAVEAT: the MPPC number starts from 0 in gAn and from 1 for
   FACTDriver. Therefore, the MPPC+1 operation in the WriteOffset function
   is both intentional and necessary. Otherwise the generated offset
   configuration file will instruct FACTDriver to target the wrong MPPCs.
   */

```

**FACT\_rec**

```

/* Standard analysis for reconstruction of charged pion trajectories from pbar
annihilations. Creates histograms for: z_s distribution for reconstructed
tracks, z vertex distribution, number of tracks per time, z_s values per
time. If the given run features multiple FACT triggers or a number of runs
are provided as input, a new histogram is generated for each instance. */

```

**FACT\_rec\_min**

```

/* Initially created as a minimum working example of FACT_rec, this analysis
generated the same output as FACT_rec but adds all input data together in
the resulting histograms. */

```

**FACT\_cosmics\_rec**

```

/* Performs the track reconstruction for cosmic radiation data. Outputs
statistics on the performance of the fitting algorithm and produces a
number of histograms including the distributions of r_min, z_min, theta,
number of hits and clusters per event and the sum of squared residuals.
Can be used for testing and benchmarking the cosmic reconstruction
algorithm. */

```

**FACT\_Trap\_Eff**

```

/* Analysis for performing an MEM measurement using antiproton annihilations
on the walls of the production trap. The only parameter that is specific
to trap wall annihilations is the cuttrap=true value in the
AddEventsP(events=factevent_vector, cuttrap=true) function. */

```

**FACT\_HDMCP\_Eff**

```
/* Analysis for performing an MEM measurement using antiproton annihilations
   on the HDMCP. Uses cuttrap=false. Otherwise identical in functionality to
   FACT_Trap_Eff. */
```

**FACT\_cosmics\_Eff**

```
/* Analysis for performing an MEM measurement using cosmic radiation. Uses the
   AddEventsC function to carry out the measurement. */
```

**FACT\_cosmics\_Eff\_bin**

```
/* Identical in functionality to FACT_cosmics_Eff but features a custom read
   method that enables it to run with binary data. Needs to be provided a
   "dummy run" input so that the analysis starts. This run will not be used
   but instead binary data specified in the analysis are read. */
```

```
AEgFACT LoadBinaryFile(string FileName)
```

```
/* Reads the binary data file named FileName and returns and AEgFACT
   instance containing the data. */
```

**FACT\_tutorial**

```
/* Identical in functionality to FACT_rec_min but features detailed comments
   about the inner workings of a FACT analysis. Also contains suggestions for
   example data and some training exercises. */
```

Example solutions to the training exercises can be found on the AEGIS Twiki<sup>4</sup>.

**FACT\_cosmics\_read\_MC**

```
/* Reads the Monte Carlo generation files for the cosmic radiation simulation
   which contains the true r_min, z_0 and theta values. As this file is not
   in the standard AEGIS root file format but the gAn infrastructure was
   needed, the "hack" developed for FACT_cosmics_Eff_bin was used again. The
   analysis needs to be provided arbitrary input data which it will ignore
   but instead read a specified Monte Carlo generation file. */
```

**FACT\_positrons**

```
/* Analyzes the average time over threshold distribution for the FACT fibers
   for positrons hitting the conversion target. As the majority of the
   positrons annihilate upon impact, a lot of energy gets deposited in the
   FACT fibers which leads to ToT values around 1000 ns.
   * As this analysis was only used during the course of the investigation into
   the mapping issue and it is not particularly complex, it was not patched
   onto the gAn master branch. Instead it can only be found on the
   philip_thesis branch. */
```

**FACT\_source**

```
/* Analysis for the measurements with the radioactive source which were
   performed as the second part of the investigations into the mapping issue.
   As this is a "single-use" analysis it was also not patched onto the gAn
   master branch and can only be found on philip_thesis. */
```

<sup>4</sup>[https://twiki.cern.ch/twiki/bin/view/AEGIS/FACT\\_tutorial](https://twiki.cern.ch/twiki/bin/view/AEGIS/FACT_tutorial)

## Appendix B

# FACT Mapping

As mentioned briefly in the introduction to chapter 1, around 65 % of all positrons that are shot on the positronium conversion target, annihilate upon impact. The total amount of energy produced in this annihilation is enough to blind FACT for several hundred ns. In order to get a better grasp on how long exactly this blind time is for individual fibers, the time over threshold (ToT) distribution was studied. Since the time over threshold can be seen as a proxy for the amount of energy deposited in a fiber, the fibers close to the target (located at around  $z = 0$  cm,  $r = 1.7$  cm in FACT coordinates) are expected to exhibit higher values than the ones further away.

For the investigation into this issue, a total of 229 runs (run-numbers 102250-103478) featuring 300 positron accumulator pulses each, were analyzed. For each fiber the average time over threshold value and the standard deviation were calculated. In order to test the hypothesis, that fibers closer to the positronium converter exhibit longer time over threshold values, the fibers were divided into their respective super-layers and sorted along the  $z$ -direction. This was done by using the FACT mapping that links a combination of FPGA (numbered from 0–17) and MPPC (numbered from 0–47) to the corresponding fiber number (numbered from 0–793) with a position in  $z$  and  $r$ .

As a (previously mentioned by very important) side note, the numbering of the MPPCs starts at 1 and not at 0 for FACTDriver.

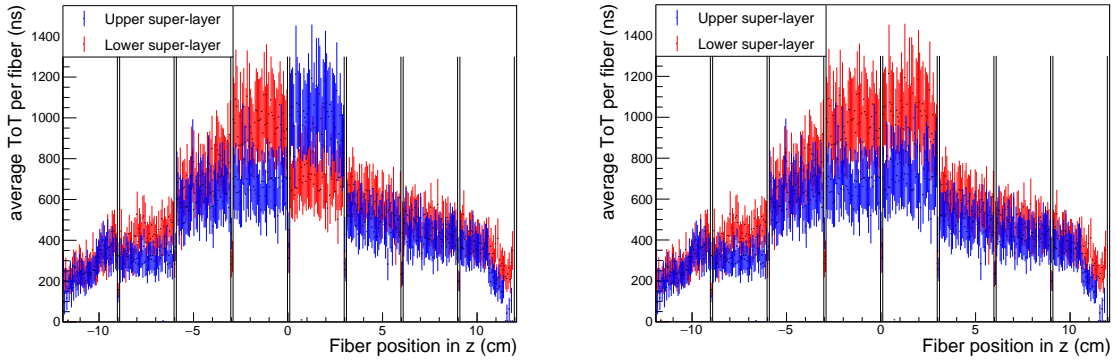
The results of the positron time over threshold analysis are shown in figure B.1a.

The results exhibit an overall expected behaviour: the values reach their maximum around  $z = 0$  cm and the lower super-layer in red exhibits higher values than the upper super-layer in blue. However, between 0 cm to 3 cm the two layers seem to be switched as the upper super-layer exhibits higher ToT values. The two FPGAs that correspond to this region are FPGA 9 on the lower and FPGA 10 on the upper super-layer. By swapping those two FPGAs with all their respective MPPCs in the mapping, the distributions now look exactly as expected, seen in figure B.1b.

Since this is not a conclusive proof that the updated mapping is now correct, a radioactive  $\beta^-$ -decaying 4 MBq  $^{137}\text{Cs}$  source was used to examine the mapping more closely. During the end of the year shutdown of CERN's accelerators, the AEGIS experiment was opened up as well for maintenance and upgrades. This allowed for access to production trap and to the steel cylinder that encloses FACT. Direct access to the FACT fibers itself was not possible as it would have required disassembling most of the 1 T region of the experiment. Therefore the source was placed inside the steel housing of FACT in order to irradiate the fibers through the housing.

The measurement method to check the FACT mapping works as follows:

- Acquire 10 min of data without the source for background assessment (to carry out the 10 min of continuous data taking the cosmic daemon described in subsection 2.4 was used)



(a) ToT distribution using the original FACT mapping (b) ToT distribution using the corrected FACT mapping

Figure B.1: Average time over threshold distribution (ToT) per fiber for 229 runs of positrons on the conversion target at 300 accumulator pulses displayed according to the  $z$ -position of the fiber. The error bars show the standard deviation of the ToT. The vertical lines mark the borders between fibers of the same FPGA. In (a) the original mapping, which was found to be incorrect, is used. In (b) the mapping is corrected by swapping FPGAs 9 and 10, located between 0 cm to 3 cm in  $z$ .

`gAn_FACT_positrons 102250-103478`

- Place the source inside the detector and measure its position in  $z$  with a metal ruler
- Acquire 10 min of data with the source
- Calculate the difference in the rate of hits per second for each fiber between the source measurement and the background
- Plot the difference as a function of the fiber position in  $z$

This process was repeated for five different positions of the source inside the detector. The maximum of the hit rate is expected to reflect the position of the source. The results of this measurement for each super-layer are shown in figure B.2.

Especially for the measurements for source positions of  $-5$  cm,  $0$  cm and  $5$  cm show good agreement between the expected one-to-one correlation between the source's location and the position of the maximum of the count rates. The two border measurements at around  $-11$  cm and  $11$  cm, however, show a slight shift in the count rate maximum towards the middle of FACT. As they still fit the overall trend, however, this shift is unlikely to be caused by another mistake in the mapping. To the best of our current knowledge (as of Jan 2019), the correct FACT mapping for FPGAs 0 to 15 looks as presented in table B.1.

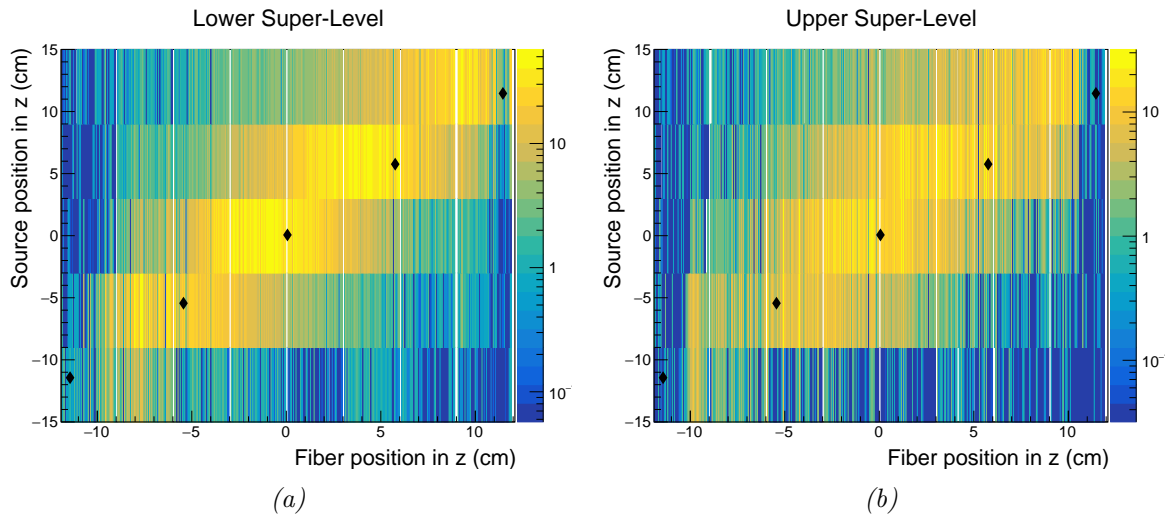


Figure B.2: Hit rates per second of each FACT fiber for five different positions of the radioactive source. Each row of the two heatmaps in (a) and (b) represents one position of the source. The black diamonds denote the source's exact position. As expected, the maximum in the hit rate the shifts according to the source's position. Additionally, the absolute count rates are consistently higher for the lower super-layer.

The mapping for FPGA 17 is presented in table B.2.

It has to be stated that both methods, the time over threshold analysis and the radioactive source measurement, can only be used to check the mapping indirectly. The only way to gain absolute certainty about the FACT mapping, is to disassemble the AEGIS-apparatus until the the FACT fibers can be accessed and check each fiber individually with a light source.

Table B.1: Mapping for FPGAs 0 – 15

FPGA	MPPC		Fib. Nr.			r (cm)		z(cm)		
0	0	–	23	225	–	248	9.80	-8.88	–	-6.12
	24	–	47	25	–	48	9.89	-8.82	–	-6.06
1	0	–	23	725	–	748	7.00	3.12	–	5.88
	24	–	47	525	–	548	7.09	3.18	–	5.94
2	0	–	23	325	–	348	9.80	3.12	–	5.88
	24	–	47	125	–	148	9.89	3.18	–	5.94
3	0	–	23	750	–	773	7.00	6.12	–	8.88
	24	–	47	550	–	573	7.09	6.18	–	8.94
4	0	–	23	350	–	373	9.80	6.12	–	8.88
	24	–	47	150	–	173	9.89	6.18	–	8.94
5	0	–	23	600	–	623	7.00	-11.88	–	-9.12
	24	–	47	400	–	423	7.09	-11.82	–	-9.06
6	0	–	23	200	–	223	9.80	-11.88	–	-9.12
	24	–	47	0	–	23	9.89	-11.82	–	-9.06
7	0	–	23	775	–	798	7.00	9.12	–	11.88
	24	–	46	575	–	597	7.09	9.18	–	11.82
8	0	–	23	375	–	398	9.80	9.12	–	11.88
	24	–	46	175	–	197	9.89	9.18	–	11.82
9	0	–	23	300	–	323	9.80	0.12	–	2.88
	24	–	47	100	–	123	9.89	0.18	–	2.94
10	0	–	23	700	–	723	7.00	0.12	–	2.88
	24	–	47	500	–	523	7.09	0.18	–	2.94
11	0	–	23	675	–	698	7.00	-2.88	–	-0.12
	24	–	47	475	–	498	7.09	-2.82	–	-0.06
12	0	–	23	275	–	298	9.80	-2.88	–	-0.12
	24	–	47	75	–	98	9.89	-2.82	–	-0.06
13	0	–	23	650	–	673	7.00	-5.88	–	-3.12
	24	–	47	450	–	473	7.09	-5.82	–	-3.06
14	0	–	23	250	–	273	9.80	-5.88	–	-3.12
	24	–	47	50	–	73	9.89	-5.82	–	-3.06
15	0	–	23	625	–	648	7.00	-8.88	–	-6.12
	24	–	47	425	–	448	7.09	-8.82	–	-6.06



Table B.2: Mapping for FPGA 17

MPPC	Fib. Nr.	r (cm)	z (cm)
0	124	9.89	3.06
1	224	9.80	-9.00
2	724	7.00	3.00
4	324	9.80	3.00
5	374	9.80	9.00
6	474	7.09	-2.94
7	524	7.09	3.06
8	624	7.00	-9.00
9	574	7.09	9.06
10	249	9.80	-6.00
13	349	9.80	6.00
16	74	9.89	-2.94
17	549	7.09	6.06
20	649	7.00	-6.00
22	149	9.89	6.06
23	174	9.89	9.06
24	274	9.80	-3.00
26	299	9.80	0.00
30	449	7.09	-5.94
34	99	9.89	0.06
36	674	7.00	-3.00
37	699	7.00	0.00
40	749	7.00	6.00
41	774	7.00	9.00
43	424	7.09	-8.94
45	24	9.89	-8.94
46	49	9.89	-5.94
47	499	7.09	0.06



Die approbierte gedruckte Originalversion dieser Diplomarbeit ist an der TU Wien Bibliothek verfügbar.  
The approved original version of this thesis is available in print at TU Wien Bibliothek.

## Appendix C

# Dead Channels

During the course of analyzing FACT data, a number of dead channels have been identified.

This identification was done using two different methods.

The first method involves the results from the antiproton annihilation efficiency studies from section 3.1. As discussed in section 2.2, the efficiency assessment algorithm is successful at singling out dead fibers and can therefore be used for this task.

As a side note: in the context of this analysis, a fiber is only considered dead if it does not feature a single hit. There is, however, a number of low-efficiency fibers with efficiencies below 0.1, including fibers with only a single hit compared to hundreds of misses. As stated above, those fibers are not considered dead in this analysis. For further investigations into those low efficiency fibers the complete results of the efficiency assessment can be found on the AEGIS-TWiki <https://twiki.cern.ch/twiki/bin/view/AEGIS/FACTEffRes>.

The second method for identifying dead channels works based on checking random noise rates for every channel. The data source for this analysis is 10 min of cosmic radiation data. All channels that did not produce any random noise in this time-frame are considered not working. In order to exclude any effects of a fiber not firing due to a too low bias setting, the equalization routine with a target rate of 50 Hz of random noise was run just before the acquisition.

An overview of all channels that were found to be dead is presented in table C.1. As mentioned before, the MPPC numbering for the bias and threshold table that FACTDriver uses starts at 1 and not at 0. The MPPC numbering in table C.1, however, starts at 0 in order to be in line with gAn.

Looking at the patterns in table C.1 two different kinds of dead fibers can be identified.

The first kind has the following form: † †/- †/-. At least one of the efficiency assessment methods found the fiber to be dead and the random noise analysis found the same result. Most likely this means that the MPPC is dead and should be replaced.

The second pattern looks like this: ✓ †/- †/-. Again, at least one of the efficiency assessment methods identified the fiber as dead, however, this time it was found producing random noise. The conclusion that one might draw is that the sensor itself is working, while for some reason the scintillation photons fail to reach it. A reason for this could be a faulty connection between the clear fiber that guides the photons and the MPPC. The clear fibers connect to the sensors on the MPPC board through a plastic socket. Located behind those MPPC boards are screws that hold together the AEGIS apparatus. As they need to be accessed during opening and closing of the experiment. It is not unthinkable that some connections were compromised during this procedure.

In conclusion, replacing the MPPC for the channels in the first category and checking the connections on the second category looks to be a way to quickly improve the overall efficiency of the FACT detector.

Table C.1: Overview of the 30 dead FACT channels as of Jan 2019.

The left three columns specify the fiber with FPGA, MPPC and fiber number. All three numbers are counted starting at 0. The right three columns specify the method of assessing the fiber status (fib. stat.). “N” stands for random noise, “T” specifies efficiency analysis based on antiproton trap wall annihilations and “H” specifies efficiency analysis based on antiproton HDMCP annihilations.

“†” marks a fiber identified as dead.

“✓” is only used for the “N” columns to mark a fiber that produced any amount of random noise greater than zero.

“–” is only used in the “T” and “H” columns to signal that there is no information about the fiber. The reason for this is that the fiber in question is part of the grey regions shown in figure 2.3

FPGA	MPPC	Fib. Nr.	Fib. Stat.		
			N	T	H
1	34	535	†	†	†
2	16	341	†	†	†
2	32	133	†	†	†
3	7	757	†	†	†
3	18	768	†	†	†
3	32	558	†	†	†
3	34	560	†	†	†
3	45	571	†	–	†
3	47	573	†	–	†
4	18	368	†	†	†
5	37	413	✓	†	–
6	46	22	†	†	–
7	2	777	†	–	†
7	32	583	†	–	†
8	20	395	✓	†	–
8	21	396	✓	†	†
8	22	397	✓	†	–
8	33	184	✓	†	†
8	43	194	✓	†	–
8	44	195	✓	†	–
9	17	317	†	†	†
10	5	705	†	†	†
14	8	258	†	†	†
15	21	646	✓	†	–
17	1	224	✓	†	–
17	7	524	†	†	†
17	10	249	✓	†	†
17	13	349	†	†	†
17	16	74	†	†	†
17	30	449	†	†	–

# List of Tables

1.1	Worst-case errors for track reconstruction . . . . .	24
2.1	Classification of all 16 configurations for charged pion tracks . . . . .	39
2.2	Probabilities for the all “trackable” cases . . . . .	40
2.3	Overview of hit and miss combinations . . . . .	41
2.4	Distribution of the number of clusters per simulated cosmic muon . . . . .	46
2.5	Classification of particle tracks for $\overline{E}_f = 0.5$ in untrackable and trackable for charged pions and cosmic muons . . . . .	47
2.6	Cosmic fitting algorithm performance for perfect and 50 % efficiency . . . . .	57
3.1	Average fiber efficiency values for antiproton annihilations on the trap wall and on the HDMCP . . . . .	69
3.2	Counts/ $\overline{p}$ for SC2122 for three different minimum deposited energies $E_{minS}$ inside the detector material. . . . .	71
3.3	Simulated amount of tracks in the signal regions for antiproton annihilations on the trap walls and on the HDMCP . . . . .	72
3.4	Overview of the number of FACT tracks, SC2122 counts and the ratios for measured antiproton annihilations on the trap wall . . . . .	76
3.5	Overview of the number of FACT tracks, SC2122 counts and the ratios for measured antiproton annihilations on the trap wall . . . . .	77
3.6	Performance of the fitting algorithm for 15,740 seconds of cosmic radiation data . . . . .	78
A.1	Overview of FACT related C++ classes and analysis scripts . . . . .	88
B.1	Mapping for FPGAs 0 – 15 . . . . .	98
B.2	Mapping for FPGA 17 . . . . .	99
C.1	Overview of the 30 dead FACT channels . . . . .	102



Die approbierte gedruckte Originalversion dieser Diplomarbeit ist an der TU Wien Bibliothek verfügbar.  
The approved original version of this thesis is available in print at TU Wien Bibliothek.

# List of Figures

1	Antihydrogen gravity measurement principle . . . . .	3
2	Schematic of the antihydrogen production process. . . . .	4
3	Schematic of the AEGIS apparatus . . . . .	5
4	Antihydrogen production region renders . . . . .	6
1.1	Artistic render of an $\bar{H}$ -annihilation . . . . .	10
1.2	3D views of the two FACT cylinders . . . . .	11
1.3	Illustration of the FACT coordinate system . . . . .	11
1.4	Illustration of the “circular-honeycomb” pattern of the FACT layers . . . . .	12
1.5	Gain vs. temperature and Gain vs. bias curves for the FACT MPPCs . . . . .	14
1.6	MPPC board temperature during the summer months of 2018 . . . . .	15
1.7	Illustration of the FPGA, MPPC numbering scheme . . . . .	16
1.8	Schematic of FACT detector’s control and readout system . . . . .	19
1.9	Illustration of a hyperbolic particle track . . . . .	21
1.10	Illustration of the clustering process . . . . .	22
1.11	Illustration of pion track reconstruction . . . . .	24
1.12	Illustration of an antiproton annihilation in 3D space . . . . .	26
1.13	Illustration of an antiproton annihilation in 2D FACT coordinates . . . . .	27
1.14	Illustration of vertex reconstruction . . . . .	27
1.15	Illustration of track multiplicity . . . . .	28
1.16	Illustration of a cosmic muon crossing FACT in 3D and 2D . . . . .	30
1.17	Overview of the VertexReconstructor class . . . . .	32
2.1	Illustration of the fiber numbering system for deriving the MEM . . . . .	38
2.2	Illustration of the MEM algorithm with three different example configurations . . . . .	42
2.3	Regions in $z$ for antiproton annihilations on the trap walls and on the HDMCP . . . . .	44
2.4	Illustration of the half sphere used for the cosmic radiation Monte Carlo simulation . . . . .	46
2.5	“Trackable” and “usable” fractions of cosmic muons and charged pions as a function of the average fiber efficiency . . . . .	48
2.6	Required amount of $\bar{p}$ annihilations and cosmic radiation acquisition time . . . . .	49
2.7	Histograms of reconstructed $z_s$ -values for MC antiproton annihilations on the trap wall and on the HDMCP . . . . .	50
2.8	Overview of the MEM’s performance for Monte Carlo simulated antiproton trap wall annihilations . . . . .	51
2.9	Error correlations for single fiber efficiencies obtained using the MEM for MC simulated antiproton trap wall annihilations . . . . .	52
2.10	Overview of the MEM’s performance for Monte Carlo simulated antiproton HDMCP annihilations . . . . .	53
2.11	Error correlations for single fiber efficiencies obtained using the MEM for MC simulated antiproton HDMCP annihilations . . . . .	54

2.12	Examples for the three different categories of successfully reconstructed cosmic muon trajectories . . . . .	56
2.13	Distributions of the reconstructed $z_0$ , $r_{min}$ and $\theta$ parameters for MC simulated cosmic radiation . . . . .	57
2.14	Overview of the MEM's performance for Monte Carlo simulated cosmic radiation . . . . .	58
2.15	Error correlations for single fiber efficiencies obtained using the MEM for MC simulated cosmic radiation . . . . .	59
3.1	FACT_rec analysis of radial antiproton plasma expansion procedure . . . . .	64
3.2	MEM results using trap wall antiproton annihilations . . . . .	65
3.3	Correlation plot between fiber efficiency and bias setting for trap wall antiproton annihilations . . . . .	66
3.4	FACT_rec analysis of antiproton annihilations on the HDMCP . . . . .	67
3.5	MEM results using antiproton annihilations on the HDMCP gAn FACT_HDMCP_Eff 148020-148023 . . . . .	68
3.6	Correlation plot between fiber efficiency and bias setting for HDMCP antiproton annihilations . . . . .	69
3.7	Visual representation of the two average fiber efficiency values from the trap wall and HDMCP annihilation efficiency analysis. . . . .	70
3.8	Time-resolved comparison between FACT and SC2122 using trap wall antiproton annihilations . . . . .	74
3.9	Detail view of the first 250 ms of time-resolved comparison between FACT and SC2122 using trap wall antiproton annihilations . . . . .	75
3.10	Time-resolved comparison between FACT and SC2122 using antiproton annihilations on the HDMCP . . . . .	76
3.11	Distributions of the $z_0$ , $r_{min}$ and $\theta$ parameters measured cosmic muon trajectories . . . . .	78
3.12	MEM results for recorded cosmic radiation . . . . .	79
B.1	Average time over threshold distributions for positron annihilations for the faulty and the corrected FACT mapping . . . . .	96
B.2	Heatmaps of the scan across FACT to cross-check the mapping with a radioactive source . . . . .	97



# Bibliography

- [1] J. D. Hunter. “Matplotlib: A 2D graphics environment”. In: *Computing In Science & Engineering* 9.3 (2007), pp. 90–95. DOI: 10.1109/MCSE.2007.55.
- [2] Owen Chamberlain et al. “Observation of Antiprotons”. In: *Phys. Rev.* 100 (3 Nov. 1955), pp. 947–950. DOI: 10.1103/PhysRev.100.947. URL: <https://link.aps.org/doi/10.1103/PhysRev.100.947>.
- [3] Bruce Cork et al. “Antineutrons Produced from Antiprotons in Charge-Exchange Collisions”. In: *Phys. Rev.* 104 (4 Nov. 1956), pp. 1193–1197. DOI: 10.1103/PhysRev.104.1193. URL: <https://link.aps.org/doi/10.1103/PhysRev.104.1193>.
- [4] T. Massam et al. “Experimental observation of antideuteron production”. In: *Nuovo Cimento Serie* 39 (Sept. 1965), pp. 10–14. DOI: 10.1007/BF02814251.
- [5] D. E. Dorfan et al. “Observation of Antideuterons”. In: *Physical Review Letters* 14 (July 1965), pp. 1003–1006. DOI: 10.1103/PhysRevLett.14.1003.
- [6] G. Bandr et al. “Production of antihydrogen”. In: *Physics Letters B* 368 (Feb. 1996), pp. 251–258. DOI: 10.1016/0370-2693(96)00005-6.
- [7] G. Blanford et al. “Observation of Atomic Antihydrogen”. In: *Phys. Rev. Lett.* 80 (14 Apr. 1998), pp. 3037–3040. DOI: 10.1103/PhysRevLett.80.3037. URL: <https://link.aps.org/doi/10.1103/PhysRevLett.80.3037>.
- [8] Robert D Reasenberget al. “Design and characteristics of a WEP test in a sounding-rocket payload”. In: *Classical and Quantum Gravity* 29.18 (2012), p. 184013. URL: <http://stacks.iop.org/0264-9381/29/i=18/a=184013>.
- [9] The ALPHA Collaboration et al. “Description and first application of a new technique to measure the gravitational mass of antihydrogen”. In: *Nature Communications* 4 (Apr. 2013). Article, p. 1785. URL: <http://dx.doi.org/10.1038/ncomms2787>.
- [10] G Yu Drobychev et al. *Proposal for the AEGIS experiment at the CERN antiproton decelerator (Antimatter Experiment: Gravity, Interferometry, Spectroscopy)*. Tech. rep. SPSC-P-334. CERN-SPSC-2007-017. Geneva: CERN, July 2007. URL: <https://cds.cern.ch/record/1037532>.
- [11] S. Aghion et al. “A moiré deflectometer for antimatter”. In: *Nature Communications* 5 (July 2014). Article, p. 4538. URL: <http://dx.doi.org/10.1038/ncomms5538>.
- [12] Guatieri Francesco. “Production and excitation of cold Ps for  $\bar{H}$  formation by charge exchange: towards a gravitational measurement on antimatter”. PhD thesis. Università degli Studi di Trento, 2018.
- [13] M. Amoretti et al. “Production and detection of cold antihydrogen atoms”. In: *Nature* 419 (Sept. 2002), p. 456. URL: <http://dx.doi.org/10.1038/nature01096>.
- [14] A. Kellerbauer et al. “Ultracold antiprotons by indirect laser cooling”. In: *Hyperfine Interactions* 194.1 (Aug. 2009), p. 77. ISSN: 1572-9540. DOI: 10.1007/s10751-009-0033-6. URL: <https://doi.org/10.1007/s10751-009-0033-6>.

- [15] G. Gabrielse et al. “First Measurement of the Velocity of Slow Antihydrogen Atoms”. In: *Phys. Rev. Lett.* 93 (7 Aug. 2004), p. 073401. DOI: 10.1103/PhysRevLett.93.073401. URL: <https://link.aps.org/doi/10.1103/PhysRevLett.93.073401>.
- [16] Zurlo N. “CAD-based Monte Carlo simulations in Mathematica for positronium excitation and antihydrogen production in the AEGIS experiment @ CERN”. European Wolfram Technology Conference 2018. 2018.
- [17] M. Doser et al. “AEGIS at ELENA: outlook for physics with a pulsed cold antihydrogen beam”. In: *Philosophical Transactions of the Royal Society of London A: Mathematical, Physical and Engineering Sciences* 376.2116 (2018). ISSN: 1364-503X. DOI: 10.1098/rsta.2017.0274. eprint: <http://rsta.royalsocietypublishing.org/content/376/2116/20170274.full.pdf>. URL: <http://rsta.royalsocietypublishing.org/content/376/2116/20170274>.
- [18] Nebbia Giancarlo. *Monitoring the Ps formation both in the AEGIS setup and in the Ps chamber*. Tech. rep. CERN/AEGIS collaboration, 2017. URL: <https://twiki.cern.ch/twiki/bin/view/AEGIS/FACTPositroniumDiagnostics>.
- [19] J. Storey et al. “Particle tracking at cryogenic temperatures: the Fast Annihilation Cryogenic Tracking (FACT) detector for the AEGIS antimatter gravity experiment”. In: *Journal of Instrumentation* 10.02 (2015), p. C02023. URL: <http://stacks.iop.org/1748-0221/10/i=02/a=C02023>.
- [20] KURARAY CO. LTD. *Plastic Scintillating Fibers (Materials and Structures)*. URL: <http://kuraraypsf.jp/psf/index.html> (visited on 07/10/2018).
- [21] Haider David. “Characterization of the AEGIS scintillating fiber detector FACT for antihydrogen detection”. MA thesis. TU Wien, 2017.
- [22] Hamamatsu. *Si APD, MPPC*. 2014. URL: [https://www.hamamatsu.com/resources/pdf/ssd/e03\\_handbook\\_si\\_apd\\_mppc.pdf](https://www.hamamatsu.com/resources/pdf/ssd/e03_handbook_si_apd_mppc.pdf) (visited on 09/23/2018).
- [23] Bonomi Germano. *Cosmics reconstruction with the FACT: a MC study*. Tech. rep. Università degli Studi di Brescia, 2018.
- [24] Pagano Davide. *On the reconstruction of annihilation vertices with the FACT detector*. Tech. rep. Università degli Studi di Brescia & INFN, 2017. URL: <https://indico.cern.ch/event/630100/contributions/2546282/>.
- [25] Rudolf Frühwirth. *Wahrscheinlichkeitsrechnung und Statistik für Studierende der Physik*. Rudolf Frühwirth & bookboon.com, 2015. ISBN: 978-87-403-0847-1. URL: [http://www.hephy.at/project/ilc/reports/ASEpub/14\\_eBook\\_by\\_RF.pdf](http://www.hephy.at/project/ilc/reports/ASEpub/14_eBook_by_RF.pdf) (visited on 11/18/2018).
- [26] M. Hori et al. “Analog Cherenkov detectors used in laser spectroscopy experiments on antiprotonic helium”. In: *Nuclear Instruments and Methods in Physics Research Section A: Accelerators, Spectrometers, Detectors and Associated Equipment* 496.1 (2003), pp. 102–122. ISSN: 0168-9002. DOI: [https://doi.org/10.1016/S0168-9002\(02\)01618-2](https://doi.org/10.1016/S0168-9002(02)01618-2). URL: <http://www.sciencedirect.com/science/article/pii/S0168900202016182>.
- [27] M. C. Fujiwara et al. “Three-Dimensional Annihilation Imaging of Trapped Antiprotons”. In: *Phys. Rev. Lett.* 92 (6 Feb. 2004), p. 065005. DOI: 10.1103/PhysRevLett.92.065005. URL: <https://link.aps.org/doi/10.1103/PhysRevLett.92.065005>.
- [28] Bonomi G. *Simulations for the AEGIS experiment*. 2017. URL: <https://twiki.cern.ch/twiki/bin/view/AEGIS/WebHome#Simulations> (visited on 02/21/2019).